UNIVERSITY OF READING

Department of Meteorology

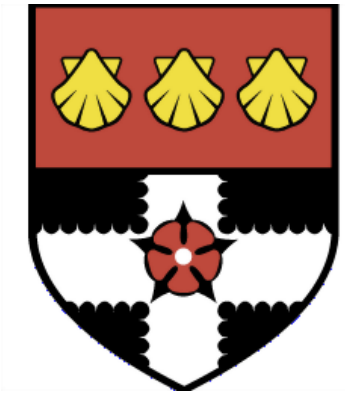

Mountain wave breaking in atmospheric flows with directional wind shear

Maria Vittoria Guarino

A thesis submitted for the
degree of Doctor of Philosophy

November 2017

Declaration of Authorship

I confirm that this is my own work and the use of all material from other sources has been properly and fully acknowledged.

Maria Vittoria Guarino

Signed: _____

Date: _____

"Everything is simpler than you think,
and at the same time more complex than you imagine"

Goethe

UNIVERSITY OF READING

Abstract

Department of Meteorology

Doctor of Philosophy

by Maria Vittoria Guarino

In this thesis, mountain wave breaking triggered by directional wind shear is investigated using numerical simulations of idealized and semi-idealized orographic flows.

Idealized simulations are used to produce a regime diagram to diagnose conditions for wave breaking in Richardson number-dimensionless mountain height parameter space. It is found that, in the presence of directional shear, wave breaking can occur over lower mountains than in a constant-wind case. Furthermore, the extent of regions within the simulation domain where Clear-Air Turbulence (CAT) is expected increases with terrain elevation and background wind shear intensity.

Analysis of the model output, supported by theoretical arguments, suggest the existence of a link between wave breaking and the relative orientations of the incoming wind vector and the horizontal velocity perturbation vector. This condition provides a possible diagnostic for CAT forecast in directional shear flows.

The stability of the flow to wave breaking in the transition from hydrostatic to non-hydrostatic mountain waves is also investigated. Wave breaking seems to be inhibited by non-hydrostatic effects for weak wind shear, but enhanced for stronger wind shear.

In the second part of the thesis, a turbulence encounter observed over the Rocky Mountains (in Colorado, USA) is studied. The role of directional shear in causing wave breaking is isolated from other possible wave breaking mechanisms through various sensitivity tests. The existence of an asymptotic wake, as predicted by Shutts for directional shear flows, is hypothesized to be responsible for a significant downwind transport of unstable air detected in cross-sections of the flow.

Finally, critical levels induced by directional shear are studied by spectral analysis of the horizontal velocity wave perturbations. This is done for a fully idealized flow and for the more realistic flow corresponding to the investigated turbulence encounter. In these 2D power spectra, a rotation of the most energetic wave modes with the background wind and their selective absorption can be found. Such behaviour is consistent with the mechanism leading to wave breaking in directional shear flows.

Acknowledgements

First and foremost I would like to express my gratitude to my supervisor, Dr. Miguel Teixeira, who has provided me with continuous support and guidance over the course of my PhD. I appreciate the time he spent in our weekly meetings over the past three and a half years answering my questions, giving excellent advice on how overcoming difficulties and pursuing research goals. His attention to details and supervision have been precious allies down the road to a PhD.

I would also like to acknowledge Prof. Maarten Ambaum, for offering co-supervision and support, Prof. Ted Shepherd and Prof. Paul Williams, for serving as my monitoring committee members and for their constructive comments and useful suggestions.

Next, I would like to express my thanks to Dr. Robert Sharman and Dr. Teddie Keller for hosting me at NCAR and making my stay in Boulder so enjoyable. It was an honour and a pleasure to collaborate with them.

I thank all those people I met since I moved to the U.K. who contributed, each in a personal way, to shape the past years and whose presence became part of my quotidian life. In particular, I would like to mention the fellow PhD students of Lyle 3, with whom I shared the journey of a doctoral degree, and those people who for a long time have been my housemates.

A special thanks goes to my boyfriend, whose sense of humor, company and unconditional help in all aspects of life helped me immensely throughout my PhD.

Finally, as it is not possible to mention all of them, my gratitude goes to all those who, at unspecified times, places, and situations in my life, contributed to my educational and personal growth relaying me the curiosity for knowledge and inspiring me to grow into my own ambitions.

Maria Vittoria Guarino

This work has been accomplished with the financial support of the European Commission under Marie Curie Career Integration Grant GLIMFLO, contract PCIG13-GA-2013-618016.

Contents

Declaration of Authorship **iii**

Abstract **vii**

Acknowledgements **ix**

Most Frequent Symbols **xv**

1 Introduction **1**

1.1 Atmospheric waves and turbulence 1

1.2 Motivation 4

1.3 Outline of the thesis 7

2 Methodology: theoretical and numerical aspects **9**

2.1 The physics of mountain waves 9

2.1.1 The Taylor-Goldstein equation 9

2.1.2 A zeroth- and first- order WKB solution of the TG equation . 12

2.1.3 The scaling of key flow parameters 13

2.2 The Weather, Research and Forecasting (WRF) Model 15

2.2.1 Idealized model set-up 15

2.2.2 The WRF 1.5 order turbulence closure 17

3 Turbulence generation by mountain wave breaking in flows with directional wind shear **19**

3.1 Introduction 20

3.2 Methodology 24

3.2.1 Setup of numerical simulations 24

3.2.2 Calculation of $\mathrm{Ri}_{\mathrm{min}}$ near the mountain 26

3.3 Results and discussion 28
3.3.1 Simulations without wind shear 29
3.3.2 Wind shear simulations 31
3.3.2.1 Non-wave breaking regime 34
3.3.2.2 Wave breaking regime 35
3.3.3 A possible wave breaking diagnostic 41
3.4 Summary and conclusions 45
3.5 Appendix 3.A: Turbulent flow behaviour 48
3.5.1 Turbulence generated by shear and buoyancy production . . . 48
3.5.2 A TKE-based regime diagram 51
3.6 Appendix 3.B: Testing a possible wave breaking diagnostic 53

4 Non-hydrostatic effects on mountain wave breaking in directional shear flows 59
4.1 Introduction 59
4.2 Methodology 61
4.2.1 Numerical simulations 61
4.2.2 Wave breaking diagnosis 62
4.2.3 Non-hydrostatic mountain waves 64
4.3 Results and discussion 65
4.3.1 Non-hydrostatic effects on wave breaking 65
4.3.2 A regime diagram for non-hydrostatic mountain waves 67
4.4 Summary and conclusions 73

5 Mountain wave turbulence in the presence of directional wind shear over the Rocky Mountains 75
5.1 Introduction 76
5.2 Wave breaking mechanism in directional shear flows 78
5.3 Methodology 80
5.3.1 PIREPs and case study selection 80
5.3.2 Numerical simulations 83
5.4 Results and discussion 85
5.4.1 Semi-idealized simulations: real atmospheric sounding and orography 85
5.4.2 Sensitivity tests 87
5.4.2.1 Test 1: the bottom boundary condition / surface forcing 88

5.4.2.2 Test 2: the tropopause and the variation of N with height 90
5.4.2.3 Test 3: the speed shear 91
5.4.2.4 Test 4: the mountain amplitude 95
5.4.3 The directional shear contribution 96
5.4.3.1 Spectral analysis of the wave field 99
5.5 Summary and conclusions 104
5.6 Appendix 5.A: Wave energy distribution at critical levels 108

6 Conclusions **113**
6.1 Summary 113
6.2 Main results and conclusions 114
6.3 Directions for future work 117

Bibliography **121**

Most Frequent Symbols

Symbol	Name	Unit
a	Mountain half-width	m
e	Turbulent kinetic energy	$\mathrm{m^2\ s^{-2}}$
f	Coriolis parameter	$\mathrm{s^{-1}}$
g	Acceleration of gravity	$\mathrm{m\ s^{-2}}$
H	Mountain height	m
N_0	Brunt-Väisälä frequency of the background flow	$\mathrm{s^{-1}}$
p_0	Pressure of the background flow	hPa
p_1	Pressure perturbation	hPa
Ri_{in}	Richardson number of the background flow	
Ri_{min}	Minimum Richardson number of the total flow	
Ri_{out}	Richardson number of the total flow	
$(u_0, v_0, 0)$	Background wind velocity vector	$\mathrm{m\ s^{-1}}$
(u_1, v_1, w_1)	Wind velocity perturbation vector, also denoted by primes	$\mathrm{m\ s^{-1}}$
β	Rate of wind turning with height	$\mathrm{m^{-1}}$
ε	Eddy dissipation rate, unless otherwise specified	$\mathrm{m^2\ s^{-3}}$
θ_0	Potential temperature of the background flow	K
θ_1	Potential temperature perturbation	K
$\boldsymbol{\kappa} \equiv (k, l, m)$	3D wave-number vector	$\mathrm{m^{-1}}$
$\boldsymbol{\kappa}_H \equiv (k, l, 0)$	Horizontal wave-number vector	$\mathrm{m^{-1}}$
λ_x	Horizontal wavelength	m
λ_z	Vertical wavelength	m
ρ_0	Background atmospheric density	$\mathrm{Kg\ m^{-3}}$
$(\ \widehat{}\ )$	Symbol used to denote the Fourier transforms	

Chapter 1

Introduction

1.1 Atmospheric waves and turbulence

Atmospheric gravity waves originate from an imbalance in the buoyancy of the flow. While propagating in the fluid medium, gravity waves transport energy and drive changes in winds, temperature and chemical composition of the atmosphere (through redistribution of atmospheric constituents in wave breaking regions and forcing of mean circulations).

As gravity or, more precisely, buoyancy is the restoring force responsible for sustaining the wave motion, gravity waves only exist in atmospheres with a stable density/temperature stratification. In fact, gravity waves are a constant (most of the time invisible) presence in our skies, but their existence is only occasionally revealed through cloud patterns. Indeed, except for the lowest 1-3 km (corresponding to the Planetary Boundary Layer, PBL) and geographical regions affected by deep convection like the tropics, the atmosphere is generally stably stratified and a variety of wave sources exist. Some of them are: orographic lift, convective clouds and jet/front systems.

Gravity waves launched by orographic barriers generally belong to the category of internal waves, as they propagate in the interior of the fluid and not at the discontinuity surface between two media with different density (e.g., the air-sea interface). Internal gravity waves are transverse waves for which the parcel oscillations are perpendicular to the direction of propagation. When the response of the flow to the orographic forcing occurs on short time scales, waves are not affected by the Earth's rotation and the Coriolis force can be neglected. In this case, orographic waves are said to be "pure internal gravity waves" (Holton and Hakim, 2012).

(a)

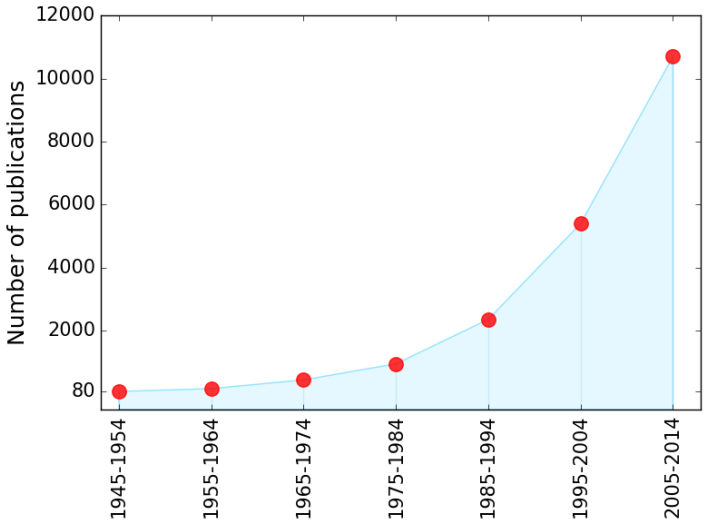

(b)

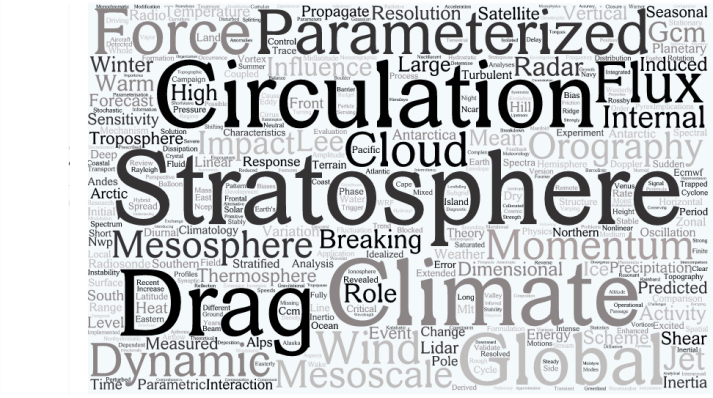

FIGURE 1.1: (a) number of publications between 1945 and 2014 by decade including the words "orographic gravity waves" anywhere in the article, according to Google Scholar. (b) word cloud generated using the titles of the 1000 most cited papers published between 1945 and 2014 including the words "orographic gravity waves". Note that no significance is attached to the greyscale used.

Mountain waves are able to propagate horizontally and vertically, playing a part in the atmospheric dynamics at different scales. They received great attention in the past 20-30 years as a consequence of a growing awareness of their ubiquity, their role in the atmospheric dynamics and technological advances as a result of which orographic waves began to be more often observed in measurement campaigns (Nappo, 2012).

Figure 1.1 (a) shows the number of publications per decade from 1945 to 2014 containing (all) the words "orographic gravity waves", in the title or in the main body of the article. The graph was generated using the Google Scholar database and, although data may suffer from some inaccuracy such as multiple versions for a same publication or missing publications, it gives an idea of the exponential growth of papers discussing mountain waves since 1945. Around that time, Queney (1947) published one of the earliest studies dealing explicitly with orographic waves. Between 1945

and 1954 about 70 papers with the words "orographic gravity waves" were published, between 2005 and 2014 almost 11000.

Figure 1.1 (b) provides an overview of the most popular research areas where mountain waves have been/are studied. The word "cloud" was produced using the titles of the 1000 most cited papers between 1945 and 2014 containing the words "orographic gravity waves"[1]. The size of the words represents the frequency and, thus, the popularity of the topic (i.e., the bigger the word, the higher the number of papers).

Numerous studies focus on orographic drag and its parameterization (e.g., McFarlane, 1987, Shutts, 1995, Miranda and James, 1992, Teixeira *et al.*, 2004), the deceleration of the global atmospheric circulation due to divergence of the momentum flux associated with wave breaking events (Lilly and Kennedy, 1973) and its influence on climate (e.g., Boer and Lazare, 1988, Sigmond *et al.*, 2008). At the mesoscale, mountain waves are often investigated in connection with orographic precipitations (see e.g., Barstad *et al.*, 2007) and, within the boundary layer, in connection with variations of the PBL structure, downslope windstorms and boundary layer separation (e.g. Grisogono and Enger, 2004, Durran, 1990, Grubišić *et al.*, 2015, Sun *et al.*, 2015). At higher altitudes, breaking mountain waves are studied because of their ability to generate aviation-scale turbulence in the mid- and upper- troposphere (Staquet and Sommeria, 2002, Lilly, 1978, Wolff and Sharman, 2008). Orographic gravity waves can also break in the stratosphere (see e.g., Shutts *et al.*, 1988, Smith *et al.*, 2008) and play a role in the formation of Arctic and Antarctic polar stratospheric clouds with consequences for ozone depletion (see e.g., Carslaw *et al.*, 1999, Alexander *et al.*, 2011, Alexander *et al.*, 2013). Also, there exists evidence of mountain wave activity in the mesosphere and even lower thermosphere, where it drives fluctuations of the horizontal wind and changes in the atmospheric dynamics (by wave momentum deposition) and chemical composition (by mixing and redistribution of chemical species like oxigen and ozone) (see e.g., Garcia and Solomon, 1985, Miyoshi and Fujiwara, 2008, Smith *et al.*, 2009).

Mountain waves not only exist in the atmosphere, but also in the oceans where they are excited by tidal flows over bottom topography. Just like in the atmosphere, internal waves in the ocean can break and produce turbulent mixing of heat and solutes (Staquet and Sommeria, 2002, Ferrari and Wunsch, 2009).

Finally, orographic gravity waves have been recently detected in the atmosphere of Venus (Bertaux *et al.*, 2016, Fukuhara *et al.*, 2017). Their formation can provide hints

[1]Note that expressions like "orographic gravity waves, model, simulations" etc. were excluded in the generation of the word cloud.

on the atmospheric structure of the planet at lower altitudes and, similarly to what happens on Earth, how their breaking can influence Venus's atmospheric circulation.

The most evident and direct way in which mountain waves impact us all is probably through generation of aviation-scale turbulence. For example, on 30 December 2015 an Air Canada flight encountered severe mountain wave turbulence over Alaska. Passengers reported that turbulence lasted about 40 min and the flight made an emergency landing. In the aftermath of the incident 21 passengers were hospitalized (The Globe and Mail, 2015). More recently, on 27 February 2017 an American Airlines flight to Chicago made an emergency landing in Denver, after having encountered severe turbulence over the Rocky Mountains. 5 passengers were injured and 2 were transported to a local hospital (The Weather Channel, 2017).

Turbulence encounters represent about 65% of all weather-related commercial aircraft incidents, and an estimation has been made of tens of millions dollars a year paid out by airlines for injury-related claims by passengers (Sharman *et al.*, 2006). Mountain wave breaking is, of course, not the sole responsible for aviation turbulence. However, it is a major contributor to the upper-level turbulence over the western half of the United States (Wolff and Sharman, 2008), and air-spaces over large topographic features (such as Rocky Mountains, Andes or Alps) are known to be 'hot spots' of mountain wave turbulence (MWT). Greenland, for instance, is recognized to be a prolific source of MWT in the lower stratosphere (Sharman and Lane, 2016). A few examples of studies on turbulence generation by mountain wave breaking are: Jiang and Doyle (2004) where the authors study gravity wave breaking over the central Alps, Doyle *et al.* (2005), which investigates a large-amplitude mountain wave breaking event over Greenland, Ágústsson and Ólafsson (2014), which presents an investigation of a commercial aircraft encounter with severe turbulence over the south-eastern coast of Iceland, and Strauss *et al.* (2015) where turbulence generated over the Medicine Bow Mountains (in southeast Wyoming, USA) is studied.

1.2 Motivation

Currently, airlines use turbulence forecasts, pilot reports (PIREPs) and real-time weather observations (radar, satellite etc.) to plan safe routes. If mountain wave activity is forecasted or reported, Delta Air Lines, for example, adopts a mountain wave avoidance system for which pilots can either avoid selected altitudes, or avoid the steep terrain area (Sharman and Lane, 2016). Obviously, the success of avoidance procedures rely on the robustness of turbulence detection and forecasting techniques.

At present, mountain wave turbulence is one of the most challenging forms of Clear-Air Turbulence (CAT) to forecast. Indeed, several mechanisms and environmental conditions can operate independently, or jointly, to cause vertically propagating mountain waves to break at aircraft cruise altitudes. Established mechanisms are: an increase in the wave amplitude as waves propagate upwards in response to a decreasing air density (Eliassen and Palm, 1960), a negative vertical wind shear (i.e. wind speed decreasing with height) that may lead to a layer of zero wind speed (Booker and Bretherton, 1967), environmental critical levels created by a wind direction that changes with height (Broad, 1995), or an abrupt increase in the atmospheric stability (such as the transition from troposphere to stratosphere) (VanZandt and Fritts, 1989).

Of the two World Area Forecast Centers (WAFC), WAFC London and WAFC Washington, only the first one has an algorithm to forecast mountain wave turbulence. This algorithm uses a method developed by Turner (1999), based on the gravity wave drag parameterization adopted in a global weather prediction model. However, when the forecasting skills for the methods used to predict wind shear and convective turbulence events are compared with that of the MWT algorithm, this turns out to be the one that performs worst(Gill and Stirling, 2013).

Recently, Sharman and Pearson (2016) presented a revised Graphical Turbulence Guidance (GTG) system, used by the U.S. Aviation Weather Center, that includes explicit MWT algorithms. Using a combination of MWT and CAT diagnostics, they showed that an ensemble-weighted mean of several diagnostics performs better than any other diagnostic used alone. Overall, these authors achieved a better forecasting skill with their method than using MWT predictors based on a gravity wave drag formulation. Yet, none of their diagnostics takes into account mountain wave breaking induced by directional wind shear.

To a certain extent, we can always expect the wind direction to vary with height. Directional shear flows are ubiquitous in nature, and at least three processes creating (both speed and directional) vertical wind shear can be identified: thermal advection, as is consistent with the thermal wind relation, the balance between friction and rotation within the PBL (a process also known as the "Ekman spiral"), and rapidly moving weather systems (in particular cyclones) (Markowski and Richardson, 2006).

Approximations with constant background flows or speed-only (unidirectional) wind shear are often used in theoretical and idealized numerical studies to simplify the problem when attention needs to be focused on other aspects of the flow dynamics. However, a turning wind not only represents a further complication mathematically,

since introduction of an additional variable (the y-component of the wind vector) is necessary, but it also corresponds to the addition of an independent physical mechanism able to cause wave breaking. In this respect, directional wind shear, by originating directional critical levels where gravity waves increase their amplitude and potentially breakdown into turbulence, represents a mechanism often overlooked in the literature. Its absence in the current MWT algorithms and drag parameterizations may explain part of the biases and inaccuracies shown by our current weather and CAT forecasting tools.

Additionally, with specific regard to orographic drag, the existence of a directional shear alters the way in which the wave energy and the wave momentum flux are absorbed into the mean-flow. In directional shear flows, and according to linear theory, the wave momentum is selectively deposited at critical levels that are distributed through a continuous range of heights (Teixeira and Miranda, 2009), and not all at once at a same height, chosen in accordance with a saturation criterion (Lindzen, 1981), as it happens in unidirectional or unsheared flows. An accurate representation of orographic wave drag is essential to correctly assess the deceleration of the global atmospheric circulation due to gravity wave breaking.

In this thesis, mountain wave breaking in atmospheric flows with directional wind shear will be investigated. The ultimate goal is to understand the mechanisms by which three-dimensional orographic gravity waves break and generate Clear-Air Turbulence. The aim is to contribute to enhance the accuracy of wave breaking prediction in directional shear flows, with potential impacts not only on CAT forecasts but also on orographic drag model parametrizations. For this purpose, throughout the rest of the thesis, theoretical aspects of the fundamental gravity wave dynamics will be combined with numerical modelling of atmospheric flows over orography.

The research questions of this thesis are:

(a) Under a controlled scenario, how does wave breaking depend on background flow parameters?

(b) Where is turbulence generation expected with respect to the orography that generates the mountain waves?

(c) Is there a way to diagnose this type of turbulence?

(d) How does the stability of the flow to wave breaking change in the transition from hydrostatic to non-hydrostatic mountain waves?

(e) In a real turbulence event, what is the role of directional shear in triggering wave breaking? Can we isolate its contribution?

(f) In Fourier space (i.e., by spatial scale), how is the spectral wave energy distributed at directional critical levels?

In the following chapters, each of these questions will be discussed and possible answers/explanations will be provided. The remainder the thesis is organized accordingly, as detailed in the next section.

1.3 Outline of the thesis

The present thesis comprises 6 chapters. In chapter 2 the physics of mountain waves is briefly reviewed and a concise description of the Weather Research and Forecasting model is provided. This chapter introduces the theoretical and numerical framework of the thesis.

Chapters 3, 4 and 5 correspond to scientific papers that have been published, or are currently under review, as stated at the beginning of each chapter. Each chapter consists of a stand-alone publication in which the research questions of this thesis are addressed as follows: Chapter 3 investigates the generation of atmospheric turbulence due to orographic gravity wave breaking in directional shear flows using idealized 3D numerical simulations of hydrostatic, vertically-propagating mountain waves. The aim is to diagnose wave breaking based on large-scale flow variables and identify regions, within the simulation domain, where wave breaking and the development of Clear-Air Turbulence are expected. Besides inviscid simulations, numerical simulations where turbulence is parameterized are presented. The dynamics of the horizontal velocity perturbations associated with the waves in Fourier space is also examined, with a focus on possible links between wave breaking and the relative orientations of the incoming wind vector and the horizontal velocity perturbation vector. This chapter constitutes the starting point of the research presented in chapters 4 and 5. Chapter 4 investigates the effects of the dispersion associated with non-hydrostatic mountain waves on wave breaking. In this chapter, causes for the observed changes in flow static and dynamic stability (as evaluated by the Richardson number) in the transition from hydrostatic to non-hydrostatic mountain waves are discussed. In chapter 5 the role of directional critical levels in causing a real turbulence event over the Rocky Mountains, in the state of Colorado, USA, is investigated. In particular,

critical levels induced by directional shear are studied by spectral analysis of the horizontal velocity perturbations. This type of analysis allows us to evaluate changes in the wave energy distribution by wave-number at critical levels.

Chapter 6 concludes the thesis by summarizing the main results obtained, pointing out their wider implications and limitations, and discussing possible directions for future research.

Chapter 2

Methodology: theoretical and numerical aspects

2.1 The physics of mountain waves

The problem of the stability of flows in which density varies with height was first addressed by Taylor (1931) and Goldstein (1931). They independently derived an equation, known as Taylor-Goldstein (TG) equation, that describes the stability of stratified flows and governs the propagation of mountain waves in the atmosphere. In this section, the Taylor-Goldstein equation is derived from the Euler equations of fluid flows. Possible solutions of the TG equation, relevant to the purposes of this thesis, are also presented. Additionally, the linear scaling of key flow parameters is introduced.

2.1.1 The Taylor-Goldstein equation

The Taylor-Goldstein equation is derived by linearizing the governing equations of fluid dynamics. The linerization method requires any generic variable $q(x, y, z, t)$ to be expressed as the sum of a background state $q_0(z)$, assumed to be steady and horizontally uniform, and a perturbation $q_1(x, y, z, t)$. Under the assumption that perturbations are small compared to the background flow, the products of the perturbations are negligible and the governing equations can be simplified accordingly. If we consider the background flow to be in hydrostatic balance, the linearized governing equations for a three-dimensional, Boussinesq, frictionless and adiabatic flow

without rotation are (Nappo, 2012):

$$\frac{\partial u_1}{\partial t} + u_0\frac{\partial u_1}{\partial x} + v_0\frac{\partial u_1}{\partial y} + w_1\frac{\partial u_0}{\partial z} = -\frac{1}{\rho_0}\frac{\partial p_1}{\partial x}, \tag{2.1}$$

$$\frac{\partial v_1}{\partial t} + u_0\frac{\partial v_1}{\partial x} + v_0\frac{\partial v_1}{\partial y} + w_1\frac{\partial v_0}{\partial z} = -\frac{1}{\rho_0}\frac{\partial p_1}{\partial y}, \tag{2.2}$$

$$\frac{\partial w_1}{\partial t} + u_0\frac{\partial w_1}{\partial x} + v_0\frac{\partial w_1}{\partial y} = -\frac{1}{\rho_0}\frac{\partial p_1}{\partial z} + \frac{\theta_1}{\theta_0}g, \tag{2.3}$$

$$\frac{\partial u_1}{\partial x} + \frac{\partial v_1}{\partial y} + \frac{\partial w_1}{\partial z} = 0, \tag{2.4}$$

$$\frac{\partial \theta_1}{\partial t} + u_0\frac{\partial \theta_1}{\partial x} + v_0\frac{\partial \theta_1}{\partial y} + w_1\frac{\partial \theta_0}{\partial z} = 0. \tag{2.5}$$

where $u = u_0 + u_1$ and $v = v_0 + v_1$ are the wind components in the x- and y- directions, $p = p_0 + p_1$ is the pressure and $\theta = \theta_0 + \theta_1$ is the potential temperature of the flow decomposed in their mean and perturbation parts. $w = w_1$ is the vertical perturbation velocity, g is the gravity acceleration, and ρ_0 is the background atmospheric density.

Equations (2.1) - (2.3) are the three components of the momentum equation, equation (2.4) is the mass continuity equation and equation (2.5) is the heat budget equation. By taking a double Fourier transform and assuming that the flow is stationary, (2.1) - (2.5) become:

$$u_0 ik\widehat{u}_1 + v_0 il\widehat{u}_1 + \widehat{w}_1\frac{\partial u_0}{\partial z} = -\frac{1}{\rho_0} ik\widehat{p}_1, \tag{2.6}$$

$$u_0 ik\widehat{v}_1 + v_0 il\widehat{v}_1 + \widehat{w}_1\frac{\partial v_0}{\partial z} = -\frac{1}{\rho_0} il\widehat{p}_1, \tag{2.7}$$

$$u_0 ik\widehat{w}_1 + v_0 il\widehat{w}_1 = -\frac{1}{\rho_0}\frac{\partial \widehat{p}_1}{\partial z} + \frac{\widehat{\theta}_1}{\theta_0}g, \tag{2.8}$$

$$ik\widehat{u}_1 + il\widehat{v}_1 + \frac{\partial \widehat{w}_1}{\partial z} = 0, \tag{2.9}$$

$$u_0 ik\widehat{\theta}_1 + v_0 il\widehat{\theta}_1 + \widehat{w}_1\frac{\partial \theta_0}{\partial z} = 0. \tag{2.10}$$

where the hat ($\widehat{\ }$) symbol is used to denote the Fourier transforms.

Equations (2.6) - (2.10) can be combined into a single equation by: differentiating with respect to z (2.6) and (2.7), using (2.8) in $\partial(2.6)/\partial z$ and $\partial(2.7)/\partial z$ to eliminate $\widehat{p}_1$, using (2.10) in (2.8) to eliminate $\widehat{\theta}_1$ and finally using (2.9) to eliminate $\widehat{u}_1$ and $\widehat{v}_1$.

This yields the following equation for $\widehat{w}_1$:

$$\frac{d^2\widehat{w}_1}{dz^2} + \left[\frac{N_0^2(k^2+l^2)}{(ku_0+lv_0)^2} - \frac{ku_0''+lv_0''}{ku_0+lv_0} - (k^2+l^2)\right]\widehat{w}_1 = 0 \tag{2.11}$$

where the primes denote differentiation with respect to z and $N_0^2 = \frac{g}{\theta_0}\frac{\partial\theta_0}{\partial z}$ is the squared Brunt-Väisälä frequency of the background flow.

The first term in the brackets in (2.11) is called buoyancy term and regulates the wave amplitude as a function of the atmospheric stability, the second term is the shear term and takes into account the variation of u_0 and v_0 with height, the last term is called non-hydrostatic term and it is only present in the equation when the vertical velocity perturbations are not in hydrostatic balance (i.e., when the vertical acceleration is sufficiently large).

Equation (2.11) is the Taylor-Goldstein equation and governs the vertical structure of the wave perturbation. Analogously, equations for the horizontal velocity perturbations can be derived by using (2.6), (2.7) and (2.9). In particular, $\widehat{u}_1$ and $\widehat{v}_1$ can be found by multiplying (2.6) by l and (2.7) by k, and subtracting the first equation from the second one (i.e. k(2.7) - l(2.6)) to eliminate the pressure $\widehat{p}_1$. Note that this is equivalent to differentiating (2.1) with respect to y and (2.2) with respect to x before taking the Fourier transform and, thus, effectively computes the vertical component of the vorticity equation. The mass continuity equation is then used to solve a system of two equations for three variables ($\widehat{u}_1$, $\widehat{v}_1$, $\widehat{w}_1$) to find:

$$\widehat{u}_1(k,l,z) = \frac{ik}{k^2+l^2}\left[\frac{l\widehat{w}(lu_0'-kv_0')}{k(ku_0+lv_0)} + \frac{\mathrm{d}\widehat{w}}{\mathrm{d}z}\right], \tag{2.12}$$

$$\widehat{v}_1(k,l,z) = \frac{-il}{k^2+l^2}\left[\frac{k\widehat{w}(lu_0'-kv_0')}{l(ku_0+lv_0)} - \frac{\mathrm{d}\widehat{w}}{\mathrm{d}z}\right]. \tag{2.13}$$

The equations presented in this section describe the oscillatory motion of stationary gravity waves according to linear theory, and away from singularities for which their solution would diverge.

Singularities in the wave equation (2.11) correspond to physical heights in the atmosphere known as "critical levels". At these heights the wave motion is no longer supported and waves are expected to stop propagating by breaking (once their amplitude increases enough that linear theory breaks down) or being absorbed into the mean flow (for very small amplitude waves, in a process that can be described by linear theory). Critical levels are thus of primary importance in the study of wave breaking. In the following chapters, the behaviour of (2.11), (2.12) and (2.13) at

critical levels will be discussed and used to interpret the results of the numerical simulations.

2.1.2 A zeroth- and first- order WKB solution of the TG equation

In the simplest scenario of hydrostatic mountain waves and constant background parameters, the second and the third term in the brackets in (2.11) are equal to zero. Thus, the Taylor-Goldstein equation has the general solution:

$$\widehat{w}_1 = \widehat{w}_1(z=0)\mathrm{e}^{imz}, \tag{2.14}$$

where the vertical wave-number m is given by:

$$m = \frac{N_0(k^2+l^2)^{1/2}}{(ku_0+lv_0)}, \tag{2.15}$$

and $\widehat{w}_1(z=0)$ is prescribed by the no-normal flow lower boundary condition, for which the flow must be parallel to the surface:

$$\widehat{w}_1(z=0) = i(ku_0+lv_0)\widehat{h}, \tag{2.16}$$

where $\widehat{h}$ is the Fourier transform of the terrain elevation $h(x,y)$.

A constant background flow is rare and solution (2.14) is often dismissed in applications to real flows. For flows where wind and stratification vary with height, the solution to (2.11) can be expressed as:

$$\widehat{w}_1 = \widehat{w}_1(z=0)\mathrm{e}^{i\int_0^z m(z)\mathrm{d}z}. \tag{2.17}$$

Substituting (2.17) in (2.11) yields:

$$im' - m^2 + \frac{N_0^2(k^2+l^2)}{(ku_0+lv_0)^2} - \frac{ku_0''+lv_0''}{ku_0+lv_0} - (k^2+l^2) = 0 \tag{2.18}$$

An expression for m can be obtained by adopting a WKB approximation (see, e.g., Bender and Orszag (2013)). The WKB method (named after physicists Wentzel, Kramers, and Brillouin) allows one to find an approximate solution to the Taylor-Goldstein equation for a slowly varying medium (i.e. the solution is only valid for gradual variations of u_0, v_0, and N_0 with height). This method has been widely

used in meteorology applications (e.g. Grisogono (1994), Broad (1995), Teixeira and Miranda (2009)), and entails representing the vertical wave-number as a sum of powers of a small parameter ε. The WKB method also requires, for a consistent scaling of the various terms in the equation, vertical derivatives to be multiplied by the same parameter ε (which effectively corresponds to an appropriate rescaling of the vertical coordinate). Following Teixeira *et al.* (2004), and using a series expansion of m truncated at first-order (i.e. $m = m_0 + \varepsilon m_1$), (2.18) becomes:

$$i\varepsilon(m_0 + \varepsilon m_1)' - (m_0 + \varepsilon m_1)^2 + \frac{N_0^2(k^2 + l^2)}{(ku_0 + lv_0)^2} - \varepsilon^2 \frac{ku_0'' + lv_0''}{ku_0 + lv_0} - (k^2 + l^2) = 0 \quad (2.19)$$

Neglecting higher-than-first-order terms in ε and combining terms of the same order, we obtain:

$$m_0 = \left[\frac{N_0^2 k_H^2}{(ku_0 + lv_0)^2} - k_H^2 \right]^{1/2}, \quad (2.20)$$

$$m_1 = \frac{1}{2} i \frac{m_0'}{m_0}. \quad (2.21)$$

When a solution of the TG equation is approximated using a zeroth-order WKB approximation, in (2.17) $m = m_0$. When using a first-order approximate solution, (2.17) becomes:

$$\widehat{w}_1 = \widehat{w}_1(z = 0) \mathrm{e}^{i \int m_0(z) \mathrm{d}z} \mathrm{e}^{i \int m_1(z) \mathrm{d}z}. \quad (2.22)$$

But using (2.21), this can be expressed as:

$$\widehat{w}_1 = \widehat{w}_1(z = 0) \left| \frac{m_0(z = 0)}{m_0(z)} \right|^{1/2} \mathrm{e}^{i \int_0^z m_0(z) \mathrm{d}z} \quad (2.23)$$

Both using a zeroth- or first-order WKB approximation, m is expressed in the same form as for a constant wind case but N_0, u_0 and v_0 are allowed to vary (slowly) with height.

The zeroth- and the first order solutions will be used in the following chapters of the thesis in the discussion of results.

2.1.3 The scaling of key flow parameters

In this section the scalings of the horizontal and vertical velocity perturbations for hydrostatic and non-hydrostatic mountain waves are discussed. These scaling properties will be used in Chapter 4 to investigate non-hydrostatic effects on mountain

wave breaking.

Because the horizontal velocities u_0, v_0 scale in the same way, the scale analysis will be performed in 2D, for simplicity. In this case, the vertical wave-number is:

$$m = \left[\frac{N_0^2}{u_0^2} - k^2\right]^{1/2}. \tag{2.24}$$

The scaling of the vertical velocity w_1 excited at the surface is the same for hydrostatic and non-hydrostatic mountain waves, and is dictated by the bottom boundary condition:

$$\widehat{w}_1(z=0) = iku_0\widehat{h} \quad \Rightarrow \quad w_1 \sim U\frac{H}{a} \tag{2.25}$$

where a is the mountain half-width, which determines the dominant horizontal wavelength ($\lambda_x \approx a$) and H is the mountain height.

The scaling of the horizontal velocity perturbations u_1 is, instead, intrinsically related to the vertical wave structure. As will be discussed in more detail in Chapter 4, in the hydrostatic limit ($\frac{N_0}{u_0} \gg k$ in (2.24)) the vertical wave-number is simply $m = N_0/u_0$, and thus the vertical wavelength is $\lambda_z \approx U/N$. Using the continuity equation we find:

$$ik\widehat{u}_1 + \frac{\partial \widehat{w}_1}{\partial z} = 0 \quad \Rightarrow \quad u_1 \sim U\frac{H}{a}\frac{N}{U}a = NH \tag{2.26}$$

In the strongly non-hydrostatic limit ($\frac{N_0}{u_0} \ll k$ in (2.24)) $m = ik$, therefore $\lambda_z \approx a$. This causes u_1 to scale instead as:

$$ik\widehat{u}_1 + \frac{\partial \widehat{w}_1}{\partial z} = 0 \quad \Rightarrow \quad u_1 \sim \frac{w_1}{a}a \sim U\frac{H}{a} \tag{2.27}$$

in the same way as the vertical velocity.

From (2.27) we can see that, for strongly non-hydrostatic mountain waves, the non-linearity of the flow is controlled by the H/a parameter. Indeed, if $H/a > 1$ the wave perturbation is larger than the background flow ($|u_1/U| > 1$). Similarly, from (2.26) we can see that the non-linearity parameter for approximately hydrostatic mountain waves is NH/U, because if $NH/U > 1$ then $|u_1/U| > 1$.

Note that, for readability, in the next chapters a change of notation will be adopted for the horizontal velocity perturbations u_1 and v_1, that will be replaced by u' and v', and the vertical velocity perturbation w_1, to which we will simply refer as w.

2.2 The Weather, Research and Forecasting (WRF) Model

The numerical simulations presented in this thesis were conducted using the Advanced Research - Weather Research and Forecasting (WRF-ARW) model version 3.6. WRF-ARW is a mesoscale model developed by the National Center of Atmospheric Research (CO) that uses an "Eulerian mass core" to solve the non-hydrostatic, fully compressible Euler equations. A comprehensive description of the model can be found in the "NCAR Technical Note" by Skamarock *et al.* (2005), where the reader is directed for details about the integration of the governing equations and the model's discretization. Here we briefly recall that the Euler equations are formulated and solved by the model on a terrain-following hydrostatic-pressure vertical coordinate (proposed by Laprise (1992)). Compared to their traditional form, the governing equations are modified by including moisture and additional terms called "mapping factors" that account for the projection of the computational domain on the Earth's surface. Horizontally, the equations are solved on an Arakawa-C staggered grid (Mesinger *et al.*, 1976).

In this thesis the model was used in its idealized mode. In this model configuration the user is given the choice to run controlled scenarios by including/excluding certain physical processes (i.e. model parametrizations), the Earth's rotation effect, moisture effects, etc. Idealized runs are particularly suitable for dynamical studies aimed at investigating the contribution of single physical processes.

In the following section, details about the initialization of the model are provided.

2.2.1 Idealized model set-up

The model was initialized with a 1D atmospheric sounding including vertical profiles of potential temperature, horizontal wind components and vapour mixing ratio (set to zero to simulate a dry flow). The Coriolis force was switched off and, horizontally, a Cartesian grid was used. Topography specifications, such as changes in the terrain elevation, or in the width, height and shape of the orography were possible via modifications of the model source code. The code was also edited to modify the distribution of the model's vertical levels.

Appropriate boundary conditions were selected to avoid wave reflections in the vicinity of the model's boundaries that could contaminate the interior solution in an

unrealistic way. Laterally, open boundary conditions were used. These boundary conditions are often called "radiative" as they are designed to radiate out of the domain waves and disturbances approaching the boundaries. In WRF, open lateral boundary conditions are implemented following the approach proposed by Klemp and Lilly (1978) and Klemp and Wilhelmson (1978). According to this approach, outward propagating waves are allowed to leave the computational domain through a lateral boundary by locally replacing the momentum equation (for instance along the west-east boundary) with:

$$\frac{\partial u}{\partial t} + (u - c_i)\frac{\partial u}{\partial x} = 0 \qquad \text{at} \qquad x = 0 \qquad \text{(inflow boundary)},$$

$$\frac{\partial u}{\partial t} + (u + c_o)\frac{\partial u}{\partial x} = 0 \qquad \text{at} \qquad x = L \qquad \text{(outflow boundary)}.$$

Therefore, the horizontal velocity is advected out of the simulation domain with an estimated phase speed $(u + c_o)$ for gravity waves propagating downstream towards the outflow boundary, and $(u - c_i)$ for gravity waves propagating upstream towards the inflow boundary. The phase speed c is chosen to be representative of the dominant wave-mode in the system, which is usually equivalent to the fastest-propagating internal gravity wave.

Near the upper boundary, an absorbing layer (Rayleigh damping layer) was used to relax u, v, w and θ back to their reference-state values. For example, for the zonal horizontal velocity component, the formulation of the damping layer is (Klemp and Lilly, 1978):

$$\frac{\partial u}{\partial t} = -\tau(z)(u - u_0)$$

where u_0 is the reference state value and $\tau(z)$:

$$\tau(z) = \gamma_r \ \sin^2\left[\frac{\pi}{2}\left(1 - \frac{z_{top} - z}{z_d}\right)\right]$$

γ_r is a user-specified damping coefficient, z_{top} is the height of the model top and z_d is the depth of the damping layer (measured downward from the model top). The expression above is valid only for $z_{top} \leq z \leq z_d$; everywhere else $\tau(z) = 0$. The damping coefficient works in the same way for all the other flow variables.

All the simulations used the dynamical core only, thus no surface processes, planetary boundary layer, micro-physics or radiation parametrizations were employed. The sole

parametrization used in the simulations of Appendix 3.A is described in the next subsection.

2.2.2 The WRF 1.5 order turbulence closure

In this section, a concise description of the 1.5 order turbulence closure used by WRF to parametrize turbulence will be provided. Attention will be focused on the calculation of turbulent kinetic energy produced by shear and buoyancy forces. However, for a detailed description, the reader is referred to Skamarock *et al.* (2005).

In this scheme, the turbulent kinetic energy e is a prognostic variable and the equation governing its evolution is:

$$\frac{\partial(\mu_d e)}{\partial t} + (\nabla \cdot \mathbf{V}e)_\eta = \mu_d(shear\ production + buoyancy + dissipation) \tag{2.28}$$

where μ_d is the mass of dry air in the column, $\mathbf{V}$ is the velocity vector, $(\nabla \cdot \mathbf{V}e)_\eta$ is the "transport term" representing fluxes of turbulent kinetic energy (TKE) on the hydrostatic-pressure terrain-following vertical grid (η).

The time evolution and transport of TKE are therefore computed taking into account source (shear and buoyancy production) and sink (dissipation) terms.

The production of TKE by shear forces is parametrized as follows:

$$shear\ production = K_h D_{11}^2 + K_h D_{22}^2 + K_v D_{33}^2 + K_h \overline{D_{12}^2}^{xy} + K_v \overline{D_{13}^2}^{x\eta} + K_v \overline{D_{23}^2}^{y\eta}. \tag{2.29}$$

D_{11}, D_{22}, D_{33}, D_{12}, D_{13}, D_{23} are the 6 independent components of the deformation tensor as defined in Skamarock *et al.* (2005). Note that only 6 (out of 9) components of the tensor are considered, as the deformation tensor is symmetric (i.e. $D_{12} = D_{21}$, $D_{13} = D_{31}$, $D_{23} = D_{32}$). The off-diagonal components of the tensor D_{12}, D_{13}, D_{23} are averaged over the grid cell faces in the xy, $x\eta$ and $y\eta$ planes, respectively (denoted by the overbars).

K_h and K_v are the horizontal and vertical eddy viscosities. These are exchange coefficients representing the turbulent transfer of momentum by eddies and are computed using:

$$K_{h,v} = C_k l_{h,v} \sqrt{e} \tag{2.30}$$

where C_k is a constant that controls the physical diffusion (usually in the interval [0.15, 0.25]), and $l_{h,v}$ are the mixing length-scales computed dynamically by the model. An

isotropic length-scale can be used when the horizontal and vertical grid spacings are similar ($\Delta x, \Delta y \simeq \Delta z$). If $\Delta x, \Delta y \gg \Delta z$ an anisotropic option is available. e, whose time evolution is given by (2.28), is first generated by the model using the surface thermal fluxes and the friction velocity computed by the surface layer scheme if this is turned on. For frictionless simulations in which heat fluxes are turned off, the model uses a "TKE seed" to generate turbulent kinetic energy.

The production/destruction of TKE by buoyancy forces is given by:

$$Buoyancy = -K_{v_{heat}} N^2 \tag{2.31}$$

where $K_{v_{heat}}$ is the vertical eddy diffusivity (an exchange coefficient for heat).

The buoyancy term can thus be either negative or positive. When negative, the statically stable atmospheric conditions ($N^2 > 0$) work against the production of TKE, because vertical motions are constrained by the restoring buoyancy force. On the contrary, when the buoyancy term is positive, the presence of a negative vertical gradient of potential temperature ($N^2 < 0$) favours the growth of turbulent motions by static instability.

The relative contributions of shear and buoyancy production to the total TKE in the numerical simulations will be discussed in Appendix A of Chapter 3. As the dissipation term does not take part in this analysis, the reader is referred to Skamarock *et al.* (2005) for details about its formulation.

Chapter 3

Turbulence generation by mountain wave breaking in flows with directional wind shear

In this chapter, mountain wave breaking, and the resulting potential for the generation of turbulence in the atmosphere, are investigated using numerical simulations of idealized, nearly hydrostatic atmospheric flows with directional wind shear over an axisymmetric isolated mountain. These simulations, which use the WRF-ARW model, differ in degree of flow non-linearity and shear intensity, quantified through the dimensionless mountain height and the Richardson number of the incoming flow, respectively. The aim is to diagnose wave breaking based on large-scale flow variables.

The work presented in this chapter was published in the *Quarterly Journal of the Royal Meteorological Society*, with the reference:
Guarino MV, Teixeira MAC, Ambaum MHP, 2016. Turbulence generation by mountain wave breaking in flows with directional wind shear. Q. J. R. Meteorol. Soc. **142**: 2715 - 2726.

In Appendix 3.A, further experiments where turbulence is parametrized using a 1.5-order turbulence closure are presented. They constitute an extension of the work included in Guarino *et al.* (2016).
In Appendix 3.B, preliminary tests of a possible wave breaking diagnostic based on ideas sketched in the chapter are discussed.

3.1 Introduction

The role of orographic gravity waves, or mountain waves, in weather and climate studies is widely recognized. These waves are generated when stably stratified air masses are lifted by flow over orography. Under favourable atmospheric conditions (in terms of atmospheric stability and wind speed profiles) and lower boundary conditions (imposed by the terrain elevation), mountain waves can break. Breaking waves affect the atmospheric circulation by deposition of wave momentum into the mean flow (Lilly and Kennedy, 1973), which manifests itself as a drag force acting on the atmosphere. Wave breaking also poses a serious safety hazard to aviation through Clear-Air Turbulence (CAT) generation (Lilly, 1978). This form of CAT can be quite severe and usually occurs at altitudes relevant for general and commercial aviation (i.e., within the troposphere and lower stratosphere) (Sharman *et al.*, 2012a). However, presently, techniques to forecast CAT generated by mountain wave breaking are still not sufficiently accurate (Sharman *et al.*, 2012b).

While the conditions for mountain wave breaking for a constant or unidirectionally sheared background wind have been studied in substantial detail, the more common case of wave breaking occurring in winds that turn with height (i.e., with directional shear) remains incompletely understood.

Directional shear flows are ubiquitous in the atmosphere. Throughout most of the mid-latitudes, the low-level shear vector turns anticyclonically with height (Lin, 2007). Directional shear is often linked to thermal advection through the thermal wind relation. Indeed, in presence of a temperature gradient, a geostrophically-balanced flow will align itself with the isotherms by turning clockwise with height in the case of warm advection, and counter-clockwise with height in the case of cold advection (Holton and Hakim, 2012). Directional wind shear can also be associated with long-period inertia-gravity waves (Mahalov *et al.*, 2009). An example of observed mountain wave breaking in the presence of directional wind shear over the French Alps was reported by Doyle and Jiang (2006).

In the simpler case of an unsheared flow over 2D orography, wave breaking conditions are essentially controlled by the value of the dimensionless mountain height N_0H/U. Linear theory breaks down when N_0H/U is large, but it can be used to obtain a rough estimate of the critical dimensionless mountain height for which the streamlines become vertical (i.e., flow overturning occurs), and hence wave breaking is expected. This critical value is $N_0H/U = 1$ for hydrostatic flow with the Boussinesq approximation over a bell-shaped ridge, defining an absolute limit of applicability of the linear

solutions, since the velocity perturbation u' is then no longer small, but has the same magnitude as the background flow velocity U. As shown in previous studies (Baines (1998), Ambaum and Marshall (2005)), it is possible to identify different flow types based on the value of the dimensionless mountain height N_0H/U and the mountain aspect ratio H/a (where a is the mountain half-width), for which the magnitudes of u' and U become comparable, leading to flow separation. In particular, for a mountain aspect ratio $H/a \ll 1$ (i.e., hydrostatic flow) and a N_0H/U larger than 1, flow separation occurs just downstream the mountain (post-wave separation).

Long (1953) developed a non-linear theory for similar 2D flows (featuring a linear equation but a non-linear lower boundary condition), which predicts the critical mountain height for hydrostatic flow overturning over a bell-shaped ridge to be instead $N_0H/U = 0.85$ (Miles and Huppert, 1969). This value limits Long's model validity, not because of the magnitude of the flow perturbation (which could be arbitrary large), but because wave breaking is expected beyond this threshold, which violates the steady-state assumption.

Smith (1989) used linear theory to study stratified flow past a 3D isolated mountain. For an unsheared and hydrostatic flow with the Boussinesq approximation over a mountain of sufficiently high amplitude, linear theory predicts two stagnation points (one on the windward slope of the mountain and the other one above the mountain top). Flow stagnation aloft is a precursor to overturning of isentropic surfaces (which replace streamlines in 3D flow) and therefore wave breaking. Smith formulated a condition for flow stagnation in terms of a critical dimensionless mountain height, above which the flow splits at the surface or overturns aloft. For the unsheared cases he considered, this only depends on the horizontal aspect ratio of the mountain (which controls directional dispersion effects).

As we consider more realistic flow setups (no Boussinesq approximation, and wind profiles with vertical shear, but still approximately hydrostatic conditions), there are basically two additional physical mechanisms that contribute to mountain wave breaking apart from the orography amplitude: the decay of density with height and vertical shear in the wind profile.
The effect of the decay of density with height is fairly straightforward, relying on conservation of the momentum flux as the wave propagates upward (in accordance with the theorem formulated by Eliassen and Palm (1960)), whereby a decrease in density corresponds to an increase in the amplitude of the wave velocity perturbations. This mechanism is currently included in drag parametrizations, based on the theory developed by McFarlane (1987).

The effect of vertical wind shear in unidirectionally sheared flows is also fairly straightforward. When the background wind decreases to zero, in what is usually termed a critical level, this always causes, no matter how small the waves are at their source, an indefinite increase in the wave amplitude as they approach the critical level, which necessarily results in flow overturning (Nappo, 2012). This mechanism, which is associated with a divergence of the wave momentum flux, is also incorporated in current drag parametrizations (e.g. Lott and Miller (1997)).

The much more complicated case of a wind with directional shear over a 3D mountain was first addressed theoretically by Broad (1995) and Shutts (1995). Whereas in unsheared flows the surface amplitude of the wave excited by the mountain is the sole responsible for fulfilment of the wave breaking condition, and in unidirectional sheared flows critical levels affect the whole wave spectrum at once at discrete heights, always leading to wave breaking, in directional shear flows the situation is more complicated. Turning of the background wind vector with height creates a continuous distribution of critical levels in the vertical where the wave energy is absorbed into the background flow, which only affect one wave-number in the wave spectrum at a time (i.e., at each level). This effect is currently not represented in drag parametrizations, although its role in determining mountain wave drag has been pointed out in several studies (e.g. Teixeira and Miranda (2009), Xu *et al.* (2012), Xu *et al.* (2013)).

While wave breaking is thought to occur also in winds that turn with height (Broad, 1995), it is weaker and distributed vertically. Since the background flow no longer needs to stagnate at critical levels, but rather is perpendicular to the affected wave-numbers, there are also indications that flow overturning may occur at considerable horizontal distances from the mountain that generates the waves (Shutts and Gadian, 1999). Therefore, the distribution of critical levels and of wave breaking with height is very sensitive to the background wind profile.

In flow over a 3D mountain, with or without shear, the vertically propagating mountain waves weaken aloft because of directional dispersion associated with the spreading of the wave pattern around the mountain (if the flow is substantially non-hydrostatic additional dispersion effects arise). This decay with height, which does not exist in flow over a 2D mountain, is counteracted by the decrease of air density with height and other processes, including critical levels, which cause the wave amplitude to increase. It is the balance between all these processes that will determine the occurrence of wave breaking or not. Furthermore, in flow over 3D mountains, wave breaking is made less likely by flow splitting around the mountain near the surface. If much of the flow is diverted along the mountain flanks, the wave field aloft will weaken and

wave breaking may be limited or totally suppressed (Miranda and James, 1992). This is a process that occurs at high N_0H/U and is obviously absent in flow over 2D ridges.

Following previous studies (Shutts and Gadian (1999), Teixeira *et al.* (2004)), the wind profile employed here assumes that both the magnitude and the rate of rotation of the wind vector with height are constant. Even though it is not particularly realistic, this idealized wind profile can be considered a prototype of flows with directional wind shear, enabling us to isolate the effect of background shear on wave breaking and encapsulate it in a single dimensionless parameter, the Richardson number, which furthermore is constant. Teixeira *et al.* (2004) showed that the curvature of the velocity profile associated with this type of wind profile increases the surface drag. This may have implications for wave breaking, since a larger amount of momentum flux is then available to be transferred to the other flow components (mean flow or turbulence) (Teixeira and Miranda, 2009). The present study is motivated by the fact that even if the wave breaking phenomenology and mechanisms have been fairly well studied, it is still hard to predict when mountain waves will break in directional shear flows. Results from linear theory on this phenomenon are obviously questionable, since wave breaking is an intrinsically non-linear process. So, 3D numerical simulations provide almost the only viable method to understand and predict mountain wave breaking in a systematic way.

In this chapter, turbulence generation due to orographic gravity wave breaking is indirectly studied using such an approach, focusing particularly on the mechanisms by which CAT may be triggered by directional wind shear. High-resolution numerical simulations of idealized flows over a three-dimensional axisymmetric isolated mountain are carried out using the Weather Research and Forecasting model (WRF-ARW version 3.6). The aim is to diagnose the conditions for mountain wave breaking in terms of the orography elevation and wind shear, quantified by the dimensionless mountain height and the Richardson number of the background flow, respectively.

In section 3.2 details about the simulations, model set-up and diagnosis of wave breaking within the computational domain are presented. In section 3.3, results for wave breaking in directional shear flows are presented and discussed, and the section closes with an interpretation of the behaviour of the wave velocity perturbation observed in the simulations. In section 3.4 the main conclusions of this study are summarized.

3.2 Methodology

3.2.1 Setup of numerical simulations

WRF (Skamarock *et al.*, 2005) is a mesoscale, non-hydrostatic, fully-compressible model whose validity in simulating mountain waves has been tested in previous studies such as Doyle (2004) and Hahn (2007). The model was used in an idealized configuration and the dynamical core only (with no parametrizations) was employed to run the simulations. The simulated flow is adiabatic (with no heat or moisture fluxes from the surface), inviscid (with no explicit diffusion allowed anywhere, and thus no Planetary Boundary Layer), and rotational effects due to the Coriolis force are neglected. The initial conditions were determined using a constant Brunt-Väisälä frequency $N_0 = 0.01\ \ \mathrm{s}^{-1}$, a surface potential temperature $\theta_0 = 293$ K, a mean sea level pressure p_0 =1000 hPa and a westerly background wind $U = 10\ \mathrm{m\,s}^{-1}$ (the magnitude of the wind velocity vector is the same also for the directional wind shear simulations, where only the u and v velocity components change with height). The computational domain comprises 100 grid-points in both the x and $y-$directions, with an isotropic grid spacing $\Delta x = \Delta y = 2$ km. The lateral boundary conditions are open (see section 2.2.1 for details). The lower boundary condition is imposed by assuming a three-dimensional bell-shaped mountain with a circular horizontal cross-section, centred in the middle of the computational domain, defined by:

$$h(x,y) = \frac{H}{\left(\frac{x^2}{a^2} + \frac{y^2}{a^2} + 1\right)^{3/2}}, \tag{3.1}$$

where a is the mountain half-width and H is the maximum mountain height. In order to simulate a nearly hydrostatic flow, the mountain half-width was kept fixed at 10 km in all the simulations, which corresponds to $N_0 a/U = 10$.

The model grid comprises 200 eta levels (using a terrain-following hydrostatic-pressure coordinate), with spacing near the ground of 45 m and spacing at the top of the domain, 20 km above ground level (a.g.l.), of 450 m. With such a high vertical resolution the gravity waves generated by the mountain, having a vertical wavelength of about 6 km, are everywhere well resolved (both at lower levels and at the top of the domain where the grid is coarser). An absorbing sponge layer at the top of the domain (above 15 km a.g.l.) was used to control wave reflection from the upper boundary.

The model spin-up time was estimated as 6 hours by evaluating the time evolution of the surface pressure drag. The drag attains a steady state (with an approximately constant value) roughly after that time. A total of 35 simulations were run. Each simulation is 24-hours long and the model was set up to produce outputs with an hourly frequency. The simulations differ in degree of flow non-linearity and directional wind shear intensity. For each model run the initial conditions were modified by varying the non-dimensional mountain height N_0H/U, which determines the amplitude of the orographic gravity waves at the source, and the Richardson number of the background flow $\mathrm{Ri}_{\mathrm{in}}$, which determines the strength of the directional wind shear.

The N_0H/U parameter was gradually increased by varying the mountain height H (keeping N_0 and U constant) and the Richardson number of the incoming flow $\mathrm{Ri}_{\mathrm{in}}$ was decreased successively by a factor of two. More specifically, the values considered for these dimensionless parameters are: $N_0H/U = 0.1$, 0.2, 0.5, 0.75, 1 and $\mathrm{Ri}_{in} = \infty$, 16, 8, 4, 2, 1, 0.5 .
In general, the gradient Richardson number is defined by:

$$\mathrm{Ri} = \frac{N^2}{\left(\frac{\partial u}{\partial z}\right)^2 + \left(\frac{\partial v}{\partial z}\right)^2}, \tag{3.2}$$

where N, u and v are the total Brunt-Väisälä frequency and wind velocity components (including wave perturbations). Denoting the background wind by $\mathbf{U} \equiv (u_0, v_0, 0)$, in the case of flows with no shear, $v_0 = 0$ and $u_0 = U$, which is constant with height, thus $\mathrm{Ri}_{\mathrm{in}} = \infty$. In the case of flows with directional shear, the u_0 and v_0 components are calculated at each model level based on $\mathrm{Ri}_{\mathrm{in}}$, as follows:

$$u_0 = U\cos(\beta z), \qquad v_0 = U\sin(\beta z), \tag{3.3}$$

where $\beta = N_0/(U\sqrt{\mathrm{Ri}_{\mathrm{in}}})$. βz is the angle that the wind vector makes with the eastward direction (i.e., u_0 and v_0 are expressed in polar coordinates), and β is the rate of wind turning with height. By decreasing $\mathrm{Ri}_{\mathrm{in}}$ the rate of turning increases, resulting in a stronger directional wind shear.

Note that since the model is run in an idealized configuration and the Coriolis force is neglected, the atmosphere is not geostrophically balanced and the wind shear is simply prescribed by (3.3), without making use of the thermal wind balance relationship.

3.2.2 Calculation of $\mathbf{Ri_{min}}$ near the mountain

The Richardson number provides information about the flow stability, quantifying the ratio between buoyancy forces and shearing forces. This study relies on the idea that for the simple atmospheric flows presented in the previous section, wave propagation and (when the required conditions are satisfied) the resulting wave breaking are the only reason for the modulation of Ri. The critical condition for wave breaking implies vertical streamlines: in this situation, flow overturning occurs and the local Richardson number becomes zero and then negative (when the potential temperature gradient becomes negative). In order to identify where and when wave breaking occurs in the simulation domain, the Richardson number of the output flow $\mathrm{Ri_{out}}(x, y, z)$ is calculated for each simulation at all grid points using centered finite differences first-order accurate. This Ri corresponds to the quasi-steady mountain wave configuration achieved after the drag stabilizes. This 3D Ri field is then analysed looking for minimum values $\mathrm{Ri_{min}}$. When these values are negative (or lower than than 0.25), turbulence generation by wave breaking (or by shear instability) is assumed to occur in the simulation domain – although turbulence itself is not explicitly modelled at the 2 km horizontal resolution employed here.

The $\mathrm{Ri_{min}}$ values calculated in the Results section below are those falling within a 'region of interest' delimited by upper, lower and lateral bounds selected taking into account physical relevance and computational resource availability considerations. The upper limit of this region is simply dictated by the height of the bottom of the sponge layer employed in the simulations, which is 15 km. A few levels just below the sponge have been neglected to avoid numerical effects due to its proximity. The upper limit is, therefore, $z \approx 14\,\mathrm{km}$. The lower limit is chosen to avoid atmosphere-ground interactions that may develop in frictionless simulations and that are not relevant to the purposes of the present study. Indeed, even in a frictionless setup, the nature of 3D flow near the ground (as described by Smith (1980) and, more recently, by Knight *et al.* (2015)) will lead to low Ri values near the surface, due to sinking of warm air from aloft in response to the lateral deflection of the flow streamlines (i.e. incipient flow splitting). Such low Ri values, not associated with wave propagation, are neglected by excluding in the analysis of the $\mathrm{Ri_{out}}$ field the first levels above the ground that, in reality, would be located within the Planetary Boundary Layer (PBL). In order to assess which maximum height the PBL can reach in the atmospheric conditions considered in the frictionless simulations, simulations with the same setup but including a PBL parametrization (the YSU-PBL scheme) were run. The maximum PBL height reached, evaluated at the last hour of simulation (when the PBL is fully developed), was approximately 1 km. The effect of the PBL

on the Richardson number was clearly recognizable by the presence of a continuous layer of low Ri which extended up to the first km of the atmosphere (not shown). A PBL height of 1 km is reasonable considering that the simulated atmosphere is stable and no surface heat fluxes exist so no thermally-driven turbulence can contribute to the PBL growth. For all the simulations run, with and without wind shear, 1 km is the lowest height used for determining $\mathrm{Ri}_{\mathrm{min}}$. Any process that occurs below this level would be changed by the presence of the PBL.

Several studies on both 2D and 3D flows (see for example Ólafsson and Bougeault (1997) and Peng and Thompson (2003)) have pointed out that the primary effect of surface friction on mountain waves is to decrease the wave amplitude by smoothing the lower boundary condition and hence making wave breaking less likely. Indeed, as Ólafsson and Bougeault (1997) first noted considering different mountain heights, and subsequently Peng and Thompson (2003) confirmed for different mountain widths, the presence of a boundary layer extends the validity of linear solutions in the free atmosphere (with which we are concerned here), by making flow over higher mountains behave as invicid flow over lower (or broader) mountains (see Peng and Thompson (2003)). Furthermore, the effect of the boundary layer depends on its depth, structure and stratification (stably stratified or convective boundary layers can interact with mountain waves in significantly different ways (Jiang and Doyle, 2008)). Inviscid simulations avoid these additional complications by addressing a generic situation, which may be easily made more realistic via a suitable adjustment of the lower boundary condition.

Finally, a square region surrounding the mountain, corresponding to 50 km to the east, west, north and south from the centre of the mountain, has been chosen as lateral limit. These lateral boundaries are applied only for the wind shear simulations. Using linear theory, Shutts (1998) demonstrated the existence of a so-called 'asymptotic wake' trailing away from the mountain in directional shear flows. This flow structure is due to the presence of a component of the wind parallel to the wave phase lines, which causes the wave energy to be advected indefinitely away from the mountain. In numerical simulations, this translates into a wave field that extends out of the computational domain. As a consequence, wave breaking events can often be detected at the edge of the domain. Trying to contain the entire wave field into the simulation domain would require increasing considerably its size and the associated computational costs. Even so, the robustness of the results would not be guaranteed because this asymptotic wake seems to be able to extend indefinitely. Thus, the analysis of results will focus on the region surrounding the mountain where the phenomena taking place (including wave breaking) could be, in realistic conditions

with complex orography, clearly attributed to the presence of the mountain under consideration (and not, for example, to other nearby mountains).

3.3 Results and discussion

Within the 'region of interest' defined in the previous section, $\mathrm{Ri_{min}}$ values were determined for the 35 numerical simulations carried out. Table 3.1 and Table 3.2 contain the results obtained for two representative cases: $\mathrm{Ri_{in}} = \infty$ and $\mathrm{Ri_{in}} = 8$, respectively. For each simulation the N_0H/U values used in input are specified, and the $\mathrm{Ri_{min}}$ position on the horizontal and vertical grid in the output flow are shown. These results are presented using tables given the importance attached to the exact numerical value of $\mathrm{Ri_{min}}$, on which some relevant considerations can be made. However, a complete overview of the results obtained in all the simulations will be provided below using a more comprehensive regime diagram.

TABLE 3.1: The $\mathrm{Ri_{min}}$ values found for the simulation with $\mathrm{Ri_{in}} = \infty$. X and Y give the horizontal position where the minimum Richardson number values occur (the mountain is located at the centre of the domain $X = 0$, $Y = 0$). The altitude in meters is also indicated.

H (m)	N_0H/U	Altitude (m)	Y (km)	X (km)	Ri $_{\mathrm{min}}$
100	0.1	2041	- 2	4	344.80
200	0.2	1577	0	6	83.04
500	0.5	1357	0	8	10.30
750	0.75	1444	0	8	3.50
1000	1	1650	0	8	1.40

TABLE 3.2: As Table 3.1 but for the simulation with $\mathrm{Ri_{in}} = 8$.

H (m)	N_0H/U	Altitude (m)	Y (km)	X (km)	Ri $_{\mathrm{min}}$
100	0.1	5358	50	- 24	4.65
200	0.2	5429	50	- 24	3.00
500	0.5	5642	50	- 28	0.94
750	0.75	6014	50	- 36	0.20
1000	1	6391	40	- 36	-1523.17

3.3.1 Simulations without wind shear

Analysis of the 3D $\mathrm{Ri_{out}}$ field for the no-shear case showed, as expected, that the vertical wave propagation modulates the total Richardson number of the flow, decreasing its value by increasing the wind shear and modifying the stability in some regions. All the minimum values are located directly above the mountain or slightly downstream, as shown by the sketch in Figure 3.1(a). This result is expected: mountain waves transport energy vertically. When the wave perturbations are in hydrostatic balance, this energy transport is upward directly above the mountain.

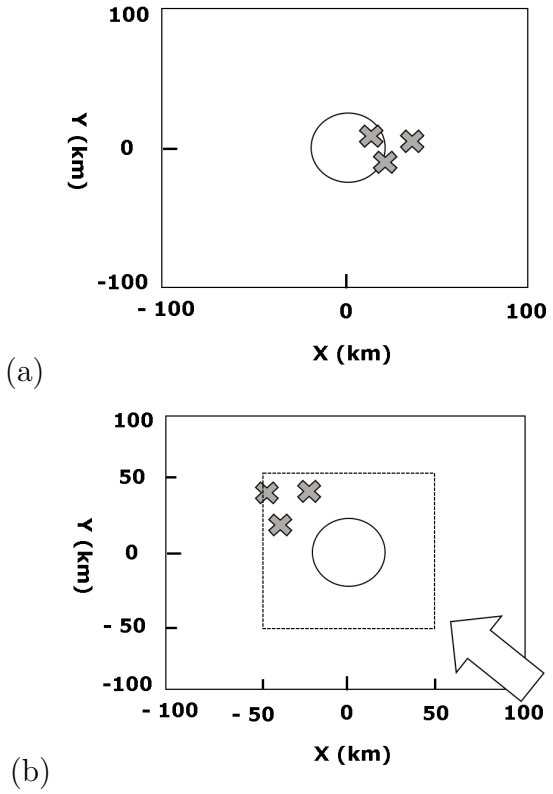

FIGURE 3.1: Sketch of the computational domain showing the location of the $\mathrm{Ri_{min}}$ values (crosses) for the simulations with $\mathrm{Ri_{in}} = \infty$ (a) and $\mathrm{Ri_{min}} = 8$ (b), according to Tables 3.1 and 3.2. The circle represents the mountain. In (b) the arrow denotes the background wind direction at the level where wave breaking is detected, and the region within the square represents the 'region of interest' defined in section 3.2.2. Both sketches refer to the $N_0H/U = 1$ simulations only.

For small-amplitude mountains ($H = 100$ m, $H = 200$ m), while being perturbed by the wave, the Richardson number values are very high. For larger mountain heights ($H = 500$ m, $H = 750$ m, $H = 1$ km) the flow becomes more nonlinear and the Ri values decrease down to a minimum of 1.4 (see Table 3.1) for a 1 km mountain.

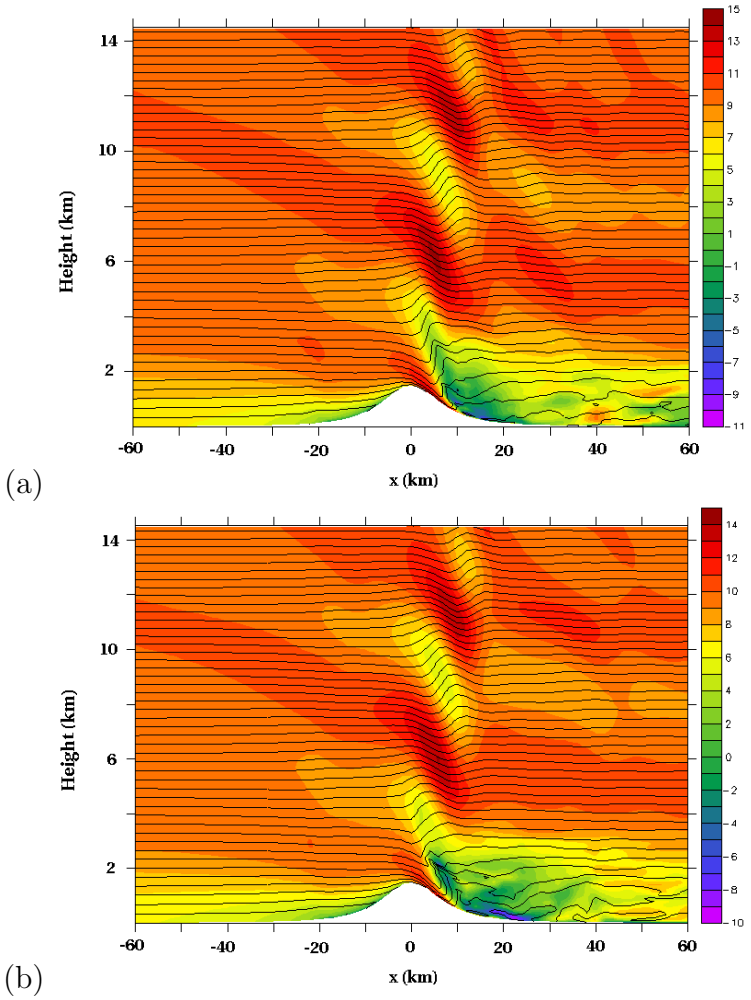

FIGURE 3.2: Flow structure for two successive model outputs in the no-shear simulation using a mountain height $H = 1.5$ km: 20th (a) and 21st (b) hours of simulation. The solid lines are isentropic surfaces (with a spacing of 1 K), the background contour field denotes the u velocity component (in $\mathrm{m\,s^{-1}}$).

However, for all the simulations performed, negative values of Ri were not observed, emphasizing that in the simple case of a constant background wind and stratification over an axisymmetric mountain wave breaking does not occur for $N_0 H/U \leq 1$. This is in agreement with linear theory (Smith, 1989), and is corroborated by the numerical simulations of Miranda and James (1992), which also indicate that beyond the narrow range of $N_0 H/U > 1$ for which wave breaking does occur, the vertically propagating waves weaken due to flow splitting. Therefore, the present results are consistent with both previous numerical simulations and linear theory, although the latter was formulated by Smith using the Boussinesq approximation, and using linear solutions to study an intrinsically non-linear phenomenon such as wave breaking is questionable.

Previous studies (Smolarkiewicz and Rotunno, 1989; Miranda and James, 1992; Bauer

et al., 2000) suggest that a 3D flow over an axisymmetric mountain enters a wave-breaking regime for $1 < N_0H/U < 2$. Thus, in order to induce wave breaking, additional simulations using mountain heights H of 1.25 km and 1.5 km (i.e. $N_0H/U =$ 1.25 and 1.5, respectively) were run. Figure 3.2 shows vertical cross sections (passing through the centre of the computational domain) of the potential temperature (black solid lines) and u velocity (filled contours) for the 20th (Figure 3.2(a)) and 21st (Figure 3.2(b)) hours of the simulation for H =1.5 km. In Figure 3.2(a) the steepness of isentropic surfaces (which coincide with streamlines) is critical, i.e. the streamlines are vertical at a height of about 2 km, just downstream of the mountain, and in Figure 3.2(b) the presence of overturned streamlines implies local static instability. In this situation, waves break, and subsequently the flow becomes statically stable again (not shown). Any turbulence generation thus tends to be intermittent. A similar flow configuration is found for the simulation performed using H =1.25 km, confirming that for $N_0H/U > 1$ wave breaking may be observed in unsheared flow, as originally found by Miranda and James (1992). The good agreement between our results and previous theoretical and numerical studies demonstrate that the numerical setup chosen for this study is appropriate.

3.3.2 Wind shear simulations

Adding a directional wind shear to the background flow reduces the stability of the flow by decreasing the value of Ri by an amount that, if large enough, can lead alone to generation of instabilities, and hence potentially to turbulence. In real flows, a background $\mathrm{Ri_{in}} \leq 0.25$ would allow spontaneous generation of turbulence that would mask the turbulence due to wave breaking. Because of that, and also because such low values of Ri are very rare in the real atmosphere, the smallest value of $\mathrm{Ri_{in}}$ considered here is 0.5, which is still above the critical threshold value of 0.25 for which dynamic instability is expected. The largest value of $\mathrm{Ri_{in}}$, on the other hand, was chosen so that the corresponding wind shear, even if weak, is still able to affect the waves appreciably.

When mountain waves are generated, the shear due to the waves is added to the shear of the background flow and the resulting Richardson number is lower (although N is also modified). Thus, in shear flows, mountain wave propagation triggers turbulence earlier than in no-shear flows (as will be seen in more detail next). However, due to the nonlinear response of the waves to the background flow and the effect of critical levels, these processes are far from being simply additive.

A complete overview of the numerical simulation results is provided by the regime diagram shown in Figure 3.3. The model outputs of the last 7 hours of the simulations were analysed, looking for $\mathrm{Ri}_{\mathrm{min}}$. In those simulations where wave breaking does not occur ($\mathrm{Ri}_{\mathrm{out}}$ always positive) the hourly values of $\mathrm{Ri}_{\mathrm{min}}$ are nearly constant and may vary, between an hour and the next, by only a few percent. When wave breaking is observed, in contrast, the $\mathrm{Ri}_{\mathrm{min}}$ values oscillate in time due to the intermittency of this process, but remain negative. In Figure 3.3, all the $\mathrm{Ri}_{\mathrm{min}}$ values refer to the last hour of simulation. The four categories used to build the regime diagram have been chosen in accordance with the background literature, from which it is known that the wave-turbulence interaction may begin with a dynamical instability, which leads to convective instability and then to turbulence (Nappo, 2012). The four categories are: $\mathrm{Ri}_{\mathrm{min}} < 0$ indicating convective instability due to wave breaking events, $0 < \mathrm{Ri}_{\mathrm{min}} \leq 0.25$ indicating dynamic instability (potentially an index of turbulence), $0.25 < \mathrm{Ri}_{\mathrm{min}} \leq 1$ indicating a flow having kinetic energy available for turbulent mixing, and $\mathrm{Ri}_{\mathrm{min}} > 1$ indicating non-turbulent flow where no wave breaking events occur.

Whilst it is straightforward to assign a meaning to those $\mathrm{Ri}_{\mathrm{min}}$ values that are negative or large and positive, it is less obvious how to interpret the values of Ri that are small but still positive. As is well known, a Richardson number lower than 0.25 is a necessary but not sufficient condition for dynamical instability (Miles, 1961). However, Hanazaki and Hunt (2004) argued that the critical value for the stability of the flow above which turbulence cannot be sustained is $\mathrm{Ri}_{\mathrm{min}} \sim 0.3$. Hence, the choice of a critical Richardson number for turbulence generation is controversial, and the effective threshold value of Ri can be somewhat larger than 0.25. In fact, in atmospheric flows where the background velocity vector varies with height the energy condition for the instability threshold is less stringent than $\mathrm{Ri} < 0.25$ (Hines, 1971; Turner, 1973). Further, in case of finite perturbations (as the ones generated by finite amplitude gravity waves) Businger (1969) demonstrated that when $\mathrm{Ri} < 1$ there will be a net release of kinetic energy in the flow. This energy may be used by the flow to initiate turbulent mixing. As mentioned before, in the simulations presented here, no turbulent mixing is allowed. Therefore, categories 2 (triangles, $0 < \mathrm{Ri}_{\mathrm{min}} \leq 0.25$) and 3 (diamonds, $0.25 < \mathrm{Ri}_{\mathrm{min}} \leq 1$) in the regime diagram have been chosen to highlight the flows that, potentially, can evolve into turbulence.

It is also worth mentioning that flows in the regime diagram having $\mathrm{Ri} < 0.25$ can be relevant for the problem of mountain wave reflection and resonant drag enhancement. Indeed, when waves propagate from layers with larger Ri to layers with $\mathrm{Ri} \leq 0.25$, in the presence of critical levels, linear theory shows that the wave solution changes its

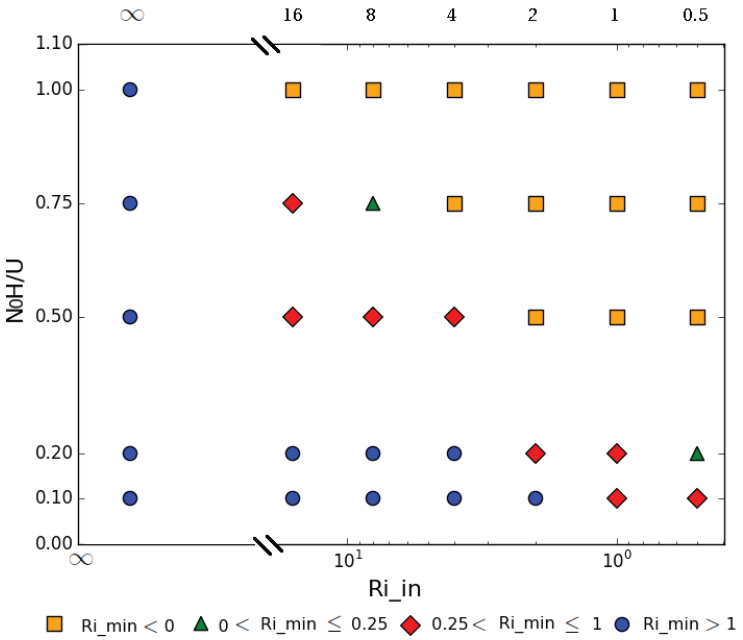

FIGURE 3.3: Regime diagram describing the nature of the flow using four categories based on the $\mathrm{Ri}_{\mathrm{min}}$ values. In the lower horizontal axis a logarithmic scale is used for $\mathrm{Ri}_{\mathrm{in}}$, however for increased readability the actual $\mathrm{Ri}_{\mathrm{in}}$ values considered are shown on the upper horizontal axis.

nature and perfect wave reflection or over-reflection may occur (Lindzen and Tung, 1976). If the reflected downward-travelling waves interfere constructively with the incoming upward-travelling waves, the wave amplitude, and hence the drag, may be amplified by a large factor (Lin, 2007).

Analysing the regime diagram in Figure 3.3, we can see that whereas in the no-shear case ($\mathrm{Ri}_{\mathrm{in}} = \infty$) wave breaking does not occur ($\mathrm{Ri}_{\mathrm{min}} > 1$ always), in the shear flows considered here wave breaking is always found for a non-dimensional mountain height $N_0H/U = 1$, no matter what $\mathrm{Ri}_{\mathrm{in}}$ is used. For $N_0H/U = 0.75$ wave breaking is detected when $\mathrm{Ri}_{\mathrm{in}} \leq 4$, but a very small value of Ri lower than 0.25 occurs already for $\mathrm{Ri}_{\mathrm{in}}$ =8. For $N_0H/U = 0.50$ wave breaking is present when $\mathrm{Ri}_{\mathrm{in}} \leq 2$, although $\mathrm{Ri}_{\mathrm{min}}$ is never larger than 1 for any wind shear intensity considered. It is only when assuming very small mountain heights ($N_0H/U = 0.1$ and $N_0H/U = 0.2$) that wave breaking is absent. However, when using a strong background wind shear (low $\mathrm{Ri}_{\mathrm{in}}$), the $\mathrm{Ri}_{\mathrm{min}}$ values obtained are small (lower than 1 or 0.25). This is, of course, consistent with the fact that we always have $\mathrm{Ri}_{\mathrm{min}} < \mathrm{Ri}_{\mathrm{in}}$.

The regime diagram therefore shows that either considering a fixed wind shear intensity of the background flow and increasing the mountain height or using a fixed N_0H/U and increasing the wind shear intensity makes the flow more likely to overturn, ultimately leading to wave breaking. By selecting flow overturning ($\mathrm{Ri}_{\mathrm{min}} < 0$) as a discriminating factor, it is possible to split the regime diagram in two sub-regions

representing a non-wave-breaking flow regime and a wave-breaking regime. Regimes where the flow behaviour is less clear-cut are accounted for by the relatively narrow regions with $0 < \mathrm{Ri}_{\mathrm{min}} \leq 0.25$ or $0.25 < \mathrm{Ri}_{\mathrm{min}} \leq 1$.

It should be noticed that if the vertical axis in Figure 3.3 was extended up to higher values of N_0H/U the wave breaking regime would continue, including now also the no-shear case (results not shown), as discussed in the previous section. This was confirmed in a few examples, but simulations using mountain heights of 1.25 km and 1.5 km and finite $\mathrm{Ri}_{\mathrm{in}}$ were not carried out systematically because it is clear beforehand that they would also produce wave breaking. Even larger mountain heights ($N_0H/U > 1.5$) were not considered because the flow would then enter a flow-splitting regime (Lin, 2007) where wave generation aloft would be strongly attenuated or totally suppressed (Miranda and James, 1992).

3.3.2.1 Non-wave breaking regime

In the absence of wave breaking, mountain waves are almost perfectly steady and the perturbation pattern associated with their propagation is stationary in time. Therefore, for those flows falling into the non-wave breaking regime in Figure 3.3, $\mathrm{Ri}_{\mathrm{min}}$ occurs at the points where the flow gets closest to instability. The stationary character of the solution enables one to analyse how it varies as function of the input conditions. Figure 3.4 shows how the $\mathrm{Ri}_{\mathrm{min}}$ values vary as a function of $\mathrm{Ri}_{\mathrm{in}}$ for a same N_0H/U value in the flows with shear. The one-to-one line represents the response that the flow would have in a perfectly linear regime, where waves are generated by an infinitesimal mountain and their perturbation of the background flow is itself infinitesimal ($\mathrm{Ri}_{\mathrm{out}} = \mathrm{Ri}_{\mathrm{in}}$). As we start to consider finite mountain heights, the simulation results show that an increase in N_0H/U corresponds to a decrease of $\mathrm{Ri}_{\mathrm{min}}$ in flows with the same background wind shear (i.e. same $\mathrm{Ri}_{\mathrm{in}}$). A base-2 logarithmic scale is used on both the horizontal and vertical axes to highlight the values of $\mathrm{Ri}_{\mathrm{in}}$ used, and also the fact that, when $N_0H/U = 0.1$, the variation of $\mathrm{Ri}_{\mathrm{min}}$ with $\mathrm{Ri}_{\mathrm{in}}$ suggests the existence of a power law behaviour (more exactly a linear relationship). However, the $N_0H/U = 0.1$ curve is the only one that behaves in this way. For higher values of N_0H/U, the relationship between $\mathrm{Ri}_{\mathrm{min}}$ and $\mathrm{Ri}_{\mathrm{in}}$ is more complicated and the small number of data points in the cases $NH/U = 0.5$ and $NH/U = 0.75$ does not allow many conclusions to be drawn about this relationship. This small number of points is due to the fact that, in these cases, the majority of the points corresponds to wave breaking situations. A final comment on the non-wave breaking regime concerns the flow category 2 (represented by triangles) that seems to

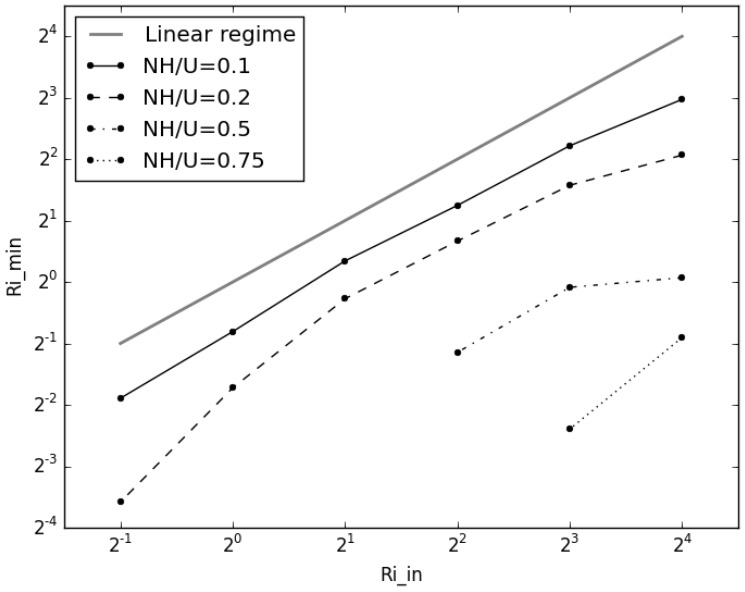

FIGURE 3.4: $\mathrm{Ri}_{\mathrm{min}}$ for flows in the non-wave breaking regime (according to Figure 3.3) versus $\mathrm{Ri}_{\mathrm{in}}$ for different N_0H/U values. On both the horizontal and vertical axes a base-2 logarithmic scale is used.

be under-represented in the regime diagram of Figure 3.3. Only two of the considered background flow conditions ($N_0H/U = 0.75$ with $\mathrm{Ri}_{\mathrm{in}} = 8$, and $N_0H/U = 0.2$ with $\mathrm{Ri}_{\mathrm{in}} = 0.5$) lead the flow to have a quasi-stationary configuration with $0 < \mathrm{Ri} < 0.25$. This is partly explained by the fact that the values of N_0H/U and $\mathrm{Ri}_{\mathrm{in}}$ have a relatively sparse sampling in the regime diagram. Taking into account more $\mathrm{Ri}_{\mathrm{in}}$ values in the interval $[0.5, 16]$ would probably increase the number of points falling into this category. Nonetheless, this region in the flow regime is necessarily narrow. This is consistent with a previous study by Laprise and Peltier (1989), where it was shown (for a case without shear) that when the flow transitions from a situation without wave breaking to a situation with flow overturning, the Richardson number changes from being positive and larger than 0.5 to (suddenly) becoming large and negative, without taking (steady) values in the interval $[0, 0.5]$ (see their Figure 10). Therefore, a steady state mountain wave field having $0 < \mathrm{Ri} < 0.25$ may be difficult to attain, perhaps because of the onset of dynamical instability.

3.3.2.2 Wave breaking regime

The mechanism leading to wave breaking in shear flows is fundamentally different from the one acting in the no-shear case where the amplitude of the mountain is the sole responsible for the fulfilment of the flow overturning condition. For a no-shear flow no environmental critical levels exist, but a self-induced critical level is created where the background flow velocity $\mathbf{U}$ plus the wave velocity perturbation (u', v') add

up to zero, leading to vertical streamlines (Clark and Peltier, 1984). For directional shear flows, environmental critical levels are defined as the heights where the horizontal wave number vector $\boldsymbol{\kappa}_H \equiv (k, l, 0)$ is perpendicular to the background wind vector $\mathbf{U} \equiv (u_0, v_0, 0)$. When this happens ($\mathbf{U} \cdot \boldsymbol{\kappa}_H = 0$), the vertical wave number m defined in linear theory (adopting a zeroth-order Wentzel-Kramers-Brillouin (WKB) approximation) as $m = \frac{N_0(k^2+l^2)^{1/2}}{u_0 k + v_0 l}$ approaches infinity and the vertical wavelength $\lambda_z = 2\pi/m$ zero. As a wave packet approaches a critical level it experiences a fast oscillation ($m \to \infty$) for which the vertical velocity becomes small compared to the horizontal velocity perturbation (that actually diverges to infinity) (Shutts, 1998). In these conditions the amplitude of the disturbance increases and the waves break.

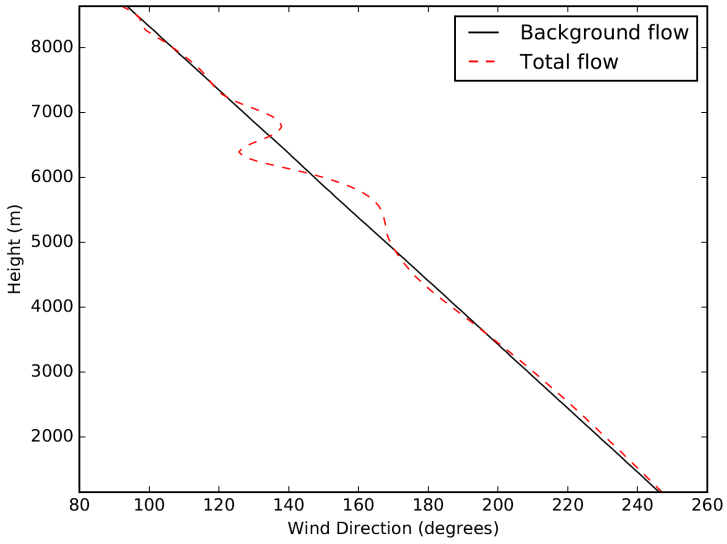

FIGURE 3.5: Variation of the wind direction with height for the simulation with N_0H/U=1 and $\mathrm{Ri}_{\mathrm{in}}$=8. The profile includes the point where the minimum Richardson number occurs (according to Table 3.2).

Figure 3.5 helps to visualize what happens when a wave packet approaches a critical level. It explains the reason why the $\mathrm{Ri}_{\mathrm{min}}$ found for $N_0H/U = 1$ and $\mathrm{Ri}_{\mathrm{in}} = 8$ (see Table 3.2) is so markedly negative. Although a wave packet comprises a range of wave-numbers, that have a range of critical levels, the most active (and therefore most easily discernible) critical levels affect the wave-numbers that dominate the wave energy spectrum. The plot shows the variation of the wind direction (in degrees) with height. When the wave packet is approaching the dominant critical level, the wave amplitude increases and the background flow (solid line) is strongly modified by the wave perturbation (see dashed line). At $\sim$ 6391 m, the Richardson number approaches a highly negative value ($\mathrm{Ri}_{\mathrm{min}}$ = -1523.17) (see Table 3.2) because the wind shear is made locally zero by the wave perturbation. The negative sign, on the other hand,

is due to flow overturning (i.e. $N^2 < 0$). Clearly, this value is as indicative of static instability as any other negative value, since only $\mathrm{Ri}_{\mathrm{min}} < 0$ matters for that purpose.

The aim of this work is not only to diagnose wave breaking occurrence for given background flow conditions, but also to identify regions within the simulation domain where wave breaking and the potential development of turbulence are expected. The sketch in Figure 3.1(b) shows the area where the $\mathrm{Ri}_{\mathrm{min}}$ values occur for the simulations with $\mathrm{Ri}_{\mathrm{in}} = 8$ (based on Table 3.2); the arrow is the wind direction at the level where wave breaking occurs for the 1 km mountain case. Wave breaking is observed at a height of about 6.4 km where the wind is from the south-east which implies, from the definition of critical levels in directional shear flows, that the direction of the dominant wave-number vectors at that level is north-east (or south-west). The $\mathrm{Ri}_{\mathrm{min}}$ values are found near the edge of the square 'region of interest', due to the presence of the asymptotic wake described in Section 3.2.2.

The location and values of $\mathrm{Ri}_{\mathrm{min}}$ (such as given in Tables 3.1 and 3.2) allow us to delimit regions in the vicinity of the mountain where more detailed attention should be focused. $\mathrm{Ri}_{\mathrm{min}}$ by itself is a poor indicator of what is going on within the simulation domain: wave breaking may be occurring simultaneously in different regions. Additionally, the temporal and spatial evolution of the flow after a wave breaking event is of particular interest. Figure 3.6 shows 3D plots where all the grid points for which $\mathrm{Ri}_{\mathrm{out}} < 0.25$ are shown. The plots pertain to wind shear simulations run using a mountain height of 1 km where, according to the regime diagram in Figure 3.3, wave breaking always occurs. These plots can be seen as instantaneous snapshots of the flow at the 18th hour of simulation. The different background wind profiles for each $\mathrm{Ri}_{\mathrm{in}}$ considered are also shown.

In order to interpret the $\mathrm{Ri}_{\mathrm{out}} < 0.25$ fields displayed in Figure 3.6 in more detail, the temporal variability of Ri in a wave breaking event was analysed. For this purpose, an additional simulation using $\mathrm{Ri}_{\mathrm{in}} = 0.5$ and a higher model output rate (i.e., 6 model outputs per hour instead of 1) was carried out. Figure 3.7 shows a time-series of Ri in the 6 grid-points adjacent to the one where $\mathrm{Ri}_{\mathrm{min}}$ is located at the 18th hour of the simulation, which has horizontal coordinates $X = 22$ km, $Y = -10$ km and an altitude $z \approx 3.1$ km. The time-series begins at the 7th hour of simulation (the first 6 hours have been excluded because they correspond to the model spin-up time), and data are plotted every 10 minutes.

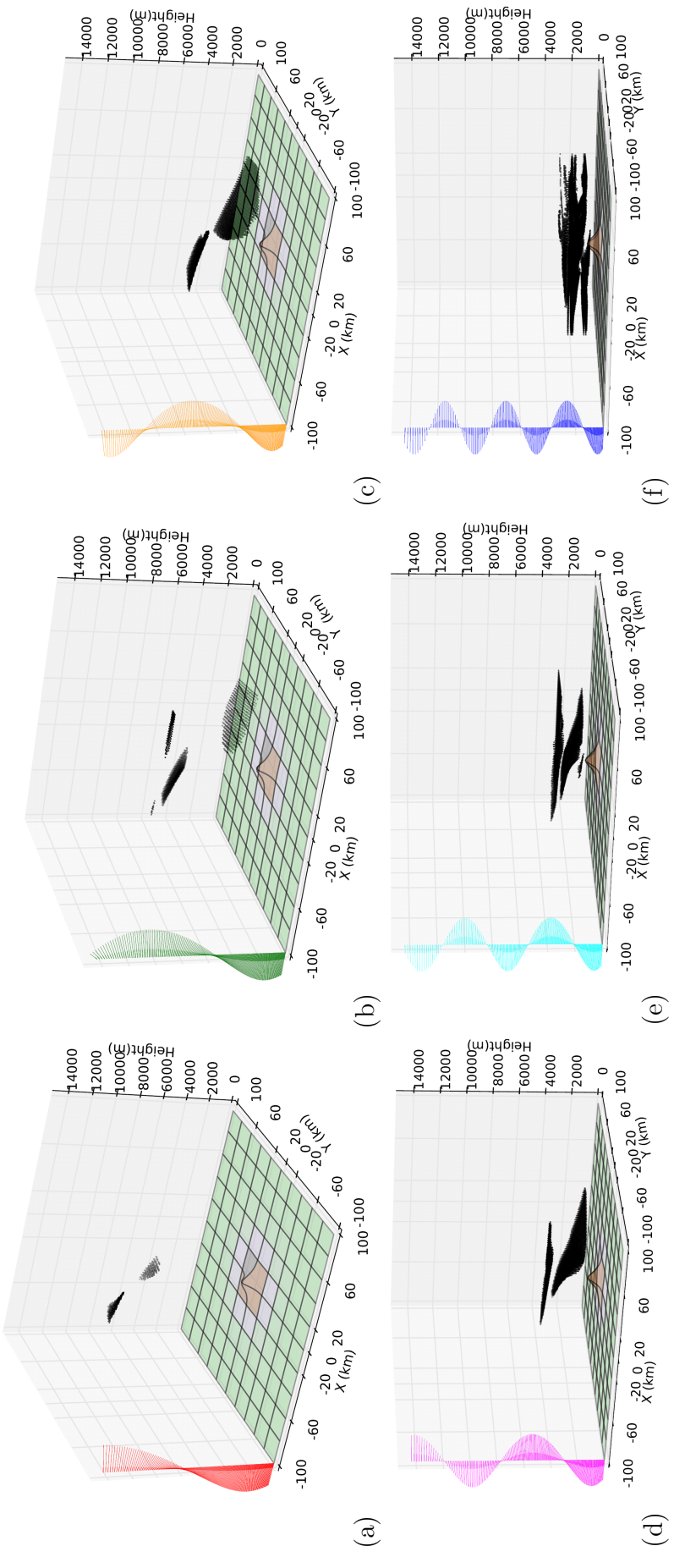

FIGURE 3.6: 3D plots showing every point in the computational domain where $\mathrm{Ri}_{\mathrm{out}} < 0.25$. The plots refer to the 18th hour of simulations and assume a $N_0 H/U = 1$ and different wind shear intensities: $\mathrm{Ri}_{\mathrm{in}}$ =16 (a), $\mathrm{Ri}_{\mathrm{in}} = 8$ (b), $\mathrm{Ri}_{\mathrm{in}}$=4 (c), $\mathrm{Ri}_{\mathrm{in}} = 2$ (d), $\mathrm{Ri}_{\mathrm{in}} = 1$ (e), $\mathrm{Ri}_{\mathrm{in}} = 0.5$ (f). The profile of vectors on the left-hand side of each plot shows the direction of the background wind as a function of height. The helical shape of the wind profile corresponds to a wind that rotates anticlockwise as z increases. At the ground the wind is always westerly, in accordance with (3.3).

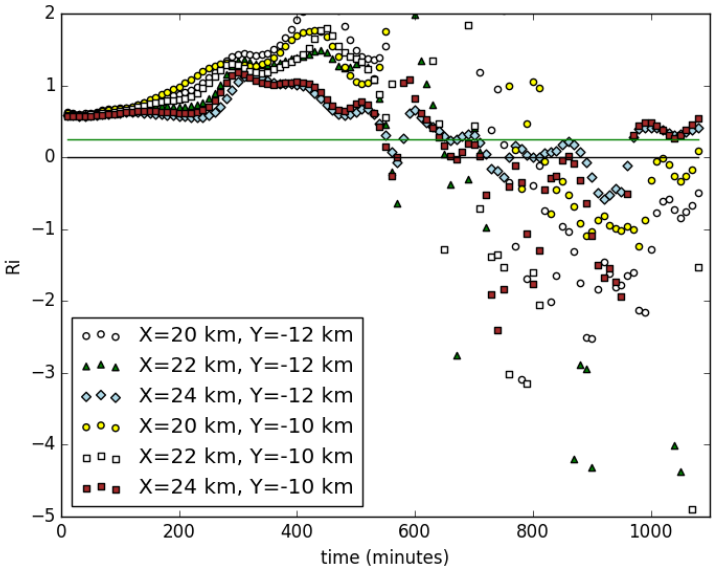

FIGURE 3.7: Time-series of the Richardson number evaluated at six grid-points adjacent to the one where, according to the $\mathrm{Ri}_{\mathrm{out}}$ field, wave breaking occurs in the simulation with $N_0 H/U = 1$ and $\mathrm{Ri}_{\mathrm{in}} = 0.5$. The coordinates X, Y or each point are shown. For all the considered points $z \approx 3100$ m.

The purpose of Figure 3.7 is to point out that for each grid-point, after the first wave breaking event has taken place (the first time Ri drops below 0), Ri keeps oscillating between negative and positive values. Additionally, Ri remains roughly between 0 and 0.25 both before and after wave breaking periods. The shaded regions in the 3D plots of Figure 3.6 therefore presumably represent locations where waves are at different stages of their intermittent breaking process, including waves which are breaking ($\mathrm{Ri} < 0$), about to break, or have already broken ($0 < \mathrm{Ri} < 0.25$). When mountain waves break the associated convective instability can lead to turbulence generation (known as Clear Air Turbulence or CAT), thus the plots in Figure 3.6 can been thought of as continuous regions of (potential) occurrence of mountain wave-induced CAT. The extent of these regions is variable, increasing with the background shear intensity. While for simulations using $\mathrm{Ri}_{\mathrm{in}} = 16$ localized shading is visible occupying a very small fraction of the 'region of interest', the flow topology for $\mathrm{Ri}_{\mathrm{in}} = 0.5$ is much more complex. This happens because when the shear due to waves is added to an already strong background wind shear, Ri values lower than 0.25 occur simultaneously in many vertical levels and almost everywhere across the horizontal plane. An important aspect is that, for stronger background shear, $\mathrm{Ri} < 0.25$ regions, and the $\mathrm{Ri}_{\mathrm{min}}$ values embedded in them, occur at lower levels. This means that, the stronger the directional shear is, the faster (or, more exactly, the lower down) the wave energy is dissipated, preventing wave breaking at higher levels. This is due to the

greater density of critical levels, which leads to more concentrated wave amplification, breaking, and subsequent dissipation, as will be detailed below.

The definition of critical level ($\mathbf{U} \cdot \boldsymbol{\kappa}_H = 0$) implies that, in directional shear flows where the wind turns with height continuously, all levels are critical levels. Unlike mountain waves generated by a sinusoidal terrain corrugation, orographic gravity waves excited by an isolated mountain do not have a single forcing wave-number, but rather a full spectrum of waves, with a range of wave-numbers pointing in all directions (Nappo, 2012). When the wind turns with height there will always be a wave-number vector perpendicular to the wind direction at that level. However, in a wave breaking event we can assume that only the most energetic wave-numbers (associated with the largest wave amplitudes) are able to dominate the behaviour of the entire wave packet and cause wave breaking. The other less energetic wave-numbers can still change the background flow but they will not contribute as importantly to wave breaking (as shown by Figure 3.5). Therefore, perhaps every point where wave breaking is detected within the computational domain can be seen as a point where the background wind velocity vector is perpendicular to a dominant horizontal wave-number vector.

Because of the helical wind profile employed in the simulations, in weaker shear flows (such as that with $\mathrm{Ri_{in}} = 16$) the wind vector and the (most energetic) horizontal wave-number vectors attain perpendicularity at higher levels, making wave breaking take place at high altitudes. In stronger shear flows (such as those with $\mathrm{Ri_{in}} = 1$ or 0.5), the same wind angle occurs at lower levels. Thus, fulfilment of the condition $\mathbf{U} \cdot \boldsymbol{\kappa}_H = 0$ is more probable for a major part of the wave spectrum in the lower atmosphere. For example, using $\mathrm{Ri_{in}} = 16$ the wind changes from westerly at the ground to easterly at the bottom of the sponge layer (14 km). Considering a stronger wind shear, for example $\mathrm{Ri_{in}} = 1$, the same change in wind direction occurs over the lowest 3 km of the atmosphere. Since the wave energy is likely to be dissipated by wave breaking at the lowest critical levels the waves encounter (for low Ri, there may be multiple critical levels, as pointed out by Teixeira and Yu (2014)), at greater altitudes nearly all the wave energy has already been dissipated.

To conclude, we emphasize that the flow topology displayed in Figure 3.6 was found to be relatively insensitive to changes in both vertical and horizontal resolutions. Sensitivity tests using a horizontal resolution of 1 km instead of 2 km, and 400 model vertical levels instead of 200, were carried out for $\mathrm{Ri_{in}} = 16$ and 1 (weak and strong shear, respectively). In these simulations, the $\mathrm{Ri_{out}} < 0.25$ field, which characterizes regions of potential flow instability (not shown), had mostly the same distribution as in Figure 3.6, being only marginally affected by changes in resolution. These sensitivity tests corroborated that the resolution adopted in the present study seems

appropriate to represent the major physical processes taking place in the simulation domain.

3.3.3 A possible wave breaking diagnostic

Although there is no immediate way to evaluate the dominant wave-number vectors in the mountain wave field (a spectrum would have to be computed), a joint qualitative analysis of the flow structure and of the background wind profile for the cases shown in Figure 3.6 suggests that these wave-number vectors (k,l) are roughly aligned with the corresponding horizontal velocity perturbation vectors (u',v'). Since the dominant wave-number vector and the background wind vector (u_0, v_0) are approximately perpendicular at each height (due to critical levels), this is equivalent to (u_0, v_0) and (u', v') also being perpendicular. This behaviour was detected both in weak and in strong shear flows.

In Figure 3.8(a) and 3.8(c) two horizontal cross-sections of the wind field for the simulations with $\mathrm{Ri_{in}} = 16$ and $\mathrm{Ri_{in}} = 1$ at the 18th hour of simulation are shown. The cross-sections are taken at the model levels where, according to the analysis carried out in Figure 3.6, wave breaking ($\mathrm{Ri_{out}} < 0$) occurs. The regions where $\mathrm{Ri_{out}} \leqslant 0.25$ are shown by $\mathrm{Ri_{out}}$ contour lines. The magnitude of the velocity perturbation vector (u',v') is shown by the background contours. The black vectors are the background wind and the red thick vectors are the wave velocity perturbation (calculated by subtracting the background wind from the total flow).

In Figure 3.8(a) the branch of maximum horizontal velocity perturbation elongated to the north-west, where the background wind vector and the velocity perturbation vectors become nearly perpendicular, coincides partially with the shape of the lowest shaded region displayed in Figure 3.6(a) (corresponding to the $\mathrm{Ri_{out}}$ contours in the cross-section). In fact, both shaded regions in Figure 3.6(a) extend vertically, therefore corresponding to several model levels. The map in Figure 3.8(a) (at $z \approx 7$ km) contains only some of the points belonging to the lowest region. Except for the aforementioned elongated region, it is clear that elsewhere in the computational domain the wave velocity perturbation is very small and does not modify the background flow appreciably (whose vectors then coincide with those of the total flow). The same behaviour is observed for the strong wind shear case (Figure 3.8(c)), where departing from the middle of the computational domain towards the north-west, a region where the wave velocity perturbation becomes large and almost perpendicular to the background wind is visible. This region coincides with part of the lower boundary of

the main shaded region displayed in Figure 3.6(e), at a height of about 2 km.

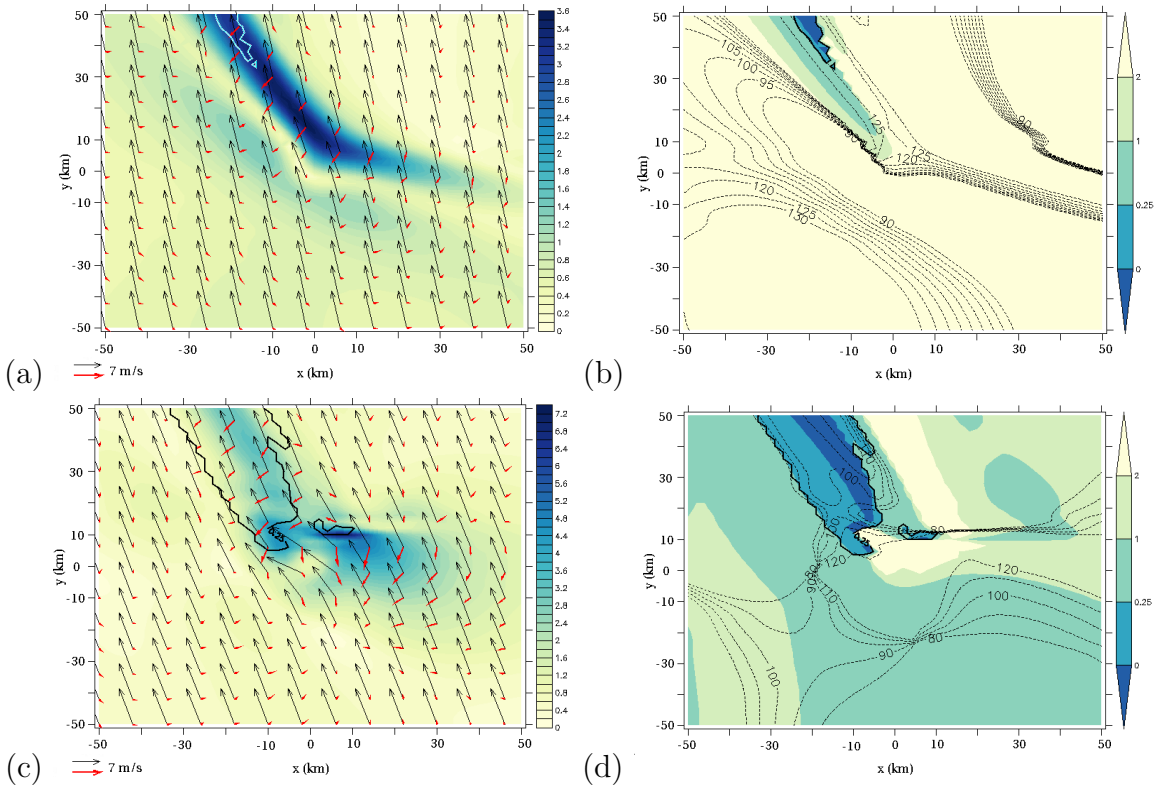

FIGURE 3.8: Horizontal cross-sections of the wind field, (a) and (c), and $\mathrm{Ri_{out}}$, (b) and (d), for the simulations with $\mathrm{Ri_{in}} = 16$ ((a) and (b)), $\mathrm{Ri_{in}} = 1$ ((c) and (d)) at the 18th hour of simulation. The cross-sections are taken at an altitude of about 7 km ((a) and (b)) and 2 km ((c) and (d)). In (a) and (c), on the background, the magnitude of the velocity perturbation vector (u',v') (in $\mathrm{m\,s^{-1}}$) is shown. The thick contour lines (white in (a), black in (c)) denote $\mathrm{Ri_{out}} = 0.25$. The black vectors are the background wind and the red thick vectors are the velocity perturbation. In (b) and (d), on the background, the $\mathrm{Ri_{out}}$ field is shown. All the $\mathrm{Ri_{out}}$ values higher than 2 and lower than 0 are represented by the same color. The dashed contour lines represent the angle between the background wind vector and the velocity perturbation vector. The thick contour lines again correspond to $\mathrm{Ri_{out}} = 0.25$.

Both in Figure 3.8(a) and 3.8(c), other locations where (u_0, v_0) and (u',v') are almost perpendicular and the wave perturbation is large can be detected. These locations lie outside the $\mathrm{Ri_{out}} = 0.25$ contour, but still within the elongated region in Figure 3.8(a) corresponding to the maximum velocity perturbation, and at the south-east edge of the computational domain in Figure 3.8(c). Since at these locations $\mathrm{Ri_{out}}$ is higher than 0.25 but still small, as shown in Figure 3.8(b) and 3.8(d), this may mean

that while being able to perturb the background flow, the wave amplitude is not large enough to induce dynamic instability.
The effective angle that the velocity perturbation vectors form with the background wind vector is shown in Figure 3.8(b) and 3.8(d). The dashed contour lines are a selected range of contour levels with values around 90 degrees, and in the background the $\mathrm{Ri}_{\mathrm{out}}$ field is shown. As observed in Figure 3.8(a) and 3.8(c), where the velocity perturbation is large and $\mathrm{Ri} \leqslant 0.25$ the angle between the two vectors tends to be a right angle, but it can vary between 80 and 130 degrees. Other areas within the computational domain where the two vectors make an angle roughly between 80 and 130 degrees can be detected, but in these areas the wave perturbation is small, hence it would be questionable to attach any significance to them.

These preliminary findings, based on a simple visual inspection of the Ri and wind velocity vector fields, contribute to improve our understanding of the flow structure displayed in Figure 3.6. They suggest a link between the orientation of the velocity perturbation vector and the background wind vector in high-amplitude wave regions, which is confirmed by a mathematical argument based on linear theory, presented next.

For hydrostatic, adiabatic, 3D, frictionless flow without rotation, the Taylor-Goldstein equation, which governs the behaviour of mountain waves, takes the form (Nappo, 2012):

$$\frac{d^2\widehat{w}}{dz^2} + \left[\frac{(k^2+l^2)N^2}{(ku_0+lv_0)^2} - \frac{ku_0''+lv_0''}{ku_0+lv_0}\right]\widehat{w} = 0, \tag{3.4}$$

where $\widehat{w}$ is the Fourier transform of the vertical velocity, and the primes denote differentiation with respect to z.
The Fourier transforms of the horizontal velocity perturbations are given by (Nappo, 2012):

$$\widehat{u'}(k,l,z) = \frac{ik}{k^2+l^2}\left[\frac{l\widehat{w}(lu_0'-kv_0')}{k(ku_0+lv_0)} + \frac{\mathrm{d}\widehat{w}}{\mathrm{d}z}\right], \tag{3.5}$$

$$\widehat{v'}(k,l,z) = \frac{-il}{k^2+l^2}\left[\frac{k\widehat{w}(lu_0'-kv_0')}{l(ku_0+lv_0)} - \frac{\mathrm{d}\widehat{w}}{\mathrm{d}z}\right]. \tag{3.6}$$

Note that the second terms within the square brackets in (3.5)-(3.6) correspond to a vector that is parallel to the horizontal wave-number vector (k,l), whereas the first terms correspond to a vector that is perpendicular to (k,l). In shear flows, the solution to (3.4) may be expressed as:

$$\widehat{w} = \widehat{w}(z=0)\mathrm{e}^{\,i\int_0^z m(z)\mathrm{d}z}. \tag{3.7}$$

Substituting (3.7) into (3.5)-(3.6) and adopting a zeroth-order WKB approximation, (3.5) and (3.6) become:

$$\widehat{u'}(k,l,z) = \frac{ik\widehat{w}}{k^2+l^2}\left[\frac{l(lu_0' - kv_0')}{k(ku_0+lv_0)} - i\frac{N_0(k^2+l^2)^{1/2}}{ku_0+lv_0}\right], \tag{3.8}$$

$$\widehat{v'}(k,l,z) = \frac{-il\widehat{w}}{k^2+l^2}\left[\frac{k(lu_0' - kv_0')}{l(ku_0+lv_0)} + i\frac{N_0(k^2+l^2)^{1/2}}{ku_0+lv_0}\right], \tag{3.9}$$

where $m = N_0(k^2+l^2)^{1/2}/(ku_0+lv_0)$ is the same expression for m as in the constant wind case, but where u_0 and v_0 vary with height because of directional shear. The WKB approximation assumes that the background flow changes slowly with z compared to the vertical wavelength of the waves. A slowly varying medium implies a slowly varying vertical wave-number, which allows us to approximate m as described above. Contrary to what one may expect, the WKB approximation is still valid in flows with a fairly low Richardson number, as shown by Teixeira *et al.* (2004) and Teixeira and Miranda (2009).

At a critical level $ku_0 + lv_0 = 0$, which suggests that both the terms within the brackets in (3.8)-(3.9) would diverge to infinity. However, the helical wind profile described by (3.3) implies that

$$u_0' = -U\sin(\beta z)\beta = -\beta v_0\ , \qquad v_0' = U\cos(\beta z)\beta = \beta u_0, \tag{3.10}$$

and substituting $lu_0' - kv_0' = -\beta(ku_0 + lv_0)$ into the numerators of the first terms on the right-hand side of (3.8) and (3.9), the equations for $\widehat{u}$ and $\widehat{v}$ become:

$$\widehat{u'}(k,l,z) = \frac{-il\beta\widehat{w}}{k^2+l^2} + \frac{k\widehat{w}}{k^2+l^2}\frac{N_0(k^2+l^2)^{1/2}}{ku_0+lv_0}, \tag{3.11}$$

$$\widehat{v'}(k,l,z) = \frac{ik\beta\widehat{w}}{k^2+l^2} + \frac{l\widehat{w}}{k^2+l^2}\frac{N_0(k^2+l^2)^{1/2}}{ku_0+lv_0}. \tag{3.12}$$

This shows that at critical levels ($ku_0 + lv_0 = 0$) the second terms on the right-hand side are the only ones that diverge to infinity, and therefore are overwhelmingly dominant. Under these conditions, the $(\widehat{u'}, \widehat{v'})$ vector is parallel to the wave-number vector $(k,\ l)$. Although $\widehat{u'}$ and $\widehat{v'}$ are the Fourier transforms of the physical u' and v' perturbation velocities, and thus contribute to u' and v' from a range of wave-numbers, their contribution is dominant at critical levels, where $(k,l)\cdot(u_0,\ v_0) = 0$, because of this divergent behaviour. Hence the condition that $(\widehat{u'}\ ,\ \widehat{v'})$ and (k,l) are parallel at critical levels can be translated in physical space into a condition stating that $(u',\ v')$ and $(u_0,\ v_0)$ are approximately perpendicular, which explains what can be seen in Figure 3.8.

Note that considering a series expansion of the vertical wave-number up to second- or third-order in the WKB approximation in (3.7), as done by Teixeira *et al.* (2004) and Teixeira and Miranda (2009), would not add much to the present analysis or affect the conclusions inferred therefrom. This power series can be expressed as the leading zeroth-order term multiplyed by 1 plus higher-order corrections that have no singularities. Hence the singular behaviour of the whole series at critical levels can be inferred correctly using only the zeroth-order term. Furthermore, inclusion of non-hydrostatic effects in the WKB solution is not physically justified, since mountain waves are perfectly hydrostatic at critical levels, as noted by Grubišić and Smolarkiewicz (1997).

3.4 Summary and conclusions

In this chapter orographic gravity wave breaking in flows with directional wind shear has been investigated. A set of numerical simulations were performed to study wave breaking using orography and wind profiles with a common idealized form, but varying terrain elevations and shear intensities, respectively. The numerical simulation results were summarized in a regime diagram classifying the flow behaviour. In no-shear flows, wave breaking was observed only for dimensionless mountain heights $N_0H/U > 1$, as found by previous authors.

In directional shear flows, for the values of $\mathrm{Ri_{in}}$ considered here, wave breaking always occurs when $N_0H/U = 1$. However, for gradually stronger directional shears (lower $\mathrm{Ri_{in}}$) the critical N_0H/U for wave breaking decreases down to 0.5. Therefore, in presence of directional shear, wave breaking can occur over lower mountains than in the constant-wind case, a result that is not wholly unexpected.

When mountain waves break, the associated convective instability can lead to turbulence generation (which is one of the existing forms of CAT). In this study, the flow topology during wave breaking events was studied in order to identify regions within the computational domain where potential CAT generation is expectable. These regions correspond to all the points in the 'region of interest' embedded in the computational domain where the Richardson number of the output flow $\mathrm{Ri_{out}}$ is lower than 0.25. As the analysis of the temporal variability of Ri revealed, these dynamical instability regions can represent waves at different stages of their intermittent breaking process, namely: waves which are breaking, about to break, or that have already broken. The flow topology inferred from the present study can be summarized as follows:

- in contrast with no-shear flows where wave breaking occurs essentially over the mountain, for the helical wind profiles with directional shear adopted in this study, the flow overturning regions are more three-dimensional and spread along the 3 spatial directions;

- increasing the strength of the directional shear (i.e., reducing the value of $\mathrm{Ri}_{\mathrm{in}}$) leads to more numerous wave breaking events and to wider regions of (potential) turbulence generation;

- for stronger shear flows, wave breaking occurs at lower levels, and all the wave energy is dissipated within the first few kms above the ground because of the fast rate of turning of the background wind with height. However, this does not imply that a stronger directional shear produces less dangerous CAT. Indeed, in real atmospheric conditions the wind can begin to turn with height at any altitude. By changing the altitude at which the wind starts to turn, we can reasonably expect that the region of instability found near the ground in the simulations presented here will be translated upwards accordingly. However, the situation is complicated by the fact that an additional physical parameter is added to the problem: the height where the wind begins to turn. This is a possible topic for future study.

The velocity field in a wave breaking event has also been analysed. By examining the dynamics of the horizontal velocity perturbations associated with the waves in Fourier space, it was found that the Fourier transform of the horizontal velocity perturbation vector and the wave-number vector are aligned at critical levels. When transposed to physical space, this explains the approximate perpendicularity between the wave velocity perturbation vector and the background wind vector detected in the flow cross-sections. However, it was observed that the angle between the two vectors ranges from 80 to 130 degrees. A reason for this behaviour may be that at a critical level wave-numbers other than the dominant one can still play a role in determining the orientation of the velocity perturbation vector, especially if the energy of the waves at the wave-number meeting a critical level is especially low. This approximate perpendicularity could in principle be used as a diagnostic for CAT forecast in directional shear flows. Indeed, looking at the orientation of the (u', v') vector is much easier than detecting where the most energetic wave components have critical levels, which entails the calculation of spectra.

Although the validity of this diagnostic is supported by a theoretical argument, its generality and applicability to real flows must be tested. Concerning the generality of the result, although the physical interpretation presented in Section 3.3.3 relies

crucially on the form of the helical wind profile (3.3), we can expect it to hold approximately for any wind profile characterized by a relatively large background Richardson number. This is because the ratio between the second and the first term in (3.8) and (3.9) scales with $\mathrm{Ri}_{\mathrm{in}}^{1/2}$. Therefore, even without considering a specific wind profile we expect the second term to dominate for large $\mathrm{Ri}_{\mathrm{in}}$. Note, however, that this is a weaker criterion than the one used in Section 3.3.3, since it does not rely on singular behaviour (for which a term is infinitely larger than the other). Further clarification of this issue would require additional numerical simulations, which are beyond the scope of this study.

Concerning the applicability of the suggested diagnostic to real flows, difficulties may arise from the need to isolate the background flow from the total flow containing the wave perturbation. For this purpose, the wind field measured upstream of the mountain or averaged over the surrounding area may be used. It may also be challenging to distinguish between flow regions where the perpendicularity of the vectors is a signature of wave breaking and regions where this does not happen. Probably, an additional condition, involving the magnitude of the flow perturbation, will be necessary.

It is worth mentioning that developing methods to diagnose wave breaking without relying on the use of the Richardson number is a major goal for mountain wave CAT forecasting (Sharman *et al.*, 2012a). While in the idealized simulations presented in this study wave propagation is the only reason for the modulation of Ri, in real conditions Ri is a noisy variable, influenced by small-scale flow structures, displaying a large vertical-scale dependence. Even a flow with $\mathrm{Ri} > 1$ can be turbulent if this parameter is estimated at sufficiently coarse resolution. In this respect, the regime diagram presented in this study provides a way of predicting wave breaking based only on large-scale variables using the mountain height and background wind profile, thus avoiding dependence on the wave field itself.

The results presented in this study constitute a starting point for testing the applicability of these (idealized) simulation results to real flows. Future steps would entail carrying out numerical simulations with more realistic conditions, including: realistic orography, a PBL, non-hydrostatic effects, more complicated atmospheric profiles, etc. This should allow a better understanding of CAT generated by fully 3D mountain waves and the development of more specific tools to forecast it.

3.5 Appendix 3.A: Turbulent flow behaviour

As discussed in subsection 3.3.2, the regime diagram in Figure 3.3 depicts stability conditions under which a flow can become turbulent, although turbulence itself is not modelled in the experiments. In this appendix, simulations of the same atmospheric flows as in Figure 3.3 but where turbulent mixing is parametrized (via a turbulence closure) are presented. These experiments provide additional information about the generation of turbulence by mountain wave breaking.

3.5.1 Turbulence generated by shear and buoyancy production

The simulations including TKE use the same model set-up described in section 3.2.1, but a prognostic equation for the turbulent kinetic energy is employed. The parametrization scheme adopted (a 1.5 order turbulence closure) assumes fully three-dimensional sub-grid scale turbulence and is designed for high-resolution simulations ($\Delta x, \Delta y \leq 2$ km) (Skamarock *et al.*, 2005). While we refer to section 2.2.2 for further details about the parametrization scheme, it is worth mentioning that the "anisotropic mixing option" was chosen so that, in the computation of the horizontal and vertical eddy viscosities and mixing lengths according to (2.30), the anisotropy of the horizontal and vertical grids (i.e. $\Delta x, \Delta y \gg \Delta z$) is taken into account.

In order to have a full understanding of what type of instability mountain waves generate, the contributions of the two production terms (shear and buoyancy production) in (2.28) to the total model TKE were studied. More specifically, the eddy viscosities K_h and K_v, the 6 components of the deformation tensor (D_{11}, D_{22}, D_{33}, D_{12}, D_{13}, D_{23}) and the model-computed squared Brunt-Väisälä frequency (N^2) were extracted from the model output and used to compute the shear and buoyancy terms according to (2.29) and (2.31). In the computation of the two terms, the model code `module_diffusion_em.f90` (Skamarock *et al.*, 2005) was imitated.

While the variable "TKE" in output from the model corresponds to the total production of turbulent kinetic energy per unit of mass (sum of the TKE produced at previous time steps, shear and buoyancy production/destruction, dissipation and TKE fluxes, according to (2.28)), the shear and buoyancy terms computed as described above are instantaneous values per unit of mass per second. Thus, the present analysis is not meant to establish a TKE budget, as these three quantities (TKE and its

two source terms) are not comparable unless the model TKE tendency is also taken into account. Additionally, the dissipation term has not been computed.

The total model TKE (m^2 s^{-2}) for the simulation with $Ri_{in} = 1$ at $z \approx 2$ km is shown in Figure 3.9(a), the shear production (m^2 s^{-3}) in 3.9(b) and the buoyancy production (m^2 s^{-3}) in 3.9(c).

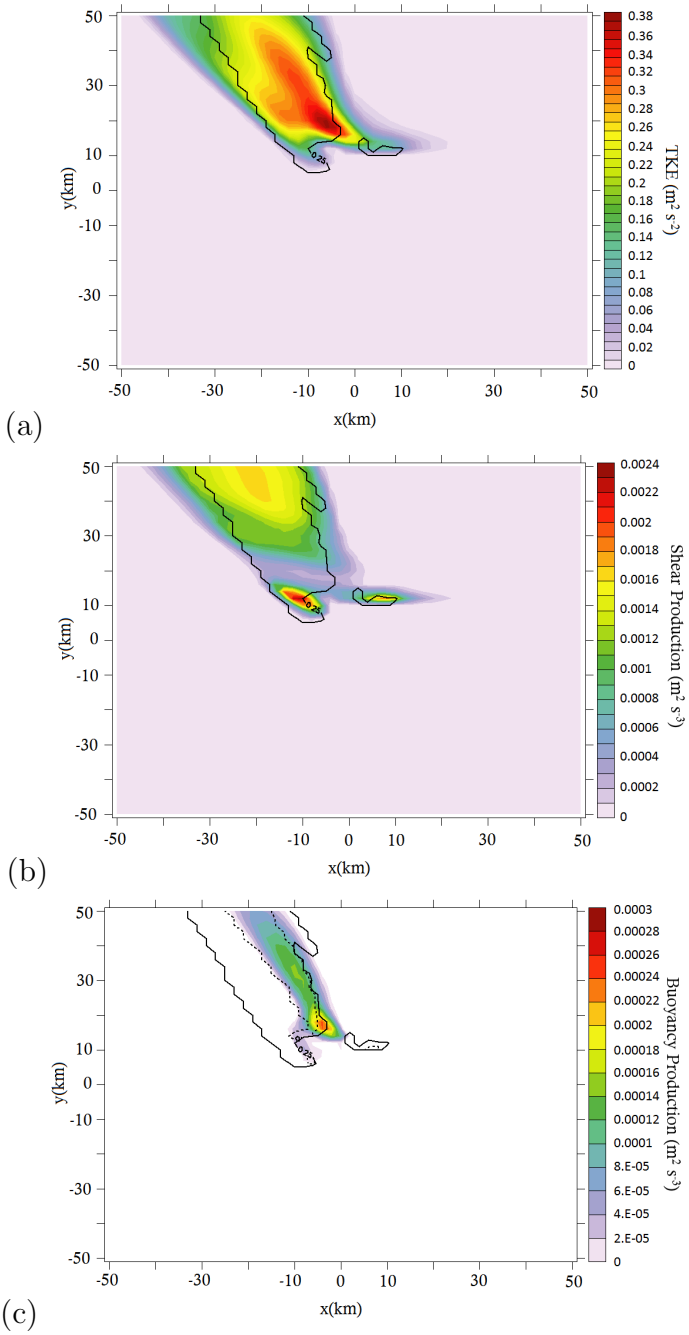

FIGURE 3.9: Horizontal flow cross-sections taken at $z \approx 2$ km for the experiment with $Ri_{in} = 1$ at the 18th hour of simulation. (a) is the total model TKE (m^2 s^{-2}), (b) is the shear production term (m^2 s^{-3}), (c) is the buoyancy production term (m^2 s^{-3}).

The solid contour line was added to facilitate the comparison with the corresponding $\mathrm{Ri}_{in} = 1$ inviscid simulation and corresponds to the $\mathrm{Ri}_{out} = 0.25$ contour line shown in Figure 3.8(c). The dashed line in Figure 3.9(c), instead, highlights regions where Ri_{out} becomes negative.

In Figure 3.9(a), the TKE produced by the model matches well the instability region predicted by the corresponding inviscid simulation (solid contour line). In Figure 3.9(b), the production of TKE by shear forces indicates that instabilities are generated by the vertical and horizontal shear of the flow (corresponding to the stress tensor in the model). The mechanism by which orographic waves affect the directional shear of the background flow has been discussed in section 3.3.2.2. Regions with a positive shear term, thus, correspond to regions where the wave perturbation is strong and the wind shear of the total flow is large. In Figure 3.9(c), the positive sign of the buoyancy term indicates that buoyancy forces favour the production of TKE. Indeed, according to (2.31), this situation corresponds to the presence of a layer with inverted potential temperature gradient where $N^2 < 0$. The region where the buoyancy term is positive corresponds to the flow overturning region predicted in the inviscid simulation (dashed contour line).

Comparing Figure 3.9(b) and (c), it can be seen that where the buoyancy production is a maximum, the shear production is minimum. Indeed, when flow overturning occurs, waves cease to propagate and break. Also, while overall the TKE region in Figure 3.9(a) resembles the pattern formed by the positive shear term in Figure 3.9(b), the maximum in TKE follows the elongated region where shear and buoyancy production are both active.

3.5.2 A TKE-based regime diagram

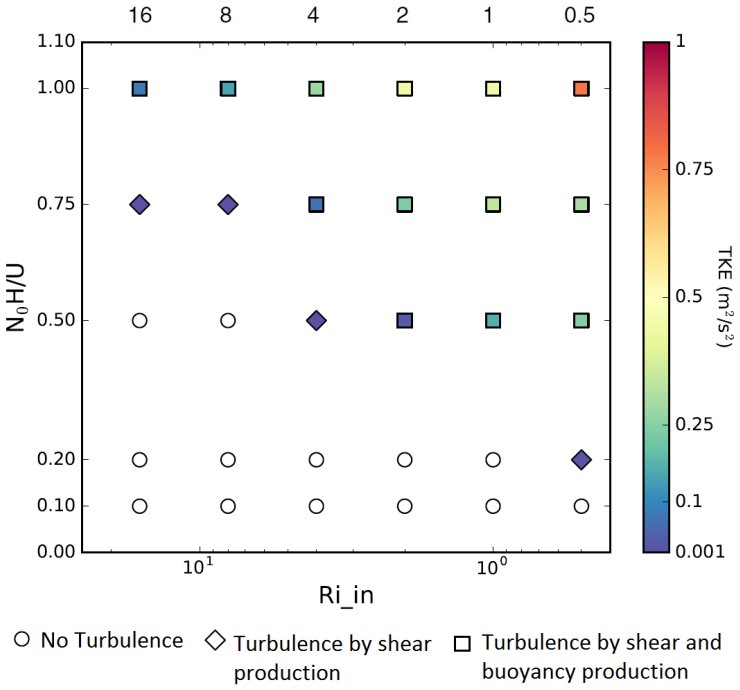

FIGURE 3.10: Regime diagram classifying the stability of the flow based on the production of turbulent kinetic energy. The color shading denotes the maximum TKE found for each flow configuration. Axes as in Figure 3.3.

In Figure 3.10 a regime diagram for the TKE simulations, analogous to the regime diagram for the inviscid experiments presented in Figure 3.3, is shown. Note that flows with $\mathrm{Ri}_{in} = \infty$ were not considered in this analysis, as no wave breaking was found for unsheared flows. In the TKE-based regime diagram, three categories are used to classify the stability of the flow: no turbulence (TKE $= 0$), turbulence by shear production (TKE > 0[1], shear term > 0, buoyancy term < 0 everywhere), turbulence by shear and buoyancy production (TKE > 0, shear term > 0, buoyancy term > 0 in at least one grid-point). The maximum TKE value found for each simulation is also shown (color shading).

As expected, flows in which wave breaking occurs are classified as turbulent due to shear and buoyancy production (squares). More interesting is the analysis of those flows characterized by a small but positive Ri_{min}, classified as "potentially turbulent" in the inviscid regime diagram. While some of these flows are confirmed to be turbulent and classified as turbulent due to shear production (diamonds), most of them (i.e. $\mathrm{Ri}_{in} = 16$, 8 and $N_0H/U = 0.5$, $\mathrm{Ri}_{in} = 2$ and $N_0H/U = 0.2$, $\mathrm{Ri}_{in} = 1$ and

[1]Because of numerical noise the actual threshold value used was somewhat larger than zero. In particular, TKE values of order 10^{-4} m^2 s^{-2} were excluded from the analysis.

$N_0H/U = 0.1$, 0.2, $\mathrm{Ri}_{in} = 0.5$ and $N_0H/U = 0.1$) are classified here as not turbulent (circles). Presumably, for these flows, the shear added by the wave propagation is not strong enough to initiate turbulence. However, it should be noticed that the results presented in this section depend on the type of turbulence closure adopted, hence they may be sensitive to the parameterization scheme.

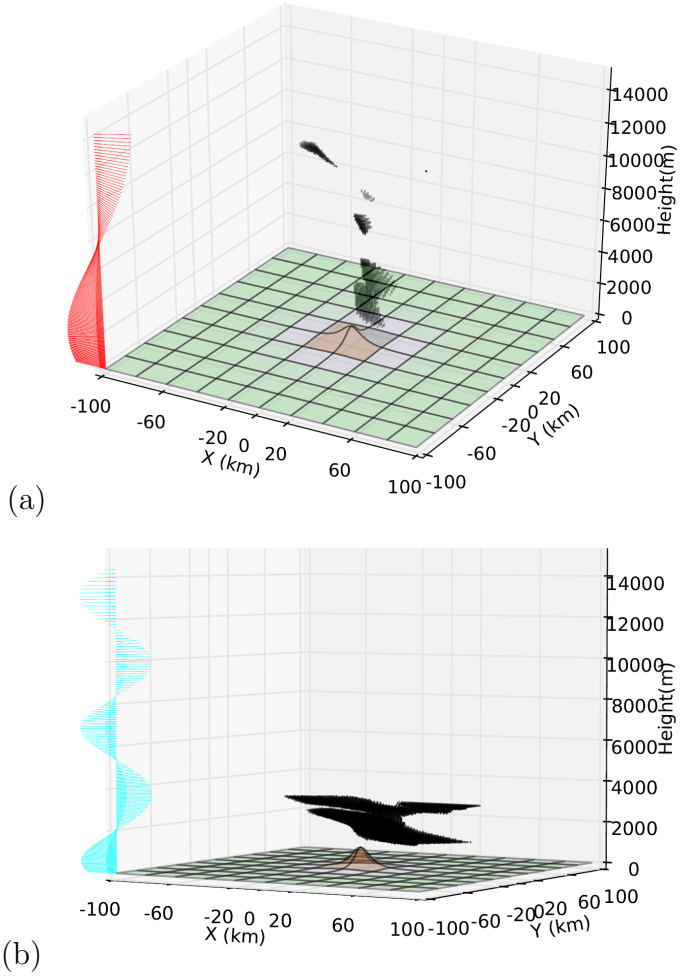

FIGURE 3.11: TKE regions for simulations with $N_0H/U = 1$ and $\mathrm{Ri}_{in} = 16$ (a) and $\mathrm{Ri}_{in} = 1$ (b). The plots refer to the 18th hour of the simulations. The profile of vectors on the left hand-side is as in Figure 3.6.

To conclude, in Figure 3.11 3D plots analogous to the ones presented in Figure 3.6(a) and 3.6(e) are shown. Here, the shaded surfaces represent regions where TKE is positive. For $\mathrm{Ri}_{in} = 16$ (Figure 3.11(a)), at high altitudes ($z \approx 7$ - 11 km) TKE regions correspond to $\mathrm{Ri}_{out} < 0.25$ regions in Figure 3.6(a). At these altitudes the buoyancy production term is positive. On the contrary, in the lower atmospheric layers, turbulence regions between 2 and 7 km result from shear instability only. In Figure 3.11(b), the TKE region resembles the region where $\mathrm{Ri}_{out} < 0.25$ in Figure 3.6(e), confirming its turbulent character.

3.6 Appendix 3.B: Testing a possible wave breaking diagnostic

In this section, the perpendicularity criterion between the horizontal velocity perturbation and background wind vectors, proposed as a wave breaking diagnostic in section 3.3.3, will be shortly tested. The tests that will be presented constitute a first attempt to use this diagnostic and, thus, should be interpreted as preliminary, and as a motivation for future work.

Continuing with the discussion in section 3.3.3, and focusing on the two cases of weak shear flow ($\mathrm{Ri}_{in} = 16$) and strong shear flow ($\mathrm{Ri}_{in} = 1$), the perpendicularity criterion was used to detect flow regions where the angle between (u_0, v_0) and (u', v') ranges from 80° to 130° (as observed in the flow cross-sections in Figure 3.8). The shape and extent of these regions was afterwards compared with the instability regions of Figure 3.6 (a) and Figure 3.6 (e), where $\mathrm{Ri}_{out} < 0.25$. The goal was to assess whether diagnostics based on the perpendicularity criterion can predict regions of low Ri_{out} and, thus, where wave breaking is expected.

The proposed diagnostic relied on the assumption that, at a critical level, (u_0, v_0) and (u', v') are approximately perpendicular. This perpendicularity, however, does not necessarily always correspond to wave breaking. Therefore it is necessary to distinguish between flow regions where the perpendicularity of the vectors is a signature of wave breaking and regions where this does not happen. Because the existence of wave breaking regions at critical levels is marked by large horizontal velocity perturbations (see Figure 3.8(a) and (c)) we used the magnitude of (u', v') as an additional constraint for our wave breaking detection algorithm.

The choice of a threshold value for $|(u', v')|$, however, was found to be particularly difficult, requiring some degree of arbitrariness. After some experimentation, the following algorithm was found to give overall the best performance:

- Within layers spanning each kilometre of the atmosphere the maximum horizontal velocity perturbation $|(u', v')|_{max}$ in the layer and the angle φ between (u_0, v_0) and (u', v') are computed;
- at each grid-point along the x-, y- and z- directions the following three conditions are evaluated: $80° \leq \varphi \leq 130°$, $|(u', v')| \geq 0.75|(u', v')|_{max}$, and $|(u', v')| > 1$ m s^{-1}. If all of them coexist, the grid-point is selected.

The velocity perturbations, counted as corresponding to wave breaking, range between 75% of $|(u', v')|_{max}$ and $|(u', v')|_{max}$ in each layer to take into account the variability of the velocity perturbation. The lower limit $|(u', v')| = 1$ m s^{-1} was chosen to eliminate from the analysis low velocities that are unlikely to be associated with wave breaking. Note that values used here were chosen empirically rather than from theoretically-based justifications, but suited the purpose of these preliminary tests.

The algorithm was run first without using the perpendicularity condition to test whether its contribution is significant compared to the sole use of the velocity perturbations. Figure 3.12(a) shows all the grid-points where $|(u', v')| \geq 0.75|(u', v')|_{max}$, and $|(u', v')| > 1$. The regions of large horizontal velocity perturbations seem to resemble the perturbation pattern of vertically propagating mountain waves. When the approximate perpendicularity condition is added (Figure 3.12(b)), the shaded regions at lower atmospheric levels disappear and the remaining grid-points are located at approximately the same altitudes where instability regions are predicted using $\mathrm{Ri}_{out} < 0.25$ (Figure 3.6(a)). Although this suggests that, by adding the perpendicularity condition, the algorithm can roughly catch altitudes where $\mathrm{Ri}_{out} < 0.25$ regions are expected, when Figure 3.6(a) and Figure 3.12(b) were compared quantitatively the agreement between the two methods was found to be modest. The number of grid-points that regions in Figure 3.6(a) and Figure 3.12(b) have in common is 139, which corresponds to $\approx 36\%$ of the total number of grid-points where $\mathrm{Ri}_{out} < 0.25$ in Figure 3.6(a) and to $\approx 10\%$ of the grid-points included in the surfaces in Figure 3.12(b). Indeed, flow regions selected by using the algorithm presented in Figure 3.12(b) are much wider than the ones in Figure 3.6(a) so it is not surprising that many grid-points where $\mathrm{Ri}_{out} > 0.25$ are included in them.

To test the resolution dependence of the algorithm, the algorithm was run again using a higher vertical resolution, so that $|(u', v')|_{max}$ was computed every 100 m of the atmosphere rather than every kilometre (not shown). The agreement with Figure 3.6(a) improved in terms of number of grid-points in common that are now 282, with an overlap between the wave breaking regions identified with the two methods of $\approx$ 73%, calculated with respect to the number of grid-points in Figure 3.6(a). However, the 'rate of success' of the algorithm did not change as 282 grid-points correspond, again, to only 10% of the total number of grid-points selected by the algorithm (figure not shown).

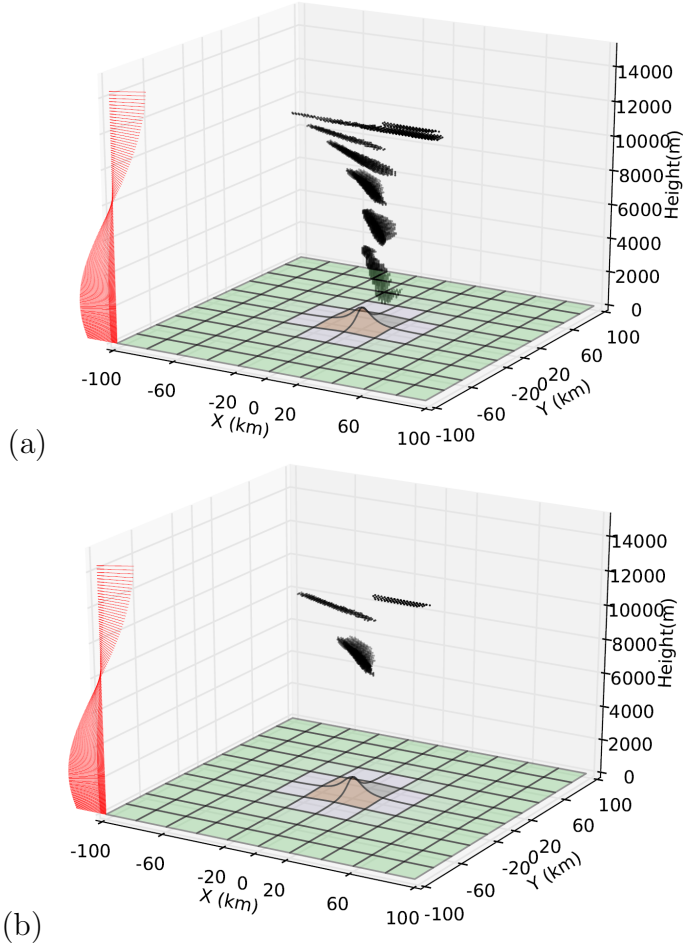

FIGURE 3.12: (a) Flow regions where $|(u', v')|$ varies between 0.75 $|(u', v')|_{max}$ and $|(u', v')|_{max}$ (computed in layers spanning 1km in the vertical). (b) flow regions as in (a) where additionally the angle φ between (u_0, v_0) and (u', v') is $80° \leq \varphi \leq 130°$. The plots refer to the 18th hour of the simulation with $N_0 H/U_0 = 1$ and $\mathrm{Ri}_{in} = 16$. The profile of vectors on the left hand-side is as in Figure 3.6.

The algorithm was also run for the strong shear flow case ($\mathrm{Ri}_{in} = 1$) (Figure 3.13). As discussed in section 3.3.2.2, in stronger shear flows most of the wave breaking occurs in the lower atmosphere, in a relatively thin layer, where many wave-numbers have critical levels and the magnitude of the horizontal velocity perturbation vector varies by a large amount (from 1 m s^{-1} to 9 m s^{-1} in the first 4 km of the atmosphere in Figure 3.6(e)). In these conditions using the algorithm was particularly challenging, and the best agreement, between Figure 3.6 (e) and Figure 3.13, corresponds to an intersection of $\approx 33\%$ (number of grid-points in common: 2626) of the number of grid-points in Figure 3.6 (e). This was found using layers of 100 m instead of 1km and requiring that the horizontal velocity perturbation satisfies: $|(u', v')| \geq 0.25|(u', v')|_{max}$. The surfaces bounding the diagnosed wave breaking regions in Figure

3.13 are again much wider than the ones in Figure 3.6 (e), and only $\approx 22\%$ of the grid-points in Figure 3.13 are grid-points where $\mathrm{Ri}_{out} < 0.25$.

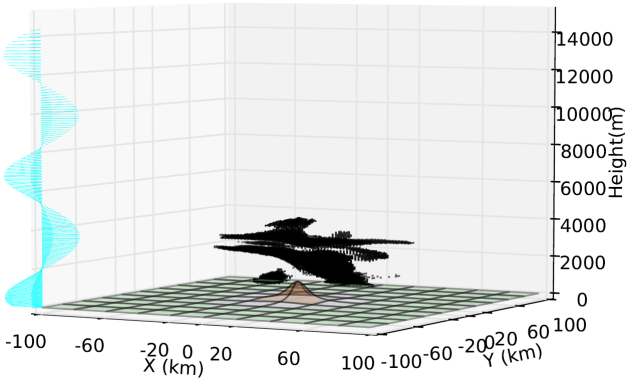

FIGURE 3.13: Flow regions where the angle φ between (u_0, v_0) and (u', v') is $80° \leq \varphi \leq 130°$, and where $|(u', v')|$ varies between 0.25 $|(u', v')|_{max}$ and $|(u', v')|_{max}$ (computed in layers spanning 100 m in the vertical). The plot refers to the 18th hour of the simulation with $N_0 H/U_0 = 1$ and $\mathrm{Ri}_{in} = 1$. The profile of vectors on the left hand-side is as in Figure 3.6.

In summary, the wave breaking detection algorithm proposed in this section performed rather poorly in the preliminary tests carried out. Possible ways to improve it could involve reviewing its formulation by trying to guide empirical choices using the physics of mountain waves at critical levels. For example, the range of variation of φ was chosen in accordance with what was detected in flow cross-sections. However, understanding what causes the variation of φ could lead to a more accurate prediction of the expected angle between the background wind vector and the horizontal velocity perturbation vector. Investigating whether that angle is influenced by the sense of rotation of the background wind with and/or by the relative orientation of the horizontal velocity perturbation vectors could be useful.

The choice of threshold values for $|(u', v')|$ was also arbitrary and varied between the two values of Ri_{in}, which is not very satisfactory. An alternative approach would be to focus on regions where the perturbation velocities exceed a significant fraction of the background flow, and thus to use velocity perturbations scaled by the background flow rather than by $|(u', v')|_{max}$. However, this would require quantifying empirically threshold values for the ratio between the velocity perturbations and the background flow.

The magnitude of (u', v') is only one of the possible additional constraints that can be used to define a CAT diagnostic. The perpendicularity condition could be combined, for example, with other quantities already used to diagnose CAT. Examples are: the

rate of deformation of the flow (the deformation tensor is also used to compute the shear TKE production term in the WRF's turbulence closure scheme, as described section 2.2.2), the TKE production itself, or the vertical velocity. These options could be considered in the future.

Chapter 4

Non-hydrostatic effects on mountain wave breaking in directional shear flows

In this chapter, mountain waves excited by a narrow 3D orography are investigated using idealized numerical simulations of atmospheric flows with directional wind shear. The stability of these waves is compared with the stability of hydrostatic mountain waves. The focus is on understanding how wave breaking is modified via gravity wave-critical level interaction, when non-hydrostatic (dispersive) effects arise. The influence of non-hydrostatic effects on wave breaking appears to be a function of the intensity of the background shear, increasing the stability of the flow (inhibiting wave breaking) for weak wind shear, but decreasing it instead (enhancing wave breaking) for stronger wind shear.

The work presented in this chapter has been submitted to the *Quarterly Journal of the Royal Meteorological Society, Notes and Correspondence*, with the reference: Guarino MV and Teixeira MAC, 2017. Non-hydrostatic effects on mountain wave breaking in directional shear flows. Q. J. R. Meteorol. Soc. - Status of the paper: accept subject to minor revisions.

4.1 Introduction

Non-hydrostatic mountain waves are primarily gravity waves excited by narrow orographic obstacles (so that the horizontal wave-number of the excited waves is large).

Because of their dispersive nature, in a stratified atmosphere with constant background parameters, these waves are thought to be less likely to break than hydrostatic mountain waves (Laprise and Peltier, 1989). The generation of approximately hydrostatic mountain waves is favoured either by a strongly stable atmospheric stratification (i.e. a large Brunt-Väisälä frequency N_0), a weak background wind (U) or a broad orography (i.e. a large mountain half-width a), so that $N_0 a/U \gg 1$. On the contrary, non-hydrostatic mountain waves are expected for a weak stratification, a strong background wind or a narrow orography, so that $N_0 a/U \lesssim O(1)$. When U and N_0 are constant with height, the character of the gravity waves launched by a mountain depends on the horizontal scale of the orography only (Holton and Hakim, 2012). In the wide mountain limit, small horizontal wave-numbers dominate the wave spectrum: in this case the wave propagation and the energy transport are mostly vertical. In the narrow mountain limit, large horizontal wave-numbers dominate the wave spectrum and the wave propagation is partly horizontal, while the wave amplitude decays with height. Under these conditions the vertical velocity perturbations are not in hydrostatic balance.

Several studies investigated the dynamics of gravity waves in the two limits of vertically propagating and trapped lee waves, the latter being highly non-hydrostatic waves generated as a consequence of an increase in wind speed and/or a decrease in atmospheric stability with height (Scorer, 1949, Durran, 1986). Studies of hydrostatic mountain waves focused particularly on wave momentum deposition, wave breaking, and down-slope wind storms (e.g. McFarlane, 1987, Clark and Peltier, 1977, Bacmeister and Schoeberl, 1989, Teixeira *et al.*, 2004, Doyle and Reynolds, 2008); studies of trapped lee waves, on the other hand, mainly focused on lee wave rotors, surface drag, and orographic rain-bands (e.g. Vosper, 2004, Kirshbaum *et al.*, 2007, Stiperski and Grubišić, 2011, Teixeira *et al.*, 2013).

Fewer studies investigated the dynamics of non-trapped mountain waves when $N_0 a/U = O(1)$ (e.g. Zängl, 2003, Sachsperger *et al.*, 2016). These are dispersive waves with short horizontal wavelengths partly able to propagate vertically and downstream of the orography that originated them. Because of destructive interferences taking place as waves propagate in the presence of dispersion, the wave amplitude decreases with distance away from their source (Nappo, 2012). For a wind profile with directional shear, the dispersive nature of these waves may influence wave breaking occurrence via modification of the wave-critical level interaction, where critical levels correspond to those heights at which gravity waves amplify and may become unstable. Indeed, depending upon the strength of dispersion effects, less or more wave energy (as we shall see) may be available to be dissipated at critical levels.

The conditions under which hydrostatic mountain waves can break and initiate turbulence in the presence of directional wind shear have been studied in chapter 3. Here, the influence of non-hydrostatic effects on mid-tropospheric mountain wave breaking is analysed by taking into account the aforementioned dispersion effects, and also how the scaling of the velocity perturbations changes in non-hydrostatic flow.

In section 4.2, the set-up of numerical simulations and the method used to identify wave breaking within the simulation domain are briefly recalled. In section 4.3, the stability of the flow in the transition from hydrostatic to non-hydrostatic mountain waves is discussed. In section 4.4, the conclusions of this chapter are summarized.

4.2 Methodology

4.2.1 Numerical simulations

The idealized numerical simulations presented in this chapter use the same set-up of chapter 3 (section 3.2.1), with the only differences being the mountain half-width, grid spacing and number of grid-points. The flow under consideration is adiabatic (i.e. no heat or moisture fluxes from the surface), inviscid (i.e. explicit diffusion not allowed anywhere, and no planetary boundary layer scheme used), and the Coriolis force is neglected.

The simulations were performed using the WRF-ARW atmospheric model. The computational domain comprised 200 grid-points in both the x and $y-$directions, with an isotropic grid spacing $\Delta x = \Delta y = 500$ m. Such a high horizontal resolution was chosen to resolve properly the narrow mountains used in the simulations. The model vertical grid contained 200 eta levels (using a terrain-following hydrostatic-pressure coordinate), with spacing near the ground of 45 m and spacing at the top of the domain, 20 km above ground level (a.g.l.), of 450 m. A 5 km-deep absorbing sponge layer at the top of the domain was used to control wave reflection from the upper boundary. For those experiments performed with the strongest directional shear considered in this study, some adjustments were made to the model set-up to ensure numerical stability, namely: the top of the domain was raised to 30 km, the depth of the absorbing layer was increased to 15 km, and 400 eta vertical levels were used.

The model was initialized using an orography profile described by a 3D bell-shaped mountain:

$$h(x,y) = \frac{H}{\left(\frac{x^2}{a^2} + \frac{y^2}{a^2} + 1\right)^{3/2}}, \tag{4.1}$$

where H is the maximum mountain height.

Non-hydrostatic mountain waves were generated by imposing $a = 2.5$ km, $U = 10$ $\mathrm{m\,s^{-1}}$ and $N_0 = 0.01$ $\mathrm{s^{-1}}$, so that $N_0 a/U = 2.5$. Note that this value of $N_0 a/U$ leads to mountain waves that are moderately non-hydrostatic. The flow could be made even more non-hydrostatic by using a lower $N_0 a/U$, however as N_0 and U were chosen to be consistent with the simulations presented in chapter 3, and a smaller a would correspond to unrealistically steep orography, $N_0 a/U = 2.5$ is near the smallest realistic value consistent with the chosen maximum value of H (see below). Furthermore, strongly non-hydrostatic waves are limited in their vertical propagation (as will be discussed later) and hence are not so relevant to mid-tropospheric wave-breaking.

In the experiments, different degrees of flow non-linearity (associated with different wave amplitudes) were considered by using 5 values of the mountain height: $H =$ 100 m, 200 m, 500 m, 750 m, 1 km. The vertical aspect ratio of the mountain H/a varies in the range [0.04 - 0.4], and the non-dimensional mountain height defined in terms of N_0 and U takes the values $N_0 H/U = 0.1$, 0.2, 0.5, 0.75, 1. For each orography configuration, 6 simulations using wind profiles with different intensities of the directional shear of the background flow were performed. This was determined by changing the rate of wind turning with height β, which depends on the Richardson number of the background flow Ri_{in} (for N_0 and U constant with height) according to:

$$u_0 = U\cos(\beta z), \qquad v_0 = U\sin(\beta z), \tag{4.2}$$

where u_0 and v_0 are the background wind components and $\beta = N_0/(U\sqrt{\mathrm{Ri_{in}}})$. More specifically, the values considered are: $\mathrm{Ri}_{in} = 16$, 8, 4, 2, 1, 0.5, which correspond to $\beta \approx 14$ degrees/km, 20 degrees/km, 31 degrees/km, 40 degrees/km, 57 degrees/km, 80 degrees/km. Therefore, as Ri_{in} decreases the rate of wind turning increases, resulting in flows with stronger directional wind shear.

4.2.2 Wave breaking diagnosis

The Richardson number of the flow including the wave perturbation, Ri_{out}, was used to detect instability regions within the simulation domain. The three-dimensional

$\mathrm{Ri}_{out}(x, y, z)$ field was computed at each grid-point using centred finite differences. Although Ri is notoriously sensitive to the depth of the layer in which the potential temperature and the wind gradients are calculated, the fairly high vertical resolution employed in the simulations guarantees that waves (and their overturning) are sufficiently well resolved everywhere in the simulation domain. Therefore, Ri_{out} is expected to provide reliable indications on the stability of the flow.

The $\mathrm{Ri}_{out}(x, y, z)$ field was used in the analysis of the results with the twofold aim of:

- Identifying the minimum Ri value in the field (Ri_{min}) for each experiment. When Ri_{min} is negative, flow overturning by wave breaking is assumed to occur in the simulation domain. Ri_{min} values are used to produce a regime diagram describing the wave breaking behaviour in the transition from linear to non-linear flows and from weak to strong directional shears.

- Delimiting regions where the wave propagation and breaking lead to the generation of dynamical ($\mathrm{Ri}_{out} < 0.25$) and/or convective ($\mathrm{Ri}_{out} < 0$) instabilities. Under these conditions the flow can potentially evolve into turbulence, hence these may be regarded as potentially turbulent regions.

As in chapter 3, the Ri_{out} field was computed within a 'region of interest' delimited by upper, lower and lateral bounds. While for a more in-depth discussion and justification for the choice of these bounds we refer to section 3.2.2, we recall here that: the upper limit is $z \approx 14$ km, as it corresponds approximately to the height of the bottom of the sponge layer; the lower limit is $z \approx 1$ km, as in more realistic conditions this would correspond to the height of a fully developed Planetary Boundary Layer; the lateral limits represent a square region of 50×50 km surrounding the mountain (25 km to the east, west, north and south from the centre of the mountain). Note that while for the simulations presented in chapter 3 (where $a = 10$ km) the region of interest had dimensions 100×100 km, spanning from -5 X/a to +5 X/a along x and from -5 Y/a to +5 Y/a along y (where X/a and Y/a are distances relative to the mountain located at (X=0 ,Y=0)), for the simulations presented here (where $a =$ 2.5 km) the region of interest spans from -10 X/a to +10 X/a and from -10 Y/a to +10 Y/a instead. Considering larger relative distances is consistent with the dynamics of the more non-hydrostatic waves investigated in the present study, as these are expected to propagate more laterally than hydrostatic waves, resulting in more extended downwind disturbances (Nappo, 2012). In the following section, the dynamics of non-hydrostatic mountain waves will be discussed in more detail.

4.2.3 Non-hydrostatic mountain waves

In its most general form, the Taylor-Goldstein equation for adiabatic, 3D, frictionless flows without rotation takes the form (Nappo, 2012):

$$\frac{d^2\widehat{w}}{dz^2} + \left[\frac{N_0^2 k_H^2}{(ku_0 + lv_0)^2} - \frac{ku_0'' + lv_0''}{ku_0 + lv_0} - k_H^2\right]\widehat{w} = 0, \tag{4.3}$$

where $\widehat{w}$ is the Fourier transform of the vertical velocity, k and l are the horizontal wave-numbers along the x and $y-$directions, $k_H = \sqrt{k^2 + l^2}$ is the magnitude of the horizontal wave-number vector and the primes denote differentiation with respect to z.

In vertically sheared flows, the solution to (4.3) can be expressed as:

$$\widehat{w}(k, l, z) = \widehat{w}(k, l, 0)\mathrm{e}^{i\int_0^z m(z)dz}, \tag{4.4}$$

where m is the vertical wave-number. Equation (4.4) is subject to the lower boundary condition:

$$\widehat{w}(k, l, 0) = i(ku_0 + lv_0)\widehat{h}(k, l), \tag{4.5}$$

where $\widehat{h}(k, l)$ is the Fourier transform of the terrain elevation $h(x, y)$. The last term in (4.3), involving k_H^2, accounts for the vertical acceleration of air parcels flowing across the mountain and is only present in the wave equation when this acceleration is important, thus accounting for non-hydrostatic effects.

By substituting (4.4) into (4.3) and adopting a zeroth-order WKB approximation, the vertical wave-number m is defined as:

$$m = \left[\frac{N_0^2 k_H^2}{(ku_0 + lv_0)^2} - k_H^2\right]^{1/2}. \tag{4.6}$$

In the hydrostatic limit ($N_0 a/U \gg 1$), k_H is negligible so that $m = N_0 k_H/(ku_0 + lv_0)$. In the strongly non-hydrostatic limit ($N_0 a/U \ll 1$), buoyancy forces are unimportant compared to k_H and the vertical wave-number is imaginary: $m = ik_H$. In the first case, the wave propagation is vertical and governed by buoyancy forces. In the second case, the generation of vertically-propagating gravity waves is inhibited and disturbances propagate in the horizontal direction as evanescent waves trapped at the lower boundary. The present study stands somewhere in between these two limit cases, as non-hydrostatic (but still vertically-propagating) gravity waves, with a dispersion relationship given by (4.6), are investigated.

According to (4.6), the dependence of the vertical wave-number on the horizontal wave-number introduces dispersion effects to the gravity wave dynamics in addition to those associated with the three-dimensionality of the flow. Indeed, because of the presence of the term $(ku_0 + lv_0)$ in (4.6), 3D hydrostatic mountain waves are already dispersive. This type of dispersion (often termed 'directional dispersion') causes the wave energy to spread along a parabola that widens with height, causing the waves to weaken as they propagate upwards (Smith, 1980). The dispersion added by the non-hydrostatic term in (4.6) decreases the total wave energy density by allowing horizontal wave propagation and downstream spatial spreading of the wave packet, as can be deduced from group velocity arguments.

4.3 Results and discussion

4.3.1 Non-hydrostatic effects on wave breaking

Figure 4.1 shows vertical cross-sections of w and the horizontal velocity perturbation $|(u', v')|$ for two simulations with $\mathrm{Ri}_{in} = 16$ and $H = 1$ km in the case of hydrostatic (Figure 4.1(a) and 4.1(c)) and non-hydrostatic (Figure 4.1(b) and 4.1(d)) mountain waves. The cross-sections were taken at $\mathrm{Y}/a = +3.6$ where, in the hydrostatic case, wave breaking occurs. The black contours correspond to $\mathrm{Ri}_{out} < 0$.

In Figure 4.1(a) and 4.1(c), hydrostatic waves propagate vertically up to $z \approx 12$ km. For non-hydrostatic mountain waves, a roughly similar flow behaviour is observed, but in Figure 4.1(b) the wave propagation shows a significant downstream component, highlighting the dispersive nature of the disturbance. While hydrostatic waves break at $z \approx 10$ km (where $\mathrm{Ri}_{out} < 0$), the breaking region is absent in Figure 4.1(b) and 4.1(d). Since in directional shear flows the existence/location of critical levels depend on the relative orientation of the background wind vector and the horizontal wave number vector, and the two simulations were initialized with the same wind profile and orography, we can assume that the same directional critical levels exist in both flow configurations. However, for non-hydrostatic mountain waves the wave dispersion presumably makes the wave energy decay faster, producing destructive interferences as the waves propagate. As a consequence, for wave packets approaching the critical level at $z \approx 10$ km, the wave energy is not concentrated enough to cause flow overturning and wave breaking.

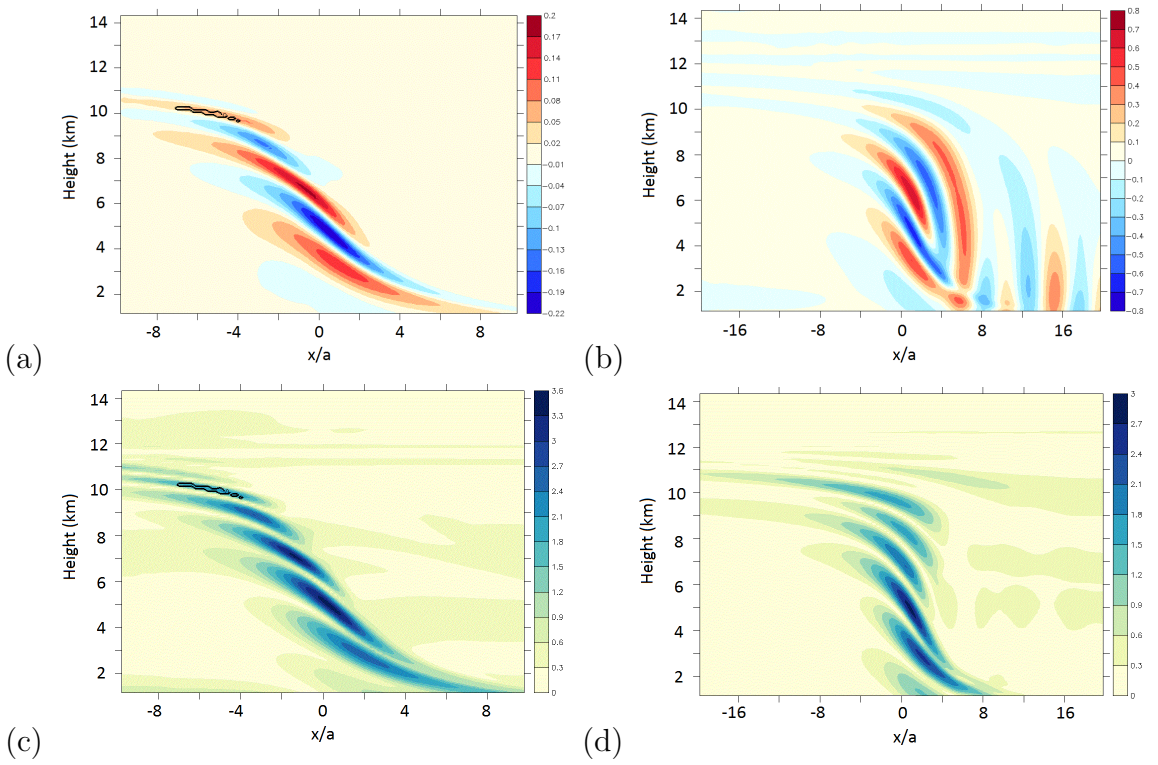

FIGURE 4.1: Vertical cross-sections of w ((a) and (b)) and the magnitude of the wave horizontal velocity perturbation vector (u', v') ((c) and (d)) at $Y/a = +\,3.6$ for simulations with $\mathrm{Ri}_{in} = 16$ and $N_0 H/U = 1$. (a) and (c) show hydrostatic mountain waves ($a = 10$ km), (b) and (d) show non-hydrostatic mountain waves ($a = 2.5$ km). The black contours indicate regions where $\mathrm{Ri}_{out} < 0$.

As a further confirmation, while Ri_{min} in the hydrostatic waves occurs at $z \approx 10$ km ($\mathrm{Ri}_{min_H} =$ - 23), for non-hydrostatic waves Ri_{min} occurs at much lower altitudes $z \approx 3$ km ($\mathrm{Ri}_{min_{NH}} = 0.75$) where, plausibly, dispersive effects are less effective. Indeed, the cumulative effect of dispersion becomes stronger in the far-field, after waves have propagated over long distances. Besides dispersive effects, hydrostatic and non-hydrostatic mountain waves differ in the scaling of key flow parameters (namely the horizontal velocity perturbations), as is discussed below.

In Figure 4.1(b) non-hydrostatic mountain waves exhibit near the surface a vertical velocity which is 4 times larger than the vertical velocity for hydrostatic waves (the maximum on the w scale is 0.2 in Figure 4.1(a) and 0.8 in Figure 4.1(b)). This can be explained via the bottom boundary condition (4.5), from which w scales as $\frac{UH}{a}$ (both for hydrostatic and non-hydrostatic waves). Because the a used in the non-hydrostatic simulations is 4 times smaller than the one used in the hydrostatic simulations, the corresponding w field in Figure 4.1 has a magnitude that is 4 times larger than the one for hydrostatic waves ($w_{NH} \approx 4\ w_H$).

The scaling predicted by linear theory for the horizontal velocity perturbations must be distinguished between the hydrostatic and non-hydrostatic cases. From mass conservation, and for the flow parameters considered here, it can be shown that while in the hydrostatic case this scaling is $v'_H \sim u'_H \sim \frac{Na}{U} w_H \approx 10\ w_H$, in the strongly non-hydrostatic case $v'_{NH} \sim u'_{NH} \sim w_{NH} \approx 4\ w_H$.

The flow cross-sections in Figure 4.1(c) and 4.1(d) show that the horizontal velocity perturbation is larger than the hydrostatic estimate of 2 m s^{-1} for the hydrostatic case (Figure 4.1(c)), and much larger than the strongly non-hydrostatic estimate of 0.8 m s^{-1} for the non-hydrostatic case (Figure 4.1(d)). What this means is that the hydrostatic scaling still applies more closely to the non-hydrostatic case than the strongly non-hydrostatic scaling (which is only valid when the effects of stratification are vanishingly weak). Note, however, that the horizontal velocity perturbation is slightly smaller in the non-hydrostatic case because of influence (albeit weak) from the non-hydrostatic scaling. It should also be kept in mind that the scalings of the horizontal velocity perturbations described above are strictly valid for linear flows, but the flows in Figure 4.1 are highly non-linear (as testified by the presence of wave breaking).

The interplay between the scaling of the velocity perturbations and the wave dispersion effects is not trivial, as both these mechanisms contribute to determine the wave amplitude and, thus, the likeliness of wave breaking. It should be noted, additionally, that the scalings presented above are applicable locally near the surface (they use the orography width as a horizontal length scale, for example), whereas the effect of dispersion is intrinsically related to the propagation of the waves. The role of each of these two mechanisms in wave breaking is discussed in the following section.

4.3.2 A regime diagram for non-hydrostatic mountain waves

In Figure 4.2, a regime diagram describing the stability of the flow as a function of its non-linearity (quantified through N_0H/U) and directional shear intensity (quantified through Ri_{in}) is presented. This regime diagram is directly comparable with the regime diagram for hydrostatic waves presented in Figure 3.3 of Chapter 3. The likeliness of wave breaking is diagnosed by using $\mathrm{Ri}_{min_{NH}}$, calculated for each numerical simulation, after the surface drag stabilizes to a constant value. The four $\mathrm{Ri}_{min_{NH}}$ categories, chosen in accordance with the background literature, are: $\mathrm{Ri}_{min_{NH}} < 0$ (squares) indicating convective instability due to wave breaking events (category 1), $0 < \mathrm{Ri}_{min_{NH}} \leq 0.25$ (triangles) indicating dynamic instability, which is potentially an index of turbulence (category 2), $0.25 < \mathrm{Ri}_{min_{NH}} \leq 1$ (diamonds) indicating a

flow having enough kinetic energy available for turbulent mixing (category 3), and $\mathrm{Ri}_{min_{NH}} > 1$ (circles), indicating non-turbulent flow where no wave breaking events occur (category 4).

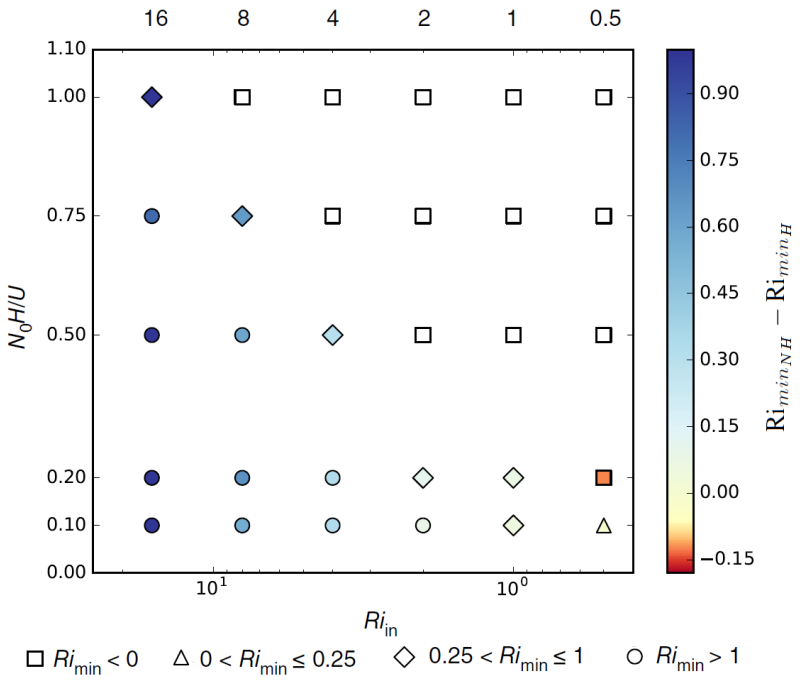

FIGURE 4.2: Regime diagram describing flow stability and likeliness of wave breaking as a function of N_0H/U and $\mathrm{Ri}_{\mathrm{in}}$. The $\mathrm{Ri}_{\mathrm{in}}$ values use a logarithmic scale, however the actual $\mathrm{Ri}_{\mathrm{in}}$ values considered are shown on the upper horizontal axis.

The colours in Figure 4.2 denote the difference between the $\mathrm{Ri}_{min_{NH}}$ values obtained from the non-hydrostatic simulations and the corresponding Ri_{min_H} values for hydrostatic waves in Figure 3.3. This allows us to visualize in which areas of the regime diagram the non-hydrostatic effects: stabilize the flow (positive differences), increase its instability (negative differences), or leave it unaltered (differences near zero). Because the information about the changes in flow stability is given by the sign of the quantity $(\mathrm{Ri}_{min_{NH}} - \mathrm{Ri}_{min_H})$ and because positive differences were found to be larger than negative ones, the scale is bounded between -0.2 and 1. Also note that when Ri_{min} is negative in both non-hydrostatic and hydrostatic conditions, the value of $(\mathrm{Ri}_{min_{NH}} - \mathrm{Ri}_{min_H})$ is ignored (white squares in Figure 4.2). This is because, for the purposes of our analysis, once the Richardson number drops below zero, any negative value has roughly the same meaning in terms of flow instability, and large differences that might occur would convey a misleading idea about their physical significance.

Just as in the hydrostatic waves case, wave breaking is more likely to happen for flows with low Ri_{in} and high N_0H/U, which is expected physically. However, while

on the left-hand side of the regime diagram ($\mathrm{Ri}_{in} = 16, 8$) the non-hydrostatic effects tend to stabilize the flow ($\mathrm{Ri}_{min_{NH}} > \mathrm{Ri}_{min_H}$), on the right-hand side ($\mathrm{Ri}_{in} = 0.5$) the instability of the flow becomes stronger ($\mathrm{Ri}_{min_{NH}} < \mathrm{Ri}_{min_H}$).

Details about the changes in flow stability observed in the transition from hydrostatic to non-hydrostatic waves are summarized in Table 4.1. Of particular interest are the changes in flow stability for the cases where:

- $\mathrm{Ri}_{in} = 16$ and $N_0H/U = 1$. In this case, non-hydrostatic mountain waves are not able to perturb the background flow as strongly as hydrostatic waves ($\mathrm{Ri}_{min_{NH}} > \mathrm{Ri}_{min_H}$) and the wave breaking that was observed in the hydrostatic waves case no longer occurs;
- $\mathrm{Ri}_{in} = 0.5$ and $N_0H/U = 0.2$. Here $\mathrm{Ri}_{min_{NH}} < \mathrm{Ri}_{min_H}$, and $\mathrm{Ri}_{min_{NH}}$ is negative. Hence, non-hydrostatic mountain waves break, originating overturning regions not present in the hydrostatic simulations.

On the left-hand side of the regime diagram, for the largest values of R_{in}, the increased stability of the flow can be explained by the dispersion effects discussed in the previous section and illustrated in Figure 4.1(b). On the right-hand side, for the lowest values of Ri_{in}, the larger instability of the flow is probably a result of the larger value of w in the non-hydrostatic simulations, the weakening of dispersion effects in strong directional shear, and non-linear effects, as will be discussed further below.

As discussed in section 3.3.2, for wind profiles with a fast rate of wind turning with height, a high density of critical levels exists at low levels in the atmosphere. Directional critical levels for a particular wave-number in the wave spectrum are defined as the heights where the background wind vector is perpendicular to the horizontal wave number vector, so that in (4.6) $ku_0 + lv_0 = 0$ and consequently $m \to \infty$. Figure 4.3 shows all the grid-points where $\mathrm{Ri}_{out} < 0.25$ for the numerical simulations with $N_0H/U = 1$. The $\mathrm{Ri}_{out} < 0.25$ field corresponds to dynamical instability regions, which may contain smaller regions where the flow overturns ($\mathrm{Ri}_{out} < 0$). In the strongest shear flow considered in this study, where $\mathrm{Ri}_{in} = 0.5$, the wind rotates by 180 degrees in the first 2.5 km of the atmosphere, hence the condition $ku_0 + lv_0 = 0$ occurs at least once for each wave-number in the wave spectrum over this depth. Waves are likely to break at the lowest critical level they encounter, therefore the majority of the wave energy is expected to dissipate by wave breaking within the first 2.5 km of the atmosphere. A similar kind of behaviour is observed for the other wind profiles employed, with the instability regions extending across deeper atmospheric layers in weaker shear flows.

TABLE 4.1: Summary of the results in Figure 4.2, including details about changes in flow stability observed in the transition from hydrostatic to non-hydrostatic waves, namely: flow type (Ri_{in} and N_0H/U), Ri_{min} for hydrostatic and non-hydrostatic mountain waves, observed changes in flow stability and corresponding flow regimes. For any parameter combinations not shown the flow class remained unchanged.

Flow type	Ri_{min_H}	$\mathrm{Ri}_{min_{NH}}$	Stability	Flow regime
$\mathrm{Ri}_{in} = 16$, $N_0H/U = 0.5$, 0.75	[0.25, 1]	> 1	increasing	may evolve into turbulence → stable
$\mathrm{Ri}_{in} = 16$, $N_0H/U = 1$	< 0	[0.25, 1]	increasing	convective instability → may evolve into turbulence
$\mathrm{Ri}_{in} = 8$, $N_0H/U = 0.5$	[0.25, 1]	> 1	increasing	may evolve into turbulence → stable
$\mathrm{Ri}_{in} = 8$, $N_0H/U = 0.75$	[0, 0.25]	[0.25, 1]	increasing	dynamical instability → may evolve into turbulence
$\mathrm{Ri}_{in} = 0.5$, $N_0H/U = 0.1$	[0.25, 1]	[0, 0.25]	decreasing	may evolve into turbulence → dynamical instability
$\mathrm{Ri}_{in} = 0.5$, $N_0H/U = 0.2$	[0, 0.25]	< 0	decreasing	dynamical instability → convective instability

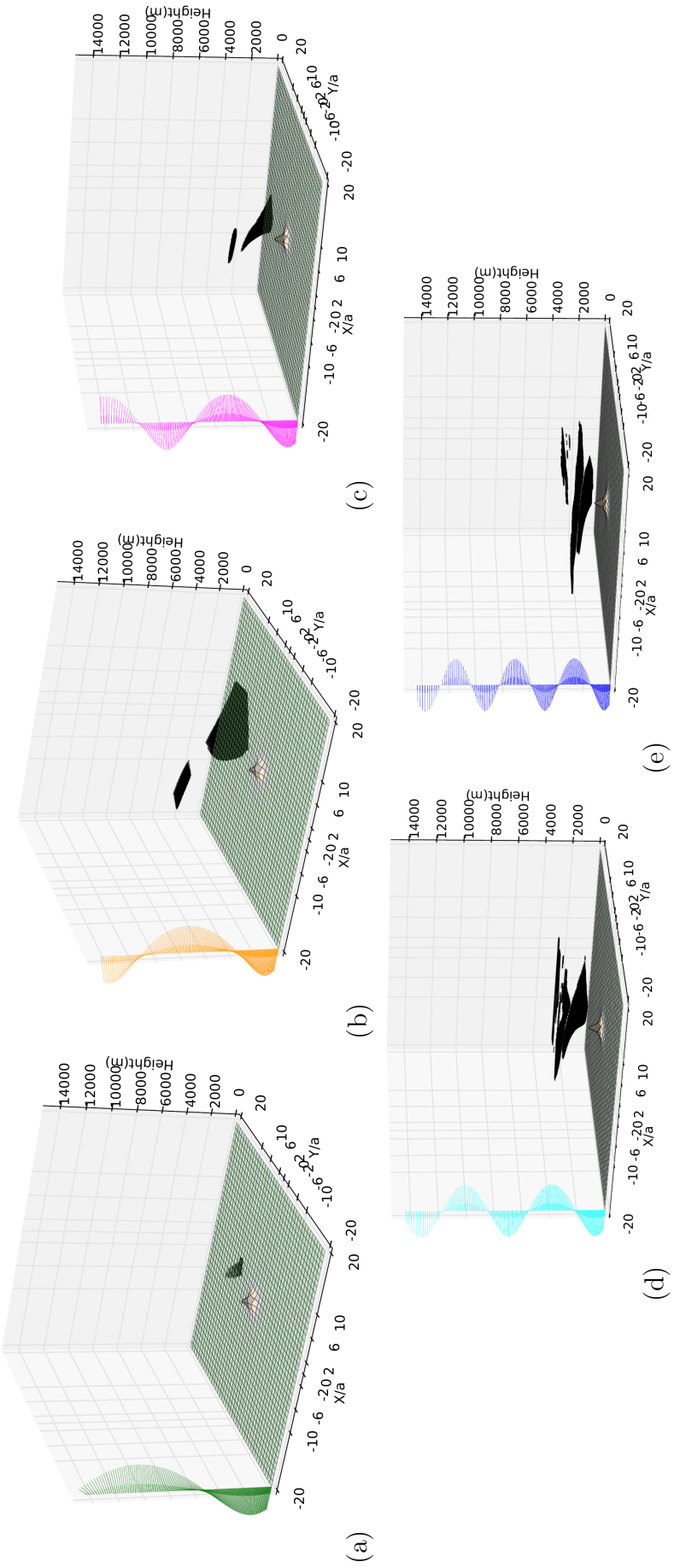

FIGURE 4.3: 3D perspective of the flow showing every point in the computational domain where $\mathrm{Ri}_{\mathrm{out}} < 0.25$. All panels refer to simulations performed with $N_0 H/U = 1$ and different wind shear intensities: (a) $\mathrm{Ri}_{\mathrm{in}} = 8$, (b) $\mathrm{Ri}_{\mathrm{in}}$=4, (c) $\mathrm{Ri}_{\mathrm{in}} = 2$, (d) $\mathrm{Ri}_{\mathrm{in}} = 1$, (e) $\mathrm{Ri}_{\mathrm{in}} = 0.5$. On the left-hand side of each plot, a representation of the wind profile used in the simulations is shown. The wind profile has a helical shape corresponding to a wind that is westerly at the surface and rotates anticlockwise as z increases.

Because wave-dispersion is a function of the distance over which waves propagate (i.e. it becomes cumulatively stronger at large – vertical or horizontal – distances from the mountain), dispersive effects are stronger for waves travelling up to 12 km (Ri_{in} = 16, 8, 4), and much weaker for waves travelling for less than 2.5 km before they reach their critical levels (where, incidentally, they become nearly perfectly hydrostatic) and break ($\mathrm{Ri}_{in} = 0.5$). Also note that in Figure 4.3(a), for $\mathrm{Ri}_{in} = 8$, instabilities occur at low levels, and the higher-altitude overturning regions observed in the hydrostatic case (see Chapter 3 Figure 3.6(b)) are absent, confirming that dispersion limits the wave amplitude at higher altitudes and, thus, selectively influences the wave-critical level interaction.

As discussed in subsection 4.3.1, while $w_{NH} \approx 4\ w_H$ in the simulations, u'_{NH} is only slightly smaller than u'_H (see also Figure 4.1(c) and 4.1(d)). This leads to a higher total wave kinetic energy, enhancing wave amplitude and likeliness of breaking at critical levels (where $w \to 0$ and $(u', v') \to \infty$ according to linear theory (Shutts, 1998)). As a consequence, at the same critical level, the wave amplitude is expected to increase more markedly for non-hydrostatic than for hydrostatic flow. Thus, in the absence of significant dispersion, non-hydrostatic mountain waves may become unstable and break where hydrostatic mountain waves do not. This probably explains why in Figure 4.2, when $\mathrm{Ri}_{in} = 0.5$ and $N_0H/U = 0.1$, $\mathrm{Ri}_{min_{NH}} < \mathrm{Ri}_{min_H}$ and the decrease in $\mathrm{Ri}_{min_{NH}}$ (albeit small) causes the flow to shift from category 3 (for hydrostatic waves) to category 2. When the mountain height increases even further, so that $N_0H/U = 0.2$, the wave amplitude is large enough to cause flow overturning and wave breaking. For larger N_0H/U no differences are observed, as wave breaking is expected also in the hydrostatic regime. An alternative, but probably equivalent, interpretation of this behaviour is that wave non-linearity is not only controlled by N_0H/U, but also increasingly by H/a as the flow becomes more non-hydrostatic. Since H/a is larger by a factor of 4 here than in the hydrostatic simulations of chapter 3, this may explain why wave breaking can become more likely despite the contrary effect of wave dispersion.

To conclude, the stability of flows where $\mathrm{Ri}_{in} = 4$ and 2, in the centre portion of the regime diagram in Figure 4.2, is not significantly affected by non-hydrostatic effects. The differences ($\mathrm{Ri}_{min_{NH}} - \mathrm{Ri}_{min_H}$) there are close to zero and no changes in flow stability (i.e. Ri_{min} category) are observed in the transition from hydrostatic to non-hydrostatic mountain waves. This can be interpreted as resulting from a balance between the two mechanisms acting to decrease (dispersion) or enhance (orography slope) the wave amplitude, as described above.

4.4 Summary and conclusions

In this chapter, flow stability in the transition from hydrostatic to non-hydrostatic gravity waves generated over a narrow axisymmetric mountain in the presence of directional wind shear has been investigated. In particular, the analysis focused on understanding how non-hydrostatic effects can prevent or favour wave breaking relative to hydrostatic flow. A set of numerical simulations were performed extending the work presented in chapter 3, where the conditions for mountain wave breaking were diagnosed as a function of the orography elevation and wind shear, quantified by the dimensionless mountain height N_0H/U and the Richardson number of the background flow Ri_{in}, respectively. The orographic gravity waves considered in this study are sufficiently affected by non-hydrostatic effects ($N_0a/U = O(1)$) for dispersion and horizontal propagation to become important, but still too far from the strongly non-hydrostatic limit ($N_0a/U \ll 1$) for vertical propagation to be strongly inhibited.

The main conclusions from this chapter can be summarized as follows:

- For weaker shear flows, non-hydrostatic effects increase the stability of the flow. This is a consequence of the additional wave dispersion occurring in this case, which acts to decrease the wave amplitude when waves travel over long distances in the vertical before they reach a critical level and break.
- For stronger shear flows, non-hydrostatic effects decrease the stability of the flow. Here, dispersion effects are weaker because waves only propagate over short vertical distances before breaking, and additional instability seems to be caused primarily by the higher slope of the orography.
- The transition from stabilizing to de-stabilizing non-hydrostatic effects occurs gradually, and appears to be a function of the intensity of the directional shear of the background flow, perhaps because this controls the distance over which dispersion effects can act before the waves break.

In summary, although because of their dispersive nature non-hydrostatic mountain waves are generally believed to be less likely to break (Laprise and Peltier, 1989), in the presence of directional wind shear this seems to be only partially true. In the numerical simulations presented in this study, flow overturning was detected over lower mountains ($N_0H/U = 0.2$, or $H = 200$ m) than in the hydrostatic wave case, where the lowest N_0H/U value associated with wave breaking was 0.5, or $H = 500$ m (see section 3.3.2 and Figure 3.3). Admittedly, a more comprehensive exploration of parameter space would be necessary to ascertain the robustness of this finding.

The present results could be relevant to improve mountain wave breaking and turbulence diagnostics, for example, used in Clear-Air Turbulence forecasts for aviation.

Chapter 5

Mountain wave turbulence in the presence of directional wind shear over the Rocky Mountains

In this chapter, the role of directional wind shear in causing a real turbulence encounter over the Rocky Mountains, in the state of Colorado, is investigated. Pilot Reports (PIREPs) are used to select cases in which moderate or severe turbulence encounters were reported in combination with significant directional wind shear in the upstream sounding from Grand Junction, CO (GJT). For a selected case, semi-idealized numerical simulations are carried out using the WRF-ARW atmospheric model, initialized with the GJT atmospheric sounding and the real orography profile. Critical levels induced by directional shear are studied by taking 2D power spectra of the magnitude of the horizontal velocity perturbation field. In these spectra, a rotation of the most energetic wave modes with the background wind can be found. Such behaviour is consistent with the mechanism expected to lead to wave breaking in directional shear flows.

The work presented in this chapter has been submitted to the *Journal of Atmospheric Sciences*, with the reference:
Guarino MV, Teixeira MAC, Keller TL, Sharman RD, 2017. Mountain wave turbulence in the presence of directional wind shear over the Rocky Mountains. J. Atmos. Sci. - Status of the paper: under review.

In Appendix 5.A, additional discussion about the power spectra of the waves is provided.

5.1 Introduction

Mountain waves, also known as orographic gravity waves, result from stably stratified airflow over orography. These waves can break at different altitudes and influence the atmosphere both locally, by generating, for example, aviation-scale turbulence (Lilly, 1978), and globally, by decelerating the general atmospheric circulation (Lilly and Kennedy, 1973). Several studies have investigated the role of mountain wave activity in a wide range of atmospheric processes taking place in the boundary layer (e.g. Durran (1990), Grubišić *et al.* (2015)), in the mid-troposphere (e.g. Jiang and Doyle (2004), Strauss *et al.* (2015)), in the upper-troposphere (e.g. Worthington (1998), Whiteway *et al.* (2003), McHugh and Sharman (2013)), in the stratosphere (e.g. Carslaw *et al.* (1998), Eckermann *et al.* (2006)), and in the mesosphere (e.g. Broutman *et al.* (2017)).

Orographic gravity wave breaking in the mid- and upper-troposphere can generate turbulence at aircraft-cruising altitudes. This is one of the known forms of Clear-Air Turbulence (CAT), and it occurs, among other occasions, when large amplitude waves approach critical levels, as this leads to a further increase of the wave amplitude. Critical levels correspond to singularities in the wave equation, for which the wave motion is no longer sustained. Above the critical level height, waves cease to propagate, and break or are absorbed into the mean flow (Dörnbrack *et al.* (1995), Grubišić and Smolarkiewicz (1997)), provided the Richardson number of the background flow is larger than about 1 (Booker and Bretherton, 1967). For atmospheric flows where the wind direction changes with height, the existence of critical levels is controlled by the relative orientations of the background wind vector and the horizontal wave-number vector at each height. Broad (1995) and Shutts (1995) used linear theory to investigate the effects of directional wind shear on the gravity wave momentum fluxes, introducing the theoretical and mathematical framework for gravity wave drag in winds that turn with height.

Generally, mountain wave critical levels exist when $\mathbf{U} \cdot \boldsymbol{\kappa}_H = u_0 k + v_0 l = 0$ (where $\mathbf{U} \equiv (u_0, v_0)$ is the background wind velocity and $\boldsymbol{\kappa}_H \equiv (k, l)$ is the horizontal wave-number vector) (Teixeira, 2014). For unidirectional shear flows ($u_0 = f(z)$, $v_0 = 0$, where f is an arbitrary function) or flows over two-dimensional ridges ($l = 0$), the definition of critical level reduces to $u_0 = 0$. For directional shear flows ($u_0 = f(z)$, $v_0 = g(z)$, where f and g are arbitrary functions) over idealized three-dimensional or complex (i.e. realistic) orographies (where $k \neq 0$, $l \neq 0$), critical levels occur when the wind vector is perpendicular to the horizontal wave-number vector, as expressed by the general condition presented above. This condition is difficult to assess from

standard physical data, as the orientations of the wave-number vectors can only be evaluated in Fourier space.

Previous theoretical and numerical studies investigating mountain waves in directional shear flows include Shutts (1998) and Shutts and Gadian (1999), who studied the structure of the mountain wave field in the presence of directional wind shear; Teixeira *et al.* (2008), Teixeira and Miranda (2009) and Xu *et al.* (2012), who focused on the impact of directional shear on the mountain wave momentum flux and, thus, on the gravity wave drag exerted on the atmosphere. All these studies considered idealized situations with a wind direction that turns continuously with height. This flow configuration is the simplest possible with directional shear, and represents a prototype of more realistic flows.

We are aware of only two observational studies of this problem in the literature focused on real cases: Doyle and Jiang (2006) studied a wave breaking event in the presence of directional shear observed over the French Alps during the Mesoscale Alpine Programme (MAP). Lane *et al.* (2009), on the other hand, studied aircraft turbulence encounters over Greenland, and attributed the observed generation of flow instabilities to the interaction between mountain waves and directional critical levels.

In this chapter, mountain wave turbulence occurring in the presence of directional wind shear over the Rocky Mountains in Colorado is investigated. Numerical simulations for a selected turbulence encounter are performed using a semi-idealized approach, for which the WRF-ARW atmospheric model is used in an idealized configuration, but initialized with the real (albeit truncated) orography and a realistic atmospheric profile. This method allows us to retain the elements necessary to reproduce the mechanisms responsible for mountain wave generation and breaking, while working in simplified conditions that facilitate physical interpretation. The simulation results are compared with theory and with idealized simulations, for a more comprehensive description and better physical understanding of the flow. The aim is to isolate the role of directional shear and determine its relevance in causing the observed turbulence event.

Because of its complexity, the wave breaking mechanism in directional shear flows is not currently taken into account for CAT forecasting purposes. Investigating its role in real turbulence encounters, as this study aims to do, is part of the fundamental research needed to improve the forecasting methods of mountain wave turbulence, which is currently one of the most poorly predicted forms of CAT (Gill and Stirling, 2013). In fact, although mountain wave turbulence is included in the forecasts provided by the London World Area Forecast Centre (WAFC), its prediction is still based on a

method developed by Turner (1999), relying on diagnostics of the gravity wave drag from its parametrization in a global model (which itself does not accurately represent mountain wave absorption by directional shear). The turbulence forecasting system GTG, described in Sharman and Pearson (2016) also contains several explicit MWT algorithms, but none consider the effect of directional wind shear. Furthermore, a predictor for mountain wave CAT is absent in the forecast issued by the Washington WAFC (Gill, 2014).

The remainder of the chapter is organized as follows. In section 5.2, the mechanism leading to wave breaking in directional shear flows is discussed. In section 5.3, the methodology used to select the turbulence encounter investigated here and the set-up of the numerical simulations is presented. In section 5.4, the simulation results are described, and further discussed in the light of the sensitivity tests presented in the same section. In section 5.5, the main conclusions of the chapter are summarized.

5.2 Wave breaking mechanism in directional shear flows

For a hydrostatic, adiabatic, three-dimensional and frictionless flow without rotation, under the Boussinesq approximation the wave equation from linear theory (also known as Taylor-Goldstein equation) takes the form (Nappo, 2012):

$$\widehat{w}'' + \left[\frac{(k^2+l^2)N_0^2}{(ku_0+lv_0)^2} - \frac{ku_0''+lv_0''}{ku_0+lv_0}\right]\widehat{w} = 0, \tag{5.1}$$

where $\widehat{w}$ is the Fourier transform of the vertical velocity, N_0 is the Brunt-Väisälä frequency of the background flow, and the primes denote differentiation with respect to z.

In vertically sheared background flows, the solution to (5.1) can be approximated as (Teixeira *et al.*, 2004):

$$\widehat{w}(k,l,z) = \widehat{w}(k,l,0)\left|\frac{m(z=0)}{m(z)}\right|^{1/2} \mathrm{e}^{\,i\int_0^z m(z)\mathrm{d}z}, \tag{5.2}$$

where the bottom boundary condition is $\widehat{w}(k,l,0) = i(ku_0+lv_0)\widehat{h}(k,l)$, and $\widehat{h}(k,l)$ is the Fourier transform of the terrain elevation $h(x,y)$. This corresponds to a first-order

WKB approximation, where the vertical wave-number m is defined as:

$$m = \frac{N_0(k^2 + l^2)^{1/2}}{(ku_0 + lv_0)} \tag{5.3}$$

as if N_0, u_0 and v_0 were constant, but where these quantities depend on z. Equations (5.2)-(5.3) are valid for any wave-number vector (k, l) in the wave spectrum, as long as the background state variables N_0 and (u_0, v_0) vary sufficiently slowly with height. In addition, by mass conservation, it can be shown that the Fourier transforms of the horizontal velocity perturbations $\widehat{u'}$ and $\widehat{v'}$ are

$$\widehat{u'}(k,l,z) = \widehat{u'}(k,l,0)\text{sign}\left(\frac{m(z)}{m(0)}\right)\left|\frac{m(z)}{m(0)}\right|^{1/2} \mathrm{e}^{\,i\int_0^z m(z)\mathrm{d}z}, \tag{5.4}$$

$$\widehat{v'}(k,l,z) = \widehat{v'}(k,l,0)\text{sign}\left(\frac{m(z)}{m(0)}\right)\left|\frac{m(z)}{m(0)}\right|^{1/2} \mathrm{e}^{\,i\int_0^z m(z)\mathrm{d}z}. \tag{5.5}$$

Orographic gravity waves excited by an isolated or complex orography can always be represented by a spectrum of wave-numbers, whose direction and amplitude depend on the bottom boundary condition (as shown by (5.2)). Hence, the wave equation has to be solved for each wave-number and, in physical space, the resulting wave pattern will be given by the Fourier integral (or sum) of their contributions (Nappo, 2012).

From the equations shown above it can be seen that, in directional shear flows, the mountain wave equation (5.1) becomes singular at critical levels, where $\boldsymbol{\kappa}_H \cdot \mathbf{U} = ku_0 + lv_0 = 0$. For a wave-number approaching its critical level, m approaches infinity according to (5.3), and the Fourier transform of the vertical velocity $\widehat{w}$ becomes small ($\widehat{w} \to 0$) according to (5.2). On the other hand, according to (5.4)-(5.5), the Fourier transform of the horizontal velocity perturbation diverges ($(\widehat{u'}, \widehat{v'}) \to \infty$) (Shutts, 1998). The net result is an increase of the wave amplitude in the vicinity of a critical level. However, only wave-numbers with large spectral amplitudes approaching critical levels will in practice contribute to wave breaking (since this process is intrinsically defined in physical space) and the subsequent generation of turbulence; small amplitude wave-numbers will be absorbed at the critical levels, as described by linear theory (Booker and Bretherton, 1967). Note also that the products of $\widehat{u'}$ and $\widehat{w}$, and of $\widehat{v'}$ and $\widehat{w}$, remain finite near critical levels (as shown by (5.2),(5.4)-(5.5), despite the divergence of $\widehat{u'}$ and $\widehat{v'}$, since their amplification cancels out with the attenuation of $\widehat{w}$. These products would in fact be exactly constant with height if there were no singularities in the integrals in the exponents of (5.2) and (5.4)-(5.5), which account for the absorbing effect of critical levels (cf. Broad (1995)).

The diagnosis of critical levels induced by directional shear can only be made in

Fourier space (where the orientation and the amplitude of each wave-number may be determined), as explained above, but it is the wave energy distribution by wave-number in the wave spectrum that ultimately determines whether wave breaking occurs or not.

5.3 Methodology

5.3.1 PIREPs and case study selection

Pilot Reports (PIREPs) of turbulence were used to select cases where atmospheric turbulence was reported, in the presence of directional wind shear, over the Rocky Mountains. An accurate description of the PIREPs database used here is provided by Wolff and Sharman (2008). In the same paper, those authors discuss generic issues and limitations of using pilot reports as a research tool (see also Schwartz (1996)). Here, we recall that while PIREPs represent a reliable method to determine turbulence occurrence, the information they provide about time, location and turbulence intensity may not be accurate. More specifically, Sharman *et al.* (2006) showed that, on average, the uncertainty associated with pilot reports is 50 km along the horizontal direction, 200 s in time, and 70 m along the vertical direction. Despite this uncertainty, pilot reports have been conveniently employed in studies aimed at evaluating/validating turbulence occurrence under certain atmospheric conditions (Kim and Chun (2010), Trier *et al.* (2012), Ágústsson and Ólafsson (2014), Keller *et al.* (2015)), for lack of a better alternative.

In this study, PIREPs are used to identify days where generic atmospheric turbulence, or mountain wave turbulence (MWT), was reported by pilots over the Rocky Mountains in the state of Colorado. In particular, moderate or severe turbulence reports within the upper troposphere (4 km to the tropopause height) were considered. The first 4 km of the atmosphere were excluded to eliminate low-level turbulence and directional wind shear associated with boundary layer processes. Note that the highest mountain peak considered here has about 4 km elevation, and the boundary layer height over mountainous terrain is expected to adjust to the terrain elevation (DeWekker and Kossmann, 2015).

The analysis focused on the winter seasons of two years of data: 2015 and 2016. Climatologies of mountain wave activity (Julian and Julian (1969),Wolff and Sharman (2008)) show that this activity is larger over the Rocky Mountains during the winter months, when low-level winds are strong and westerly (i.e. perpendicular to the

dominant mountain ridges). Furthermore, the stronger jet stream in winter favours the existence of both speed and directional shear via the thermal wind relation. The atmospheric conditions were evaluated using soundings measured upstream of the Rocky Mountains. The meteorological station selected was Grand Junction (Figure 5.1), and the data were downloaded from the website of the University of Wyoming.

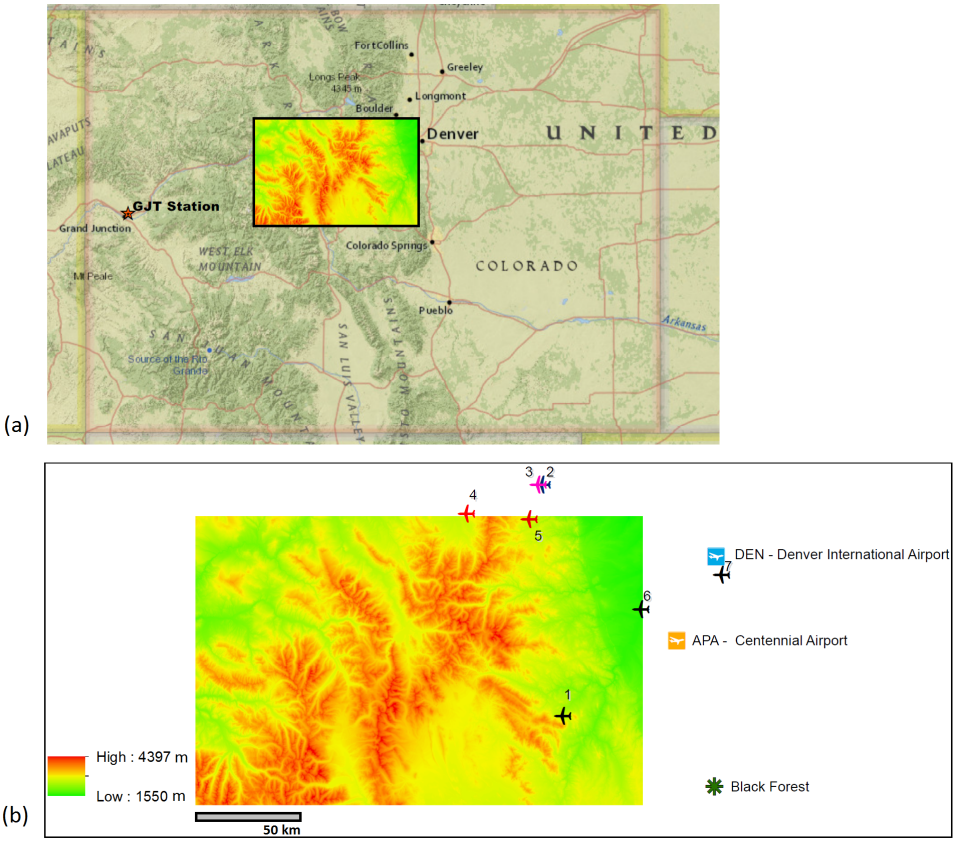

FIGURE 5.1: (a) Map of the study area showing the Rocky Mountains in the State of Colorado (USA) and the location of the Grand Junction meteorological station (GJT). The highlighted rectangular area corresponds to the portion of the Rocky Mountains used as lower boundary condition for the semi-idealized runs. (b) location of the turbulence reports possibly related to the atmospheric conditions present on 7th February 2015 00 UTC, as described in Table 5.1, and surrounding landmarks. The numbered aircraft symbols correspond to the turbulence reports ID in Table 5.1, the different colors are: black for ModT, red for SevT, blue for ModMWT, pink for SevMWT. The map only shows the portion of the Rocky Mountains used in the semi-idealized runs.

In Figure 5.2 the wind speed and direction, as well as the atmospheric stability (quantified through the squared Brunt-Väisälä frequency N^2) are shown for 7th February 2015 at 00 UTC. This day was chosen as a case study because of the fairly continuous change of wind direction with height and a tropopause height of about 11 km. The

existence of a high tropopause facilitates excluding the stability change with height taking place in its vicinity from the possible mechanisms causing wave breaking and, thus, responsible for the turbulence encounters reported in the first 10 km of the atmosphere (further indications that this is plausible are given below). As can be seen in Figure 5.2, the rate of wind turning with height is not constant but varies from a maximum of 50 degrees/km at lower levels (up to 4 km) and 10 degrees/km at higher altitudes (6 - 8 km), to a slower rotation rate (between 3 degrees/km and 5 degrees/km) in the atmospheric layers between 4 and 6 km and above 10 km respectively.

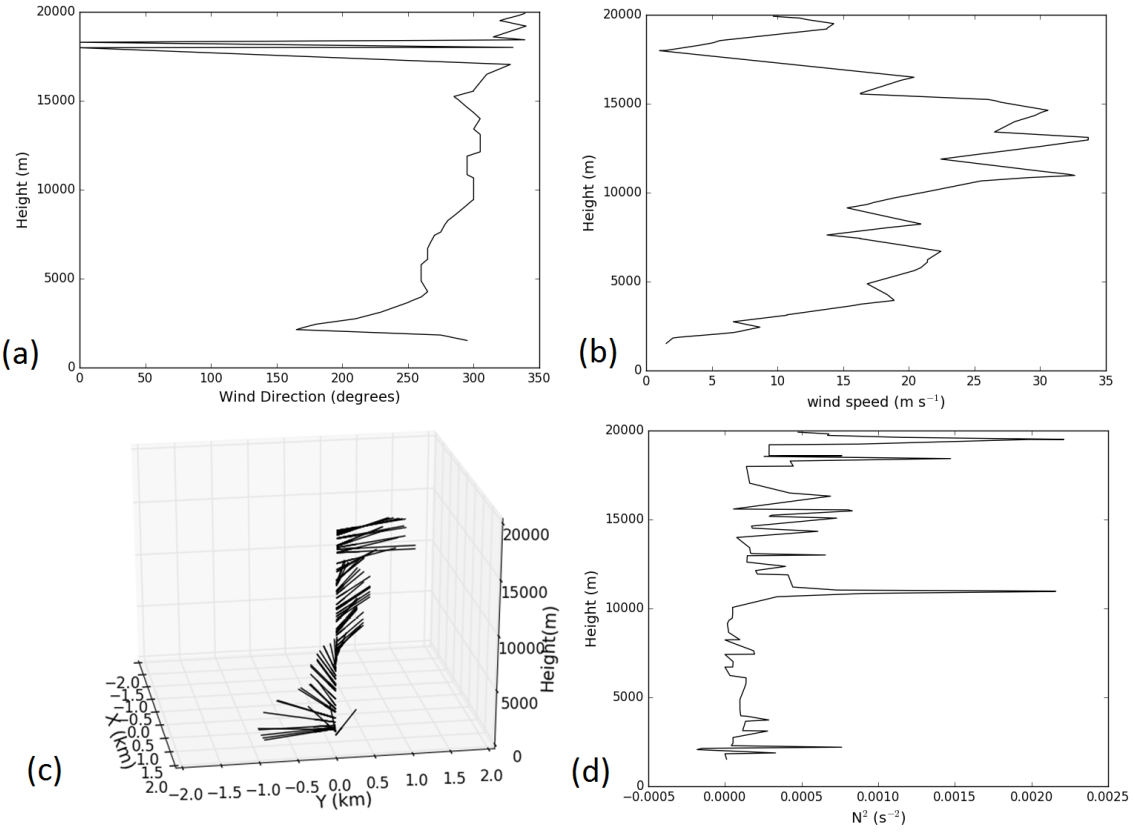

FIGURE 5.2: Variation of the wind direction (a), wind speed (b) and the squared Brunt-Väisälä frequency N^2 (d) with height for 7th February 2015 00 UTC. The meteorological data come from the Grand Junction station, located upstream of the Rocky Mountains (station elevation: 1475 m) (see Figure 5.1). (c) shows again the variation of the wind direction with height, but uses vectors with a constant length to represent the turning wind profile. Note that the vectors point towards the vertical axis in the middle.

Figure 5.1(b) shows the location of the turbulence reports associated with the atmospheric conditions presented in Figure 5.2, these reports were issued between 2 hours

before and 1 hour after 00 UTC of 7th February 2015. Table 5.1 provides details about the turbulence encounters such as type, altitude, time of occurrence, intensity of the turbulence, and the cubic root of the eddy dissipation rate ($\varepsilon^{1/3}$ – a standard measure of CAT) estimated from on-board data. ε provides a direct measure of turbulence intensity in the atmosphere, as informs us on the rate at which turbulence is dissipated by molecular viscosity. It is universally used for turbulence forecasting/nowcasting purposes because is relatively simple to calculate. Further, ε is an aircraft-independent metric of turbulence, unlike other possible metrics (for example, the root mean square of the vertical acceleration of an aircraft) that provide subjective information on the aircraft response to turbulence (see Sharman *et al.* (2014) for a more detailed discussion).

TABLE 5.1: Details about the turbulence reports, namely: type (moderate or severe turbulence (ModT, SevT), moderate or severe mountain wave turbulence (ModMWT, SevMWT)), time, altitude, and intensity of the turbulence, and the cubic root of the eddy dissipation rate ($\varepsilon^{1/3}$).

ID	Type of turbulence	Date and UTC time	Altitude (feet)	Altitude (meters)	$\varepsilon^{1/3}$ ($m^{2/3}$ s^{-1})
1	ModT	06 Feb 2015, 22.41	24000	7315	0.50
2	ModMWT	06 Feb 2015, 22.57	22000	6705	0.50
3	SevMWT	06 Feb 2015, 22.59	24000	7315	0.62
4	SevT	06 Feb 2015, 23.47	24000	7315	0.75
5	SevT	07 Feb 2015, 01.15	16000	4876	0.75
6	ModT	07 Feb 2015, 01.15	13000	3962	0.50
7	ModT	07 Feb 2015, 01.15	20000	6096	0.50

5.3.2 Numerical simulations

The selected day was investigated by performing semi-idealized numerical simulations using the WRF-ARW atmospheric model (Skamarock and Klemp, 2008). In this study, by "semi-idealized simulations" we mean simulations performed by running the WRF model in an idealized set-up, but using as input data real orography (truncated as explained next) and a real atmospheric profile. The simulations used the model's dynamical core only (i.e. no parametrizations), and the flow was assumed to be inviscid (no explicit diffusion and no planetary boundary layer) and adiabatic (no heat or moisture fluxes from the surface). Furthermore, the Coriolis force was

neglected (this choice is justified below). An isotropic horizontal grid spacing of $\Delta x = \Delta y = 1$ km was used, and the model's vertical grid comprised 100 stretched eta levels corresponding to (approximately) equally-spaced $z-$levels ($\Delta z = 250$ m). The top of the model domain was at 25 km, and a 7 km-deep Rayleigh damping layer was used to control wave reflection from the upper boundary.

The model was initialized using the wind profile and the atmospheric stability profile shown in Figure 5.2. A portion of the Rocky Mountains range (the rectangular area in Figure 5.1), downstream of the Grand Junction meteorological station (for the predominant flow direction), with a (zonal) length of 223 km and a (meridional) width of 144 km was chosen as the lower boundary condition. The terrain elevation data come from the U.S. Geological Survey 1 arc-second resolution national elevation dataset (NED), resampled to 1 km.

This real orography was placed approximately in the middle of the computational domain in order to avoid steep terrain at the lateral boundaries. The total size of the simulation domain is 400×400 km. Although by choosing such a large mountainous region as a forcing the effects of the Coriolis force on the dynamics of mountain waves may become important ($af/U \gtrsim 1$, where a is a characteristic mountain half-width, f is the Coriolis parameter and U is a velocity scale for the background wind), in this study rotation effects are neglected (by imposing $f = 0$). The ambiguous definition of mountain width in this case with complex terrain makes the af/U parameter difficult to estimate. af/U is much less than 1 if calculated taking into account a typical value for the width of single peaks in the mountain range (i.e. a =10 km, following Doyle *et al.* (2000)), but on the contrary, is large and greater than 1 if calculated by considering the mountainous region as a whole (i.e. $a \approx$100 km).

In order to assess to what extent the presence of the Earth's rotation can influence the generation and propagation of mountain waves, a simulation in which the Coriolis force was allowed to act on the flow perturbations (but not on the background flow) was run. This simulation set-up allowed us to focus on the differences due to rotation effects on the mountain waves only. Although some discrepancies were found between the two experiments with and without rotation, the overall flow pattern and, most importantly, the location of flow instability regions was only marginally affected. This in principle means that for our purposes the effect of the small-scale individual mountains is dominant, and that for the semi-idealized simulations presented here rotation effects are nearly negligible.

The model set-up described above was used for all performed simulations, including the sensitivity tests presented in the next section. Variations made to this initial configuration for each sensitivity test (i.e. changes in the orography, wind and stability profiles) will be described in the results section that follows.

5.4 Results and discussion

5.4.1 Semi-idealized simulations: real atmospheric sounding and orography

Instabilities generated within the computational domain were detected by looking at fields such as the potential temperature, the magnitude of the wave horizontal velocity perturbation vector (u', v'), and the Richardson number of the total flow including the wave perturbation, Ri_{out}. Note that since the simulations are inviscid, and thus no turbulence parametrizations are used, Ri_{out} values of less than 0.25 and/or zero are used to detect dynamical ($\mathrm{Ri}_{out} < 0.25$) and convective ($\mathrm{Ri}_{out} < 0$) instability regions that can potentially evolve into turbulence.

Figure 5.3(a) shows the grid points in the computational domain where Ri_{out} is lower than 0.25. The $\mathrm{Ri}_{out} \leq 0.25$ field was computed between 4 and 18 km, which corresponds (approximately) to the region between the height of the highest mountain peak and the height of the sponge layer employed in the simulations. The first 4 km of the atmosphere were excluded from the analysis because of unrealistic atmosphere-ground interactions that develop in frictionless simulations, leading to low Ri values just above the ground (see section 3.2.2). As shown in Figure 5.3(a), low Ri values occur just above the mountain peaks (in relation, perhaps, to the aforementioned atmosphere-ground interactions), between 6.5 and 10 km, and between 15 and 18 km height. While the highest-level instabilities occur in the stratosphere and therefore no pilot reports are available for validation purposes (aircraft cruise altitudes are usually up to about 12 km), the region of low Ri values located between 6.5 km and 10 km shows good agreement with the PIREPs database. Indeed, most of the turbulence reports indicate turbulence occurrence between 6 km and 7.5 km (see Table 5.1).

In Figure 5.4(a) contours of negative values of Ri_{out} (indicating flow overturning) at $z \approx 7.5$ km are shown. The background field is the terrain elevation. It can be seen that the location of the wave breaking event between 6 km and 7.5 km heights, mentioned above, agrees well with the turbulence report number 1 marked in Figure 5.1(b) (ModT1 in Table 5.1), both in the vertical and horizontal directions.

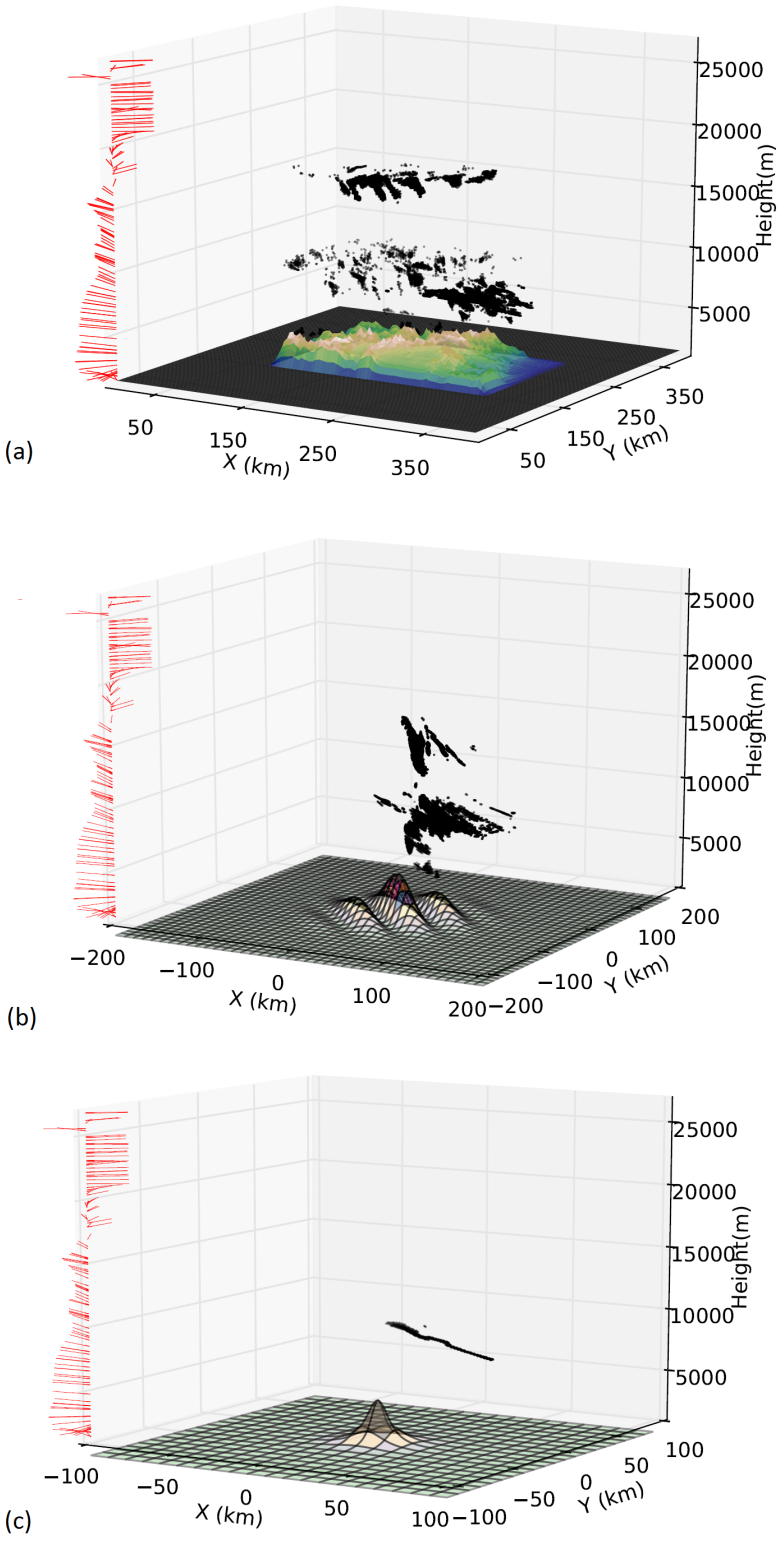

FIGURE 5.3: 3D plots showing every point in the computational domain where $\mathrm{Ri}_{out} \leqslant 0.25$ for the two simulations performed with a real input sounding and a real (a), an idealized mountain ridge (b), and a bell-shaped mountain (c) (Test 1). In (a) the Ri_{out} field contains flow overturning regions where $\mathrm{Ri}_{out} < 0$, and the simulation time shown is $t = 105$ min. In (b) and (c) the simulation time shown is $t = 360$ min, however in (c) the Ri_{out} field is never negative (at any simulation time).

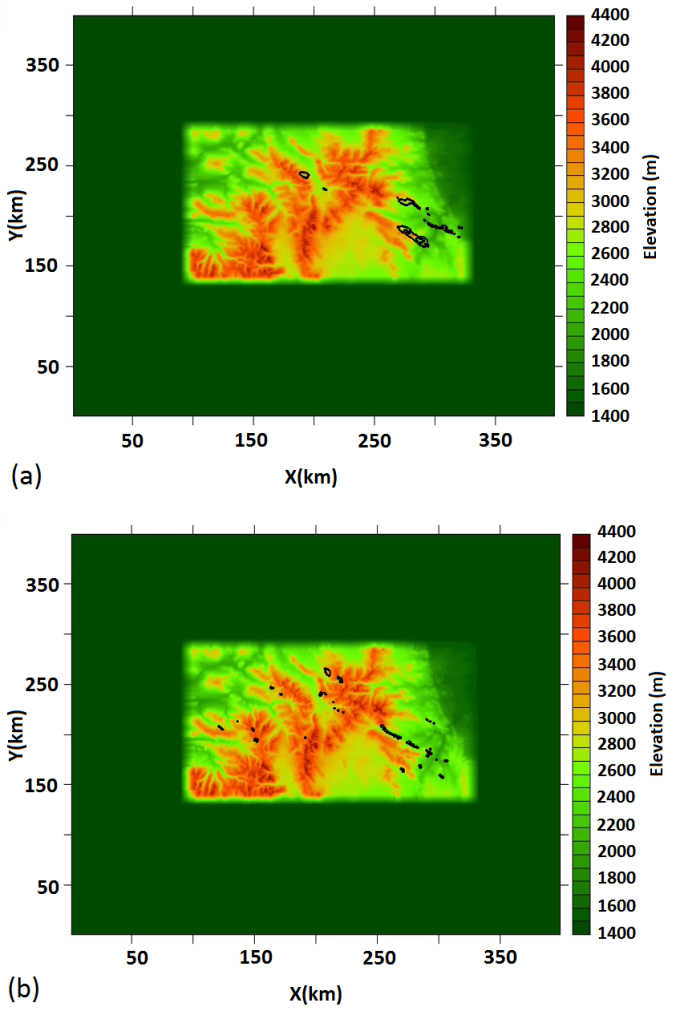

FIGURE 5.4: Horizontal cross-sections of the $\mathrm{Ri}_{out} < 0$ field at $z \approx 7.5$ km, at the simulation time $t = 105$ min. (a) uses the real input sounding containing both speed and directional shear; (b) uses the modified input sounding where only directional shear is present (Test 3). The background field is the terrain elevation.

In the following sub-sections, attention will be focused on analysing to what extent directional shear is primarily responsible for the wave breaking event displayed in Figure 5.4(a) (note that at different simulation times and at different locations we can observe more wave breaking events; however, there are no turbulence reports directly linkable to those events).

5.4.2 Sensitivity tests

Despite the simplicity of the semi-idealized simulations performed, wave breaking events detected in the simulation domain cannot be automatically associated to the presence of directional wind shear. Indeed, at least three other possible environmental

conditions able to modulate the gravity wave amplitude can be identified: 1. a sufficiently high or steep orography; 2. the variation of N with height, in particular at the tropopause; 3. the speed shear in the wind profile. Sensitivity tests were performed to investigate the role of each of these physical mechanisms separately.

Note that the unsteady nature of the flow in a wave breaking event makes comparisons between the simulations more difficult, since the evolution of two flows can be similar but asynchronous. The results presented next were analysed through the use of animations of the studied quantities over time, and the snap-shots presented in this study are representative of the overall flow features detected.

5.4.2.1 Test 1: the bottom boundary condition / surface forcing

The mechanism responsible for wave breaking in directional shear flows is sensitive to the bottom boundary condition (as shown by (5.2)), which may play a crucial role in the wave breaking process. We can hypothesize that orographies with different shapes, heights and orientations will excite waves with high energy at wave-numbers that have critical levels at different heights, or will interact with a given critical level (i.e. at a similar height) in a different way, depending on the spectral energy distribution (see section 2, or Chapter 3 for a more extended discussion).

In order to test the role of the lower boundary condition, two simulations with the same realistic input sounding presented in section 3 but idealized orographies were run. More specifically, the first sensitivity test was performed using an axisymmetric bell-shaped mountain given by:

$$h(x,y) = \frac{H}{\left(\frac{x^2}{a^2} + \frac{y^2}{a^2} + 1\right)^{3/2}} \tag{5.6}$$

where, following Doyle et al. (2000), the mountain height is $H = 2$ km and its half-width is $a = 10$ km, which are typical values for the Colorado Front Range (Doyle *et al.*, 2000). Note that unlike Doyle *et al.* (2000), who modelled the Rocky Mountains using an idealized 2D ridge, in this experiment a 3D mountain is adopted. While it could be argued that a two-dimensional representation of the Rocky Mountains could provide a more realistic approximation to their large-scale structure, here we are interested in how the smaller-scale structure, which is intrinsically 3D, affects wave breaking, via fulfilment of the $\mathbf{U} \cdot \boldsymbol{\kappa}_H = 0$ condition. In the case of a (perfect) 2D orography with $l = 0$ the definition of critical level reduces to the one valid in unidirectional flows. However, the realistic orography considered here will certainly

excite waves with wave-number vectors spanning various directions (i.e. $l \neq 0$), so use of a 3D idealized mountain is justified.

For the second sensitivity test, an idealized 3D mountain ridge containing a few peaks was used:

$$h(x,y) = H\mathrm{e}^{-\left[(x/a_{rdg})^2+(y/a_{rdg})^2\right]}[1+\cos(k_s x + l_s y)] \tag{5.7}$$

where the height of the highest peak in the mountain ridge is $H = 2$ km, the characteristic horizontal length-scale of the mountain ridge is $a_{rdg} = 50$ km and k_s and l_s, the horizontal wave-numbers of the smaller scale orography, have been chosen so that the half-width of each peak is about 10 km. The orography profile defined used the above parameters extends over an area of approximately 180X130 km, is oriented northwest-southeast and contains 5 peaks (see Figure 5.3(b)).

Although still drastically idealized, this orography approximates better the surface forcing imposed by the Rocky Mountains in terms of spatial extent (the fraction of the Rocky Mountains considered in this study extends over an area of about 220 × 150 km), the ridges' orientation (in particular of those peaks near which turbulence was observed, according to turbulence report number 1) and introduces a range of scales that attempts to (partially) reproduce the many smaller-scale features of the real orography. Using this approach, the interaction between different wave-numbers excited by the orography is probably taken into account.

In Figure 5.3(b) and (c) the $\mathrm{Ri}_{out} \leq 0.25$ field obtained for the two idealized orography simulations is shown and compared to that obtained for the real orography simulation (Figure 5.3(a)). When an isolated mountain is used (Figure 5.3(c)), despite the idealized simulation set-up, the model is able to reproduce the occurrence of dynamical instabilities at higher levels in the atmosphere, but it fails to predict the true location of the observed instability region. Indeed, most of the turbulence reports indicate turbulence between 6 km and 7.5 km (Table 1) while, in this simulation, instabilities take place in a thin layer between ≈ 9.3 km and 10 km. Furthermore, taking a closer look at the Ri_{out} field reveals that no negative Ri_{out} values exist, so no flow overturning due to wave breaking is taking place in the domain of simulation. However, when a mountain ridge with a few peaks is used (Figure 5.3(b)) the instability region is wider and more pronounced, contains negative Ri_{out} values and, most importantly, resembles better the flow simulated using the real orography (Figure 5.3(a)). Flow instabilities occur at lower levels (≈ 4 km), between 7.5 km and 11.5 km (providing a better agreement with the observations), and also at higher altitudes (≈ 14.5 – 16.5 km).

We can conclude that there is overall a poor agreement between these idealized simulations and the PIREPs, but significant improvements were observed when an orography profile with a few peaks was considered. This is a consequence of the fact that, although we still retain some elements needed to generate mountain waves that may break in directional shear (namely: a stably stratified atmosphere, representative values of mountain height and width, and a wind direction that changes with height), the wave solution obviously depends on the Fourier transform of the terrain elevation $\widehat{h}(k,l)$ (see equation (5.2)). Hence, the energy associated to each wave-number excited at the surface is closely linked to the shape and orientation of the mountain profile. Consequently, the wave spectrum excited by an axisymmetric mountain, or an idealized mountain range, and by the realistic orography are quite different and the interaction between wave-numbers and directional critical levels differs accordingly.

5.4.2.2 Test 2: the tropopause and the variation of N with height

Previous studies (Worthington, 1998; Whiteway *et al.*, 2003; McHugh and Sharman, 2013) pointed out how the interaction between vertically propagating orographic waves and the tropopause may trigger wave breaking and thus high-level turbulence generation. Furthermore, inhomogeneities in the atmospheric stability can cause wave reflection (Queney, 1947) that, by constructive or destructive interferences between upward and downward propagating waves, can modulate the surface drag and the wave amplitude itself (Leutbecher, 2001).

Although the investigated turbulence encounter was reported at a height of about 7.3 km, and therefore it is quite distant from the tropopause (in Figure 5.2(c) a substantial increase in N^2 that may be identified as the tropopause occurs at about 11 km), a simulation without the tropopause, more specifically assuming a constant $N = 0.01s^{-1}$, was run. The aim of this simulation was to exclude as a possible cause for wave breaking the existence of significant wave reflections that could potentially take place not only due to the high value of N at the tropopause itself, but also due to the variation of N within the troposphere. This latter effect might also lead to substantial modulation of the wave amplitude by refraction (according to (5.2),(5.4)-(5.5)).

In Figure 5.5 vertical (west-east) cross-sections of the magnitude of the wave horizontal velocity perturbation vector (u', v') are shown. The cross-sections pass through the grid-point where turbulence was reported (Y = 180 km in Figure 5.4(a)), and the black contours delimit the regions where Ri_{out} is negative. Figure 5(a) refers to the real sounding simulation and Figure 5.5(b) to the simulation with a constant N.

The studied wave breaking event, responsible for the negative Ri_{out} values between 6.5 and 10 km, is present in both simulations. Although in Figure 5.5(b) the instability regions are smaller, they present the same wake structure (discussed later in this section) visible in Figure 5.5(a) where patches of negative Ri_{out} propagate downstream. Also, at the same height, the (u', v') magnitude has a very similar pattern (and magnitude) in both flows.

This result indicates that wave reflection is probably not significant enough to cause wave breaking. However, the large stability jump at the tropopause cannot be ignored, and wave reflection is still expected to happen to some degree. An estimation of how much reflection should be expected for the stability profile in Fig. 2(b) can be obtained by calculating the reflection coefficient $R = (N_2 - N_1/N_2 + N_1)$, proposed by Leutbecher (2001) (developed for 2D flow), where we omit the minus sign to make R positive. This expression for R is valid for waves travelling in layers with constant N_1 and N_2. Since in the sounding of Figure 5.2(b), N^2 varies substantially, the values of N_1 and N_2 adopted here must be understood as averages below and above the large N maximum that corresponds to the tropopause, respectively. Taking N_1 = 0.01 s^{-1} at z = 10 km and N_2 = 0.02 s^{-1} at z = 11.2 km, we note that these are quite typical values for the troposphere and stratosphere and correspond to R = 1/3. Therefore, we can expect that about one-third of the upward propagating mountain waves be reflected back at the tropopause. However, in order for this reflection to cause wave enhancement, the phase of the reflected wave must also be properly tuned. The N maximum at the tropopause should also lead to horizontally propagating waves trapped at that height (Teixeira *et al.*, 2017), but since those waves decay exponentially in the vertical, their effect at $z \approx 6 - 7\,\mathrm{km}$ should be relatively modest. Hence, consistent with Figure 5.5(b), these do not seem to be the dominant mechanisms causing wave breaking.

The analysis presented above suggests that the effects of the tropopause and of the N variation in general do not play an important role in causing the observed turbulence and, thus, are not of key relevance to the event under investigation.

5.4.2.3 Test 3: the speed shear

Alongside with the variation of N with height, the change of wind speed with height represents an additional factor able to modulate the amplitude of gravity waves (see (5.2), (5.4)-(5.5)). In particular, it is known (and consistent with (5.4)-(5.5)) that a decreasing wind speed with height represents the best condition for wave steepening (Smith (1977),McFarlane (1987), Sharman *et al.* (2012a)), which can facilitate the

breaking of already large-amplitude waves. As can be seen in Figure 5.2(b), overall, the speed shear is positive over most of the troposphere, where the wind speed tends to increase with height, however regions where the wind speed decreases with height are also present.

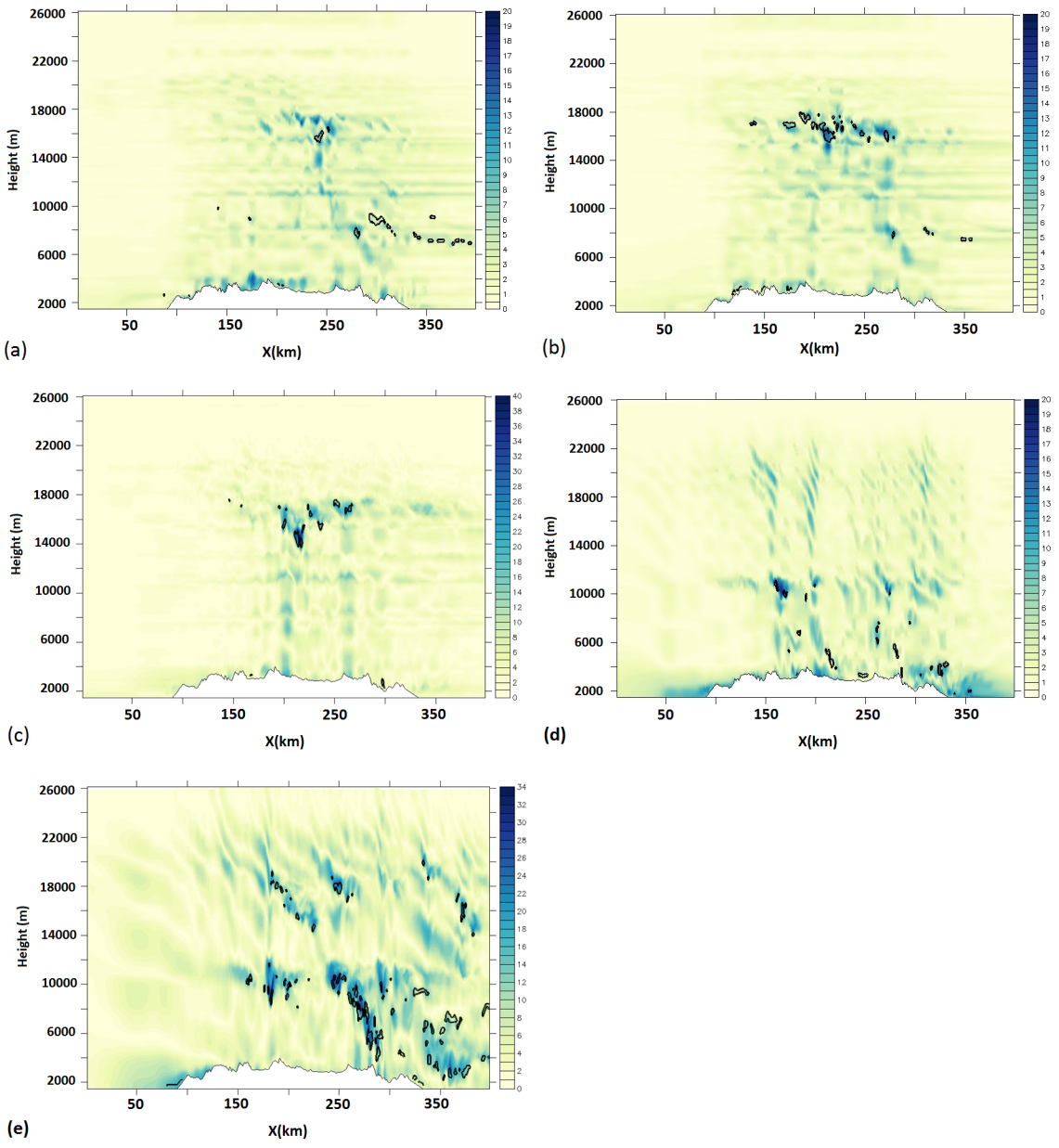

FIGURE 5.5: Vertical (west-east) cross-sections at Y = 180 km in Figure 5.4 comparing the real sounding simulation (a) with simulations run using a constant N (Test 2) (b), a constant wind direction and a varying wind speed (Test 3) (c), a constant direction and wind speed (Test 4) using U = 10 m s^{-1} in (d) and U = 20 m s^{-1} in (e), at the simulation time t = 180 min. The background field is the magnitude of the wave horizontal velocity perturbation vector (u', v'), the black contours delimit $\mathrm{Ri}_{out} < 0$ regions.

The speed shear contribution was eliminated by modifying the input wind profile so that the u and v components varied with height accounting only for the observed change in the wind direction, neglecting the variation due to the changes in wind speed, which was kept fixed at 10 m s^{-1}. The large wind speed variation for the specific day under consideration did not make it easy to identify a dominant wind speed. Indeed, while the wind speed of the flow crossing the mountain between 2.2 km and 3.6 km altitude varies in the range 7 m s^{-1} – 16 m s^{-1}, the wind speed over the mountain peaks is about 20 m s^{-1}. The value 10 m s^{-1} was chosen because it approximates better the wind speed at low levels, which is presumably responsible for generating the waves (see also Test 4, in the following section, where this assumption is furtherly tested).

In Figure 5.4(b) the $\mathrm{Ri}_{out} < 0$ field at $z \approx 7.5$ km for the new simulation including only directional shear is shown. Both in Figure 5.4(a) (the real sounding simulation) and 5.4(b) overturning regions with approximately the same location and having the same elongated shape are visible. Figure 5.6(a) and 5.6(b) show again contours of negative values of Ri_{out} in west-east vertical cross-sections passing through the point where turbulence was reported (Y = 180 km in Figure 5.4(a)). Figure 5.6(a) corresponds to the simulation with the real input sounding, Figure 5.6(c) to the simulation without speed shear. Figure 5.6(b) and 5.6(d) show the same comparison but for the potential temperature fields. From Figure 5.6 we can see that the wave breaking region occurs in the two simulations at similar altitudes (between 6 and 10 km).

Despite some differences between the two simulations (note that by modifying the input sounding we are modifying the background state in which waves are generated), the occurrence of wave breaking does not seem to be related to the presence of speed shear.

A second test was performed to furtherly assess the speed shear contribution to wave breaking. The input wind profile was again modified but this time the u and v components varied with height accounting only for the observed wind speed variation, and the directional shear was eliminated by using a constant wind direction (chosen as a "dominant wind direction" by looking at the atmospheric sounding in Figure 5.2(a)) equal to 260 degrees.

In Figure 5.5(a) and 5.5(c) vertical cross-sections for the real sounding simulation (a) and the speed shear only simulation (c) are shown. The background field is the magnitude of the horizontal velocity perturbation vector (u', v'), and the black contours delimit the region with $\mathrm{Ri}_{out} < 0$. In Figure 5.5(a) waves break at an altitude

of about 7 km, as discussed in section 5.4.1.

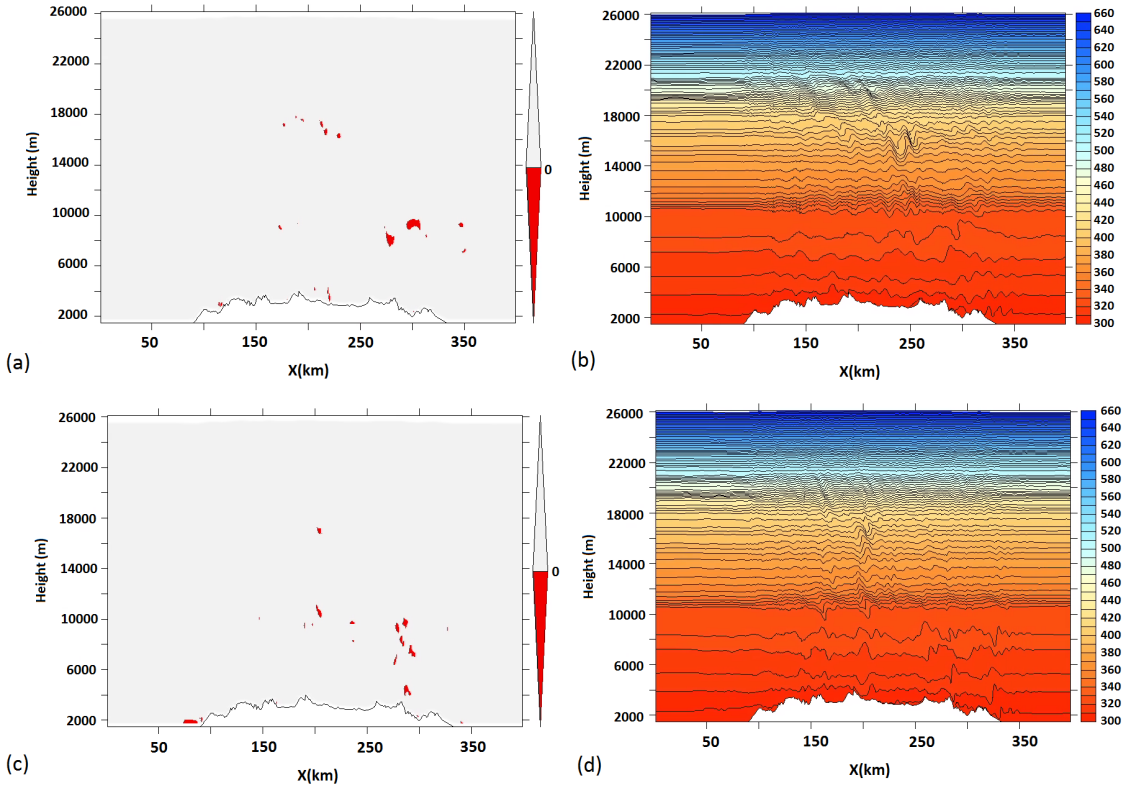

FIGURE 5.6: Vertical (west-east) cross-sections of regions where $\mathrm{Ri}_{out} < 0$ (a and c) and potential temperature (b and d) fields passing through the point where turbulence was reported (Y = 180 km in Figure 5.4) at the simulation time t = 135 min. (a) and (b) correspond to the simulation with the real input sounding. (c) and (d) correspond to the simulation where speed shear was neglected (Test 3).

When directional shear is removed (Figure 5.5(c)) no overturning regions where $\mathrm{Ri}_{out} < 0$ are observed within the troposphere (and lower stratosphere). However, in the speed shear only simulation, the breaking of the waves at z $\approx$ 15 km – 17 km is intensified and here the magnitude of the (u', v') vector increases up to 40 m s^{-1}.

The atmospheric sounding in Figure 5.2(b) shows a net decrease of the wind speed with height in the layer 14 km – 18 km. This significant negative wind shear is probably responsible for the high-altitude wave breaking. In the absence of directional shear, the filtering of the waves at lower levels is removed and all the wave-numbers in the wave-spectrum break at the same height. Thus, the wave energy is dissipated in a thin layer, rather than over the entire troposphere, resulting in the larger velocity perturbations observed in Figure 5.5(c).

5.4.2.4 Test 4: the mountain amplitude

An last test was necessary to corroborate our hypothesis that waves are breaking because of critical levels imposed by the variation of the wind direction with height, and not only because of a highly non-linear boundary condition such as is imposed by the Rocky Mountains. Indeed, for NH/U values larger than 1, linear theory breaks down and wave breaking is expected to occur even in unsheared flows (Huppert and Miles (1969), Smith (1980), Miranda and James (1992)).

For this purpose, simulations in which both wind speed and direction are kept constant were performed. In these simulations the wind direction was again set to 260 degrees and we used two different values of wind speed: U = 10 m s^{-1} and U = 20 m s^{-1}. As discussed in section 5.4.2.3, the choice of a representative wind speed of the flow passing over the orography is difficult because of the large variation of U in the lowest 3.5 km of the atmosphere. In the sensitivity tests presented here, 10 m s^{-1} was used because it was assumed to be representative of the flow at lower levels, while 20 m s^{-1} was used to test the robustness of this assumption and because this is the wind speed just above the highest mountain peaks.

Figure 5.5(d) compares the U = 10 m s^{-1} simulation with the real sounding simulation of Figure 5.5(a). While in Figure 5.5(a) the breaking region is again easily detected between 7 and 10 km, where patches of negative values of the Richardson number appear, for the simulation with a constant wind speed and direction (Figure 5.5(d)), the waves continue to propagate upwards without breaking at the same heights and horizontal locations.

This ability of the gravity waves to propagate to higher levels in the atmosphere supports the argument that, by removing the directional shear, we removed the mechanism responsible for wave breaking in the event under consideration (this test also directly compares with Test 3, Figure 5.4(b), where U = 10 m s^{-1} and directional shear is present). More specifically, without directional shear, the filtering of the wave energy by critical levels vanishes. Therefore, wave-numbers that would otherwise be absorbed into the mean flow, or increase their amplitude and cause wave breaking, remain essentially unaffected and keep on propagating upward.

In addition to vertically propagating gravity waves, in Figure 5.5(d), a few instability regions are also visible, but not at the correct levels. The mechanism behind these instabilities, and the associated wave breaking, can only be related to the high amplitude of the surface forcing provided by the Rocky Mountains, conjugated with the

decrease of density with height (which are the only possible wave breaking mechanisms active in this case).

When a U = 20 m s^{-1} is used (Figure 5.5(e)), large amplitude gravity waves are excited by the Rocky Mountains that break vigorously (the maximum on the $|(u'v')|$ scale is 34 m s^{-1}) at lower and higher atmospheric levels.

The opposite flow behaviour observed in the two tests is a consequence of the transition between two, well known, different flow regimes. Assuming $N = 0.01$ s^{-1} and $H = 2$ km, which is a good estimate of the mountain height as seen by the incoming flow (the GJ station used to initialize the model is located at about 1.5 km a.s.l.), $NH/U = 2$ when U = 10 m s^{-1} and $NH/U = 1$ when U = 20 m s^{-1}. For a 3D orography, when $NH/U = 2$ the flow enters a "flow around" regime for which a significant part of the flow is deflected around the flanks of the obstacle and the generation of vertically propagating mountain waves is weakened. When $NH/U = 1$ most of the incoming flow passes over the orography and wave breaking is favoured (Miranda and James, 1992).

In reality, the amplitude of the waves excited by the Rocky Mountains will be the result of a varying wind speed, and not of a fixed U. Therefore, although the flow simulated using U = 10 m s^{-1} is closer to the one in Figure 5.5(a) in terms of magnitude of the velocity perturbation vector, the wave breaking found when U = 20 m s^{-1} suggests that effective wind speed of the flow approaching the mountain can be decisive in causing wave breaking. We conclude that it is not possible to exclude self-induced overturning from the possible wave breaking mechanisms. Instead, this mechanism is probably acting alongside the directional shear one (as discussed in more details in the following section).

5.4.3 The directional shear contribution

While Tests 2, 3 and 4 investigated the role of static stability, speed shear and mountain height in causing the studied turbulence encounter, in this section more direct evidence that waves may break because of environmental critical levels associated with the presence of the directional shear will be presented and discussed.

Both in the horizontal cross-section of Figure 5.4 and in the vertical cross-section of Figure 5.5(a), the region delimited by the $\mathrm{Ri}_{out} < 0$ contour exhibits an elongated shape that, departing from the first wave breaking point, extends downstream forming a certain (small) angle with the wind direction (which is very close to 270 degrees) at that height.

This downwind transport of statically unstable air seems to be a signature of breaking waves in directional shear flows. Based on linear theory arguments, Shutts (1998) demonstrated the existence of a flow feature known as "asymptotic wake" (see also Shutts and Gadian (1999)). The asymptotic wake is a consequence of wave-numbers approaching critical levels in directional shear flows and, more precisely, of a component of the background wind parallel to the wave phase lines that will advect the wave energy away from the mountain (in stationary conditions).

The asymptotic wake predicted by Shutts translates into lobes of maximum wave velocity perturbation extending along the wind direction at each height, but not perfectly aligned with it (Figure 5.7(a)). We hypothesize that the tail of negative Ri values in Figure 5.4 and Figure 5.5(a), which is absent in all the breaking regions in Test 4 (see for example Figure 5.5(d)), is a manifestation of the asymptotic wake predicted by Shutts (1998). In Figure 5.7 the magnitude of the horizontal velocity perturbation vector (u', v') is shown for 5 different cases:

- Figure 5.7(a) and 5.7(b) show the flow behaviour for orographic waves excited by an axisymmetric mountain (as described by (5.6)) in the case of a background wind direction that changes (backs) continuously with height (rate of rotation $\approx$ 14 degrees/km), a constant $N = 0.01$ s^{-1} and wind speed $U = 10$ m s^{-1}. In Figure 5.7(a) the analytical solution obtained by running a linear model for such a flow is shown, in Figure 5.7(b) the corresponding idealized numerical simulation (with $H = 1$ km) is presented. The numerical set-up for this idealized simulation is slightly different from the one presented in section 5.3 (see Chapter 3 for further details).

- Figure 5.7(c) and 5.7(d) correspond to Test 1, therefore they depict simulations that use an idealized 3D orography (as described by (5.6)) and an idealized mountain ridge (as described by (5.7)) but a real atmospheric sounding.

- Figure 5.7(e) corresponds to the semi-idealized simulation that uses real orography and a real atmospheric sounding (more specifically, it focuses on a portion of the entire simulation domain shown in Figure 5.4(a), starting at X = 240 km, Y = 110 km).

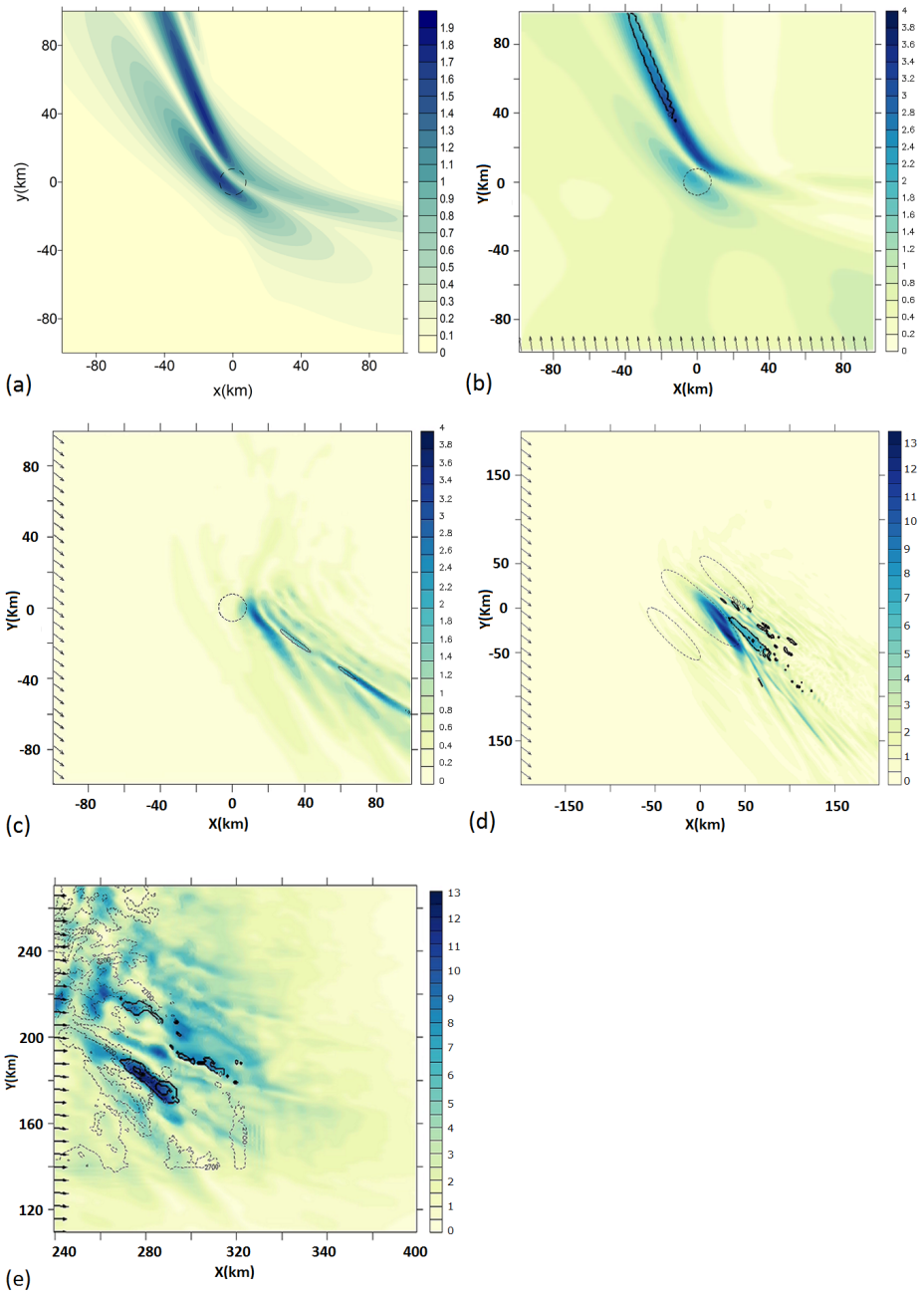

FIGURE 5.7: Horizontal cross-sections showing the flow transition as the degree of realism increases. The background field is the magnitude of the (u', v') vector, the dashed contours mark the bottom orography. In (b)-(e) the arrows are the background wind at the displayed level, the solid contour lines are $\mathrm{Ri}_{out} < 0$ (exept for (c) where $0 < \mathrm{Ri}_{out} \leq 0.25$). (a) analytical solution from linear theory and (b) equivalent cross-section taken at $z \approx$7 km for a simulation with idealized orography and an idealized atmospheric sounding; (c) cross-section taken at $z \approx$9.5 km for a simulation with idealized orography but a real atmospheric sounding (Test 1) at $t = 360$ min; (d) as (c) but for a simulation with an idealized mountain ridge containing a few peaks; (e) cross-section taken at $z \approx$7.5 km for the semi-idealized simulation with real orography and a real atmospheric sounding at $t = 105$ min. Note that (e) corresponds to a portion of the simulation domain shown in Figure 5.4(a), starting at X = 240 km, Y = 110 km.

The black contours are the lowest Ri_{out} values for each simulation. Note that although in Figure 5.7(a) and 5.7(b) the wind rotates counter-clockwise and in Figure 5.7(c), 5.7(d) and 5.7(e) it rotates clockwise, this only modifies the quadrants in which the wave energy is advected at different heights (and so where the maximum of the wave perturbation field is), but the two sets of results may be seen as essentially equivalent via a mirror transformation. The purpose of Figure 5.7 is to show the progressive transition of the asymptotic wake structure as the degree of realism of the flow increases. The asymmetry of the wave perturbation field is visible in both Figure 5.7(a) and 5.7(b), where the left-hand branch extends to the north-west, tending asymptotically to the wind direction at that height (this is the asymptotic wake). As we shift towards less idealized flows (Figure 5.7(c), 5.7(d) and 5.7(e)), this flow feature becomes less clear but it is still detectable (albeit mirrored).

Proving the existence of the asymptotic wake in real case studies is of a particular interest, since approximately hydrostatic mountain waves (such as the ones excited by the Rocky Mountains) are usually expected to break and cause turbulence just above the mountain peaks and not far downstream, but this is what seems to happen when an asymptotic wake is present (see in particular Figure 5.5(a)).

5.4.3.1 Spectral analysis of the wave field

A final piece of evidence supporting the importance of critical levels due to directional wind shear is provided by spectral analysis carried out on the magnitude of the (u', v') vector field. The quantity $|(u', v')|$ was chosen because of the strong amplification of the horizontal velocity perturbations at critical levels. This spectral analysis will be first presented for the the fully idealized simulation (with an idealized axisymmetric orography and idealized atmospheric sounding) introduced in the previous section, and then for the more realistic case being investigated.

In Figure 5.8[1] the 2D spatial power spectra of the horizontal velocity perturbation field, computed at different heights from the fully idealized simulation are shown. The five spectra correspond to $|(u', v')|$ horizontal cross-sections taken at 3 km, 6.1 km, 7 km, 10 km and 13 km heights, at a same simulation time. Note that Figure 5.8(c) is the 2D power spectrum of Figure 5.7(b).

Since the Fourier transform of a purely real signal is symmetric, in a 2D power spectrum all the information is contained in the first two quadrants of the (k, l) plane

[1]Note that in both Figure 5.8 and Figure 5.9, the non-zero spectral energies extending along the x and y axes correspond to numerical noise generated in the computation of the 2D power spectra.

and the third ($k < 0, l < 0$) and fourth ($k > 0, l < 0$) quadrants are just mirrored images of the first ($k > 0, l > 0$) and second ($k < 0, l > 0$) quadrants, respectively. The x- and y-axes show the wave-number components, and the black arrows show the background wind direction at the height where each spectrum was calculated.

For the idealized wind profile employed in this simulation, the continuous (and smooth) turning of the background wind vector with height creates a continuous distribution of critical levels in the vertical. At each critical level, the wave energy is absorbed into the background flow and this absorption affects one wave-number in the spectrum at a time (i.e., at each level). Looking at the power spectra in Figure 5.8, it can be seen that the dominant wave-number at each height (i.e. that with most energy) is the one perpendicular to the incoming wind (i.e. the one having a critical level at that height). As a consequence, the wave-number vector of the most energetic wave-mode rotates counter-clockwise following the background wind, but 90 degrees out of phase. It can also be seen that as the incoming wind rotates by a certain angle, the portion of the wave spectrum corresponding to wave-numbers perpendicular to the wind at lower levels has been absorbed. For example: in Figure 5.8(b) the wind is from the South, departing from a westerly surface direction, so all the wave-numbers in the second quadrant ($k < 0, l > 0$) have been absorbed. When the background wind has rotated by 180 degrees (Figure 5.8(e)) practically all the wave energy has been dissipated, because all possible critical levels have been encountered at lower altitudes (Teixeira and Miranda, 2009) (this is confirmed by flow cross-sections – not shown – where no waves exist above the height where the power spectrum in Figure 5.8(e) was computed).

It should be noted that the angle actually detected between the background wind direction and the most energetic wave-mode at each height is slightly less than 90 deg. A plausible interpretation is that, although a wave reaches its maximum amplitude at a critical level in linear theory, this is also the height where it will break. For finite-amplitude waves, amplification and breaking tends to occur some distance below critical levels. Therefore, typically, the energy carried by a wave-number vector perpendicular to the wind has already been absorbed, and so the angle between wavenumbers that still carry maximum energy (prior to breaking) and the local wind direction will be less than 90 degrees.

When similar 2D power spectra are computed for the more realistic case under consideration, significant similarities can be seen. In Figure 5.9 the 2D spatial power spectra computed from the semi-idealized numerical simulation are shown at heights comprising every kilometre of the atmosphere between 5.5km and 15.5 km. Figure 5.9(c) is the 2D power spectrum of Figure 5.7(e).

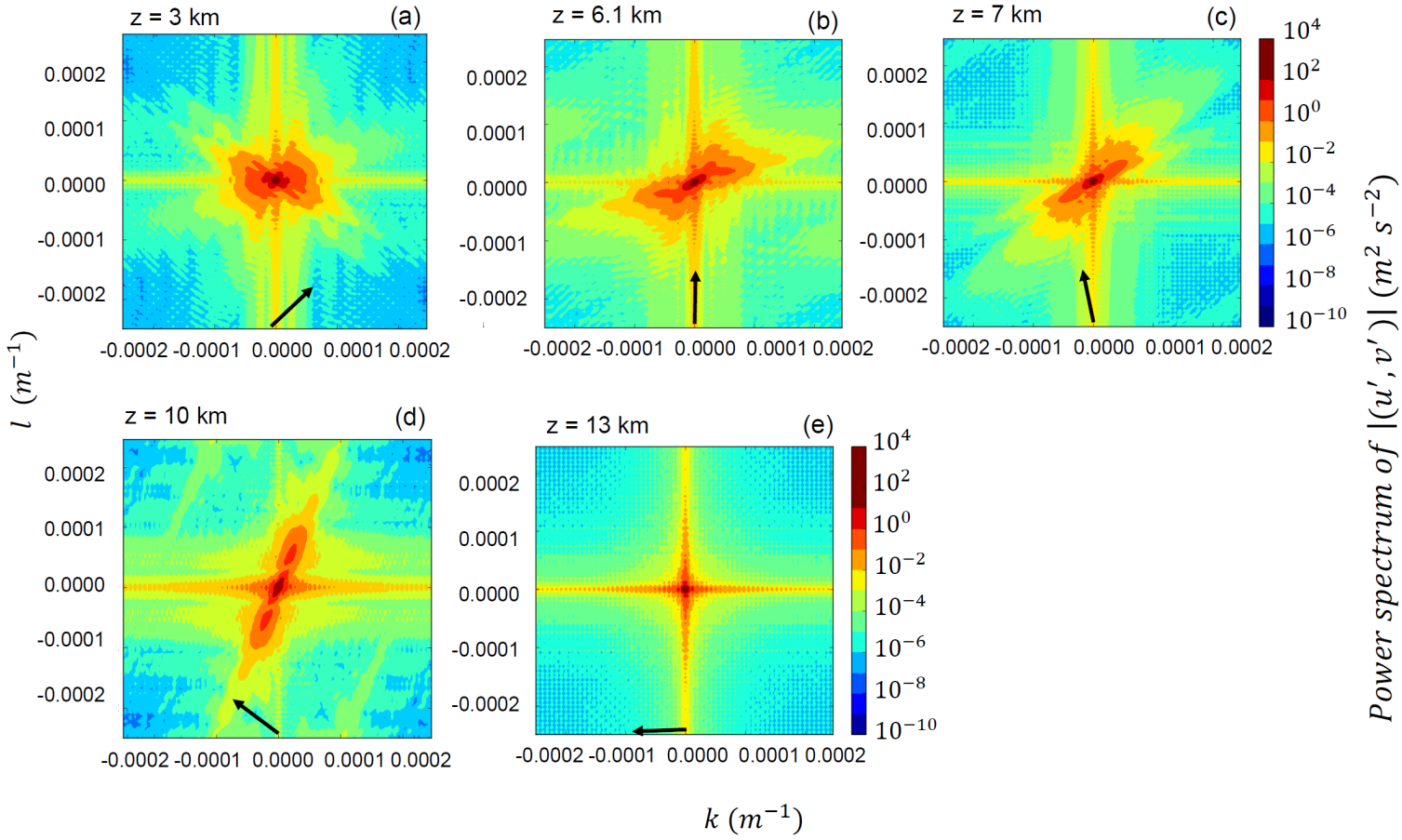

FIGURE 5.8: 2D power spectra of the horizontal velocity perturbation field for an idealized numerical simulation of directional shear flow over an isolated axisymmetric mountain, computed at heights of 3 km (a), 6.1 km (b), 7 km (c), 10 km (d), 13 km (e). The axes show the wave-number components along x and y. The black arrows indicate the wind direction at each height.

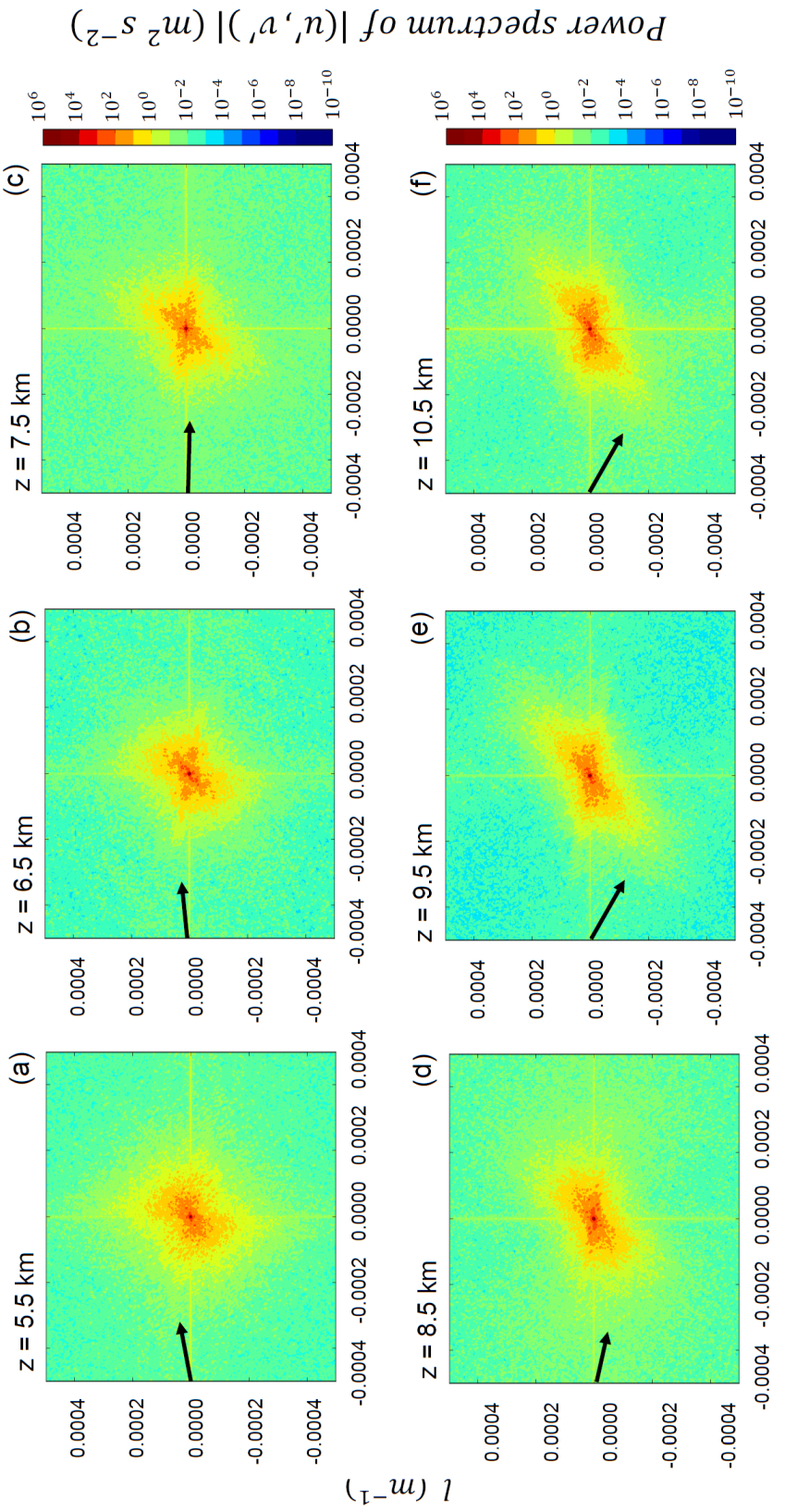

FIGURE 5.9: Continues on next page.

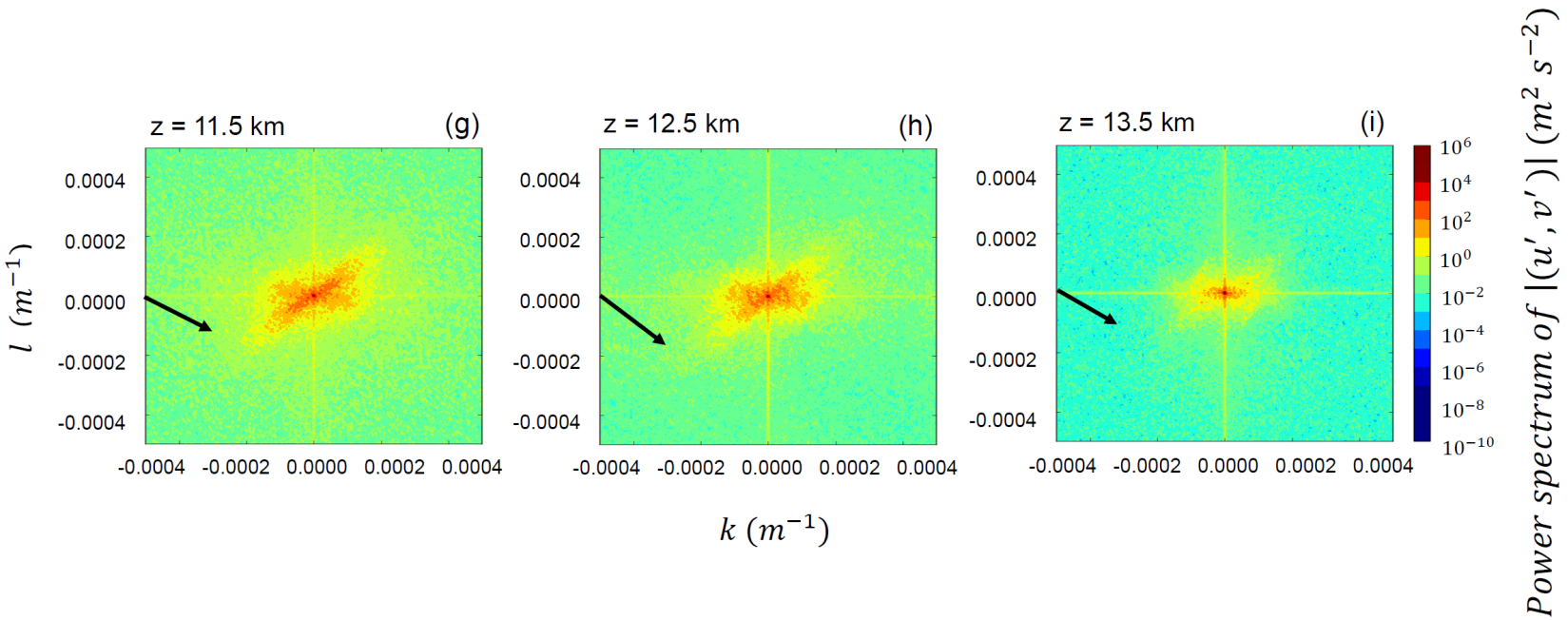

FIGURE 5.9: 2D power spectra of the horizontal velocity perturbation field for the semi-idealized numerical simulation presented in section 5.4.1, computed at heights corresponding to each kilometre of the atmosphere between 5.5 and 15.5 km. Axes and black arrows as in Figure 5.8.

The slower and non-constant rate of wind turning with height characterizing this case makes it more difficult to detect the rotation of the dominant wave-number following the wind. However, a rotation is still revealed by the changing orientation with height of the dominant wave energy lobes in the plots. In particular, approximate perpendicularity between the wind direction and the dominant wave-numbers can be seen between 7.5 and 10.5 km. These are the heights where, in physical space, most of the wave breaking occurs. Between 9.5 km and 10.5 km, the wind direction remains constant. At higher altitudes, 11.5 – 13.5 km, the wind rotation rate slows down and, as a consequence, the differences between spectra become harder to distinguish. By 13.5 km, because of the wave breaking taking place below and the ensuing critical level absorption, most of the wave energy has been dissipated. Note that, just as in the idealized case of Figure 5.8, when estimated more precisely the angle between the incoming wind vector and the dominant wave-number vector is seen to be slightly lower than 90 degrees (e.g. Figure 5.9(g)).

The wave behaviour inferred from the spectra in Figure 5.9, being essentially similar to that displayed in Figure 5.8, is equally explained via the mechanism leading to wave breaking in directional shear flows. In contrast, similar 2D power spectra computed for Test 4 (not shown), where the wind direction is constant with height, display no selective wave-energy absorption as a function of height.

5.5 Summary and conclusions

In this chapter, mountain wave turbulence in the presence of directional vertical wind shear over the Rocky Mountains in the state of Colorado has been investigated. For the winter seasons of 2015 and 2016, days with a significant directional wind shear within the upper troposphere (4 km – tropopause height) were identified by analysing atmospheric soundings measured upstream of the Rocky Mountains at the Grand Junction meteorological station (GJT). Among these days, pilot reports of turbulence encounters (PIREPs) were used to select cases where moderate or severe turbulence events were reported.

A selected case was investigated by performing semi-idealized numerical simulations, and sensitivity tests, aimed at discerning the contribution of mountain wave breaking due to directional shear in the observed turbulence event. In these simulations, the WRF-ARW model was initialized with a 1D atmospheric sounding from Grand Junction (CO) and a real (but truncated) orography profile. The orography was modified

in the sensitivity test "Test 1", and the atmospheric sounding was modified in the sensitivity tests "Test 2", "Test 3", "Test 4".

For the simulation with a real atmospheric sounding and orography, low positive and negative Richardson number values (used to identify regions of flow instability) occurred between 6.5 km and 10 km, providing overall good agreement with the PIREPs.

In Test 1, the role of the surface forcing in causing wave breaking was investigated. In particular, the lower boundary condition was modified and replaced with a 3D bell-shaped mountain and an idealized mountain ridge containing a few peaks. For these experiments, overall the agreement between model-predicted instabilities and PIREPs degraded. However, a better representation of flow dynamical and convective instabilities was achieved when an orography with a few peaks was considered. The results of Test 1 support the hypothesis that, in directional shear flows, by exciting substantially different wave spectra, orographies with different shapes, heights and orientations can change the nature of the wave-critical level interaction.

In Test 2, the effect of the tropopause and of the vertical variation of N on wave breaking were tested. The real atmospheric stability profile was replaced with an idealized profile prescribed by imposing a constant $N = 0.01$ m s^{-1}. Despite the constant stability, the investigated wave breaking event still occurred, and the flow cross-sections showed essentially the same features observed in the real-sounding simulation.

In Test 3, the influence of the variation of wind speed with height on wave steepening was explored. In a first test, the speed shear contribution was eliminated by modifying the atmospheric sounding so that changes in u' and v' were due to directional shear only, while the wind speed was kept constant at 10 m s^{-1}. In a second test, the directional shear contribution was eliminated by keeping the wind direction constant with height while the observed wind speed variation was retained. In the directional-shear-only simulation, the investigated turbulence encounter was still present. In the speed-shear-only simulation, no overturning regions were found in the simulation domain at $z \approx 7$ km, where the studied turbulence encounter occurred. These tests suggest that wave breaking was not likely attributable to the presence of speed shear.

In Test 4, the highly non-linear boundary condition imposed by the Rocky Mountains (for which $NH/U = O(1)$) was studied. Both wind speed and direction were kept constant with height, but two different wind speeds were used, namely: U = 10 m s^{-1} and U = 20 m s^{-1}. For the 10 m s^{-1} simulation, $NH/U = 2$, so mountain waves are relatively weak and propagate upwards without breaking where turbulence was observed. For the 20 m s^{-1} simulation, $NH/U = 1$ and mountain waves break at

multiple altitudes. These tests show that for the orography and flow configuration under investigation, wave breaking is quite sensitive to the wind speed of the incoming flow. The large variation of U in the lowest kilometres of the atmosphere does not allow us to exclude self-induced overturning as a possible wave breaking mechanism. Instead, this mechanism probably coexists with the directional shear, which acts to localize vertically the wave breaking event.

In connection with the studied wave breaking event, a significant downwind transport of unstable air was detected in horizontal cross-sections of the flow. This allows mountain-wave-induced turbulence to be found at large horizontal distances from the orography that generates the waves. A possible explanation for the observed flow pattern is the existence of an "asymptotic wake", as predicted by Shutts (1998) using linear theory for waves approaching critical levels in directional shear flows. The asymptotic wake translates into lobes of maximum wave energy extending roughly along the wind direction at a particular height, but not perfectly aligned with the wind. This peculiar flow structure was displayed by the horizontal velocity perturbation field (u', v') in horizontal cross-sections of the simulated flow.

Critical levels associated with directional shear were further investigated using spectral analysis of the magnitude of the (u', v') vector. This was done for a fully idealized flow and for the more realistic flow that is the main focus of the present study. Power spectra of the horizontal velocity perturbation at different heights and changes in the corresponding wave energy distribution by wavenumber (i.e. wave energy absorption/enhancement) were analysed.

For the fully idealized simulation, the continuous distribution of critical levels in the vertical makes the dominant wave-number vector at each height be (almost) perpendicular to the background wind vector at that height. As a result, the wave-number vector of the most energetic wave-mode rotates counter-clockwise, following the background wind 90 degrees out of phase. The implications of this for the approximate perpendicularity between the background wind vector and the wave velocity perturbation vector at critical levels is discussed in section 3.3.3 of this thesis.

For the semi-idealized simulation, it was still possible to detect a rotation of the dominant wave-number with the wind, even if less clearly than in the idealized case. In particular, the wind direction and the dominant wave-number were seen to be approximately perpendicular between 7.5 and 10.5 km where most of the wave breaking occurs in physical space.

The experiments discussed in this chapter suggest that critical levels induced by directional shear played a crucial role in originating the investigated turbulence encounter (ModTurb1 in Table 5.1). The directional shear contribution to wave breaking dynamics is particularly relevant to the problem of how the wave energy is selectively absorbed or dissipated at critical levels, which also has implications for drag parametrization (Teixeira and Yu, 2014). Furthermore, directional shear produces regions of flow instability far downwind from the obstacle generating the waves. This is a non-trivial result, especially for hydrostatic mountain waves, which are expected to propagate essentially vertically, and are therefore treated in drag parametrizations using a single-column approach. This downstream propagation of instabilities, which is a manifestation of the "asymptotic wake" predicted by Shutts (1998), hence represents an overlooked turbulence generation mechanism that, if adequately taken in account, might improve the location accuracy of mountain wave turbulence forecasts.

The semi-idealized approach used here was particularly well-suited to the aims of the present study, as it allowed us to isolate and investigate separately different wave breaking mechanisms. However, the simplifications adopted in the numerical simulations constitute a source of uncertainty regarding the applicability of the results to real situations. Making the numerical simulations more realistic by including missing physical processes (e.g., boundary layer effects, moisture and phase transitions), would therefore be a natural next step to further understand the observed turbulence event.

5.6 Appendix 5.A: Wave energy distribution at critical levels

In this appendix, the mechanism by which the wave amplitude is enhanced in the vicinity of critical levels will be further discussed. In particular, the energy difference between power spectra at different heights will be investigated. This analysis strengthens the conclusions drawn above regarding the role of directional critical levels in the Rocky Mountains turbulence case, and provides a more detailed description of the energy distribution observed in the wave spectra for the idealized case also discussed.

Figure 5.10(a) shows the difference in spectral energy computed by subtracting the power spectrum at $z = 3$ km (Figure 5.8(c)) from the power spectrum at $z = 7$ km (Figure 5.8(a)), for the idealized simulation with a constant rate of wind turning with height with $\mathrm{Ri}_{in} = 16$ and $N_0 H/U = 1$, presented in Chapter 3.

The portion of the spectrum where the energy difference is negative shows where in spectral space the energy of mountain waves has decreased with height. This is consistent with the absorption of wave energy at critical levels, as discussed in section 5.4.3.1. As expected, wave-numbers in the second quadrant ($k < 0$, $l > 0$) (and in the fourth quadrant, by symmetry) are absorbed between 3 km and 7 km, following the counter-clockwise rotation of the background wind vector. In Figure 5.11(a) the same field as presented in Figure 5.10(a) is shown but the directions of the background wind vector at 3 km (dashed arrow) and 7 km (solid arrow) are displayed. The straight-lines also shown in these figures, departing from the origin of the k, l plane, are perpendicular to each of these wind vectors, and correspond to the directions of the wave-number vectors that have their critical levels at those altitudes. The angular interval between the two straight-lines (roughly) corresponds to the portion of the wave spectrum where energy absorption has occurred (negative values in blue shading). This graphical representation highlights (even if only qualitatively) the dependence of the energy absorption on the directional shear of the background flow. While the energy absorption can also be discerned by a simple visual comparison of Figure 5.8(a) and 5.8(c), the key aspect to note in Figure 5.10(a) is the enhancement of wave energy for those wave-numbers that are approaching their critical levels (but have not reached them yet). Indeed, this feature is not easily quantified by looking at the power spectra in Figure 5.8.

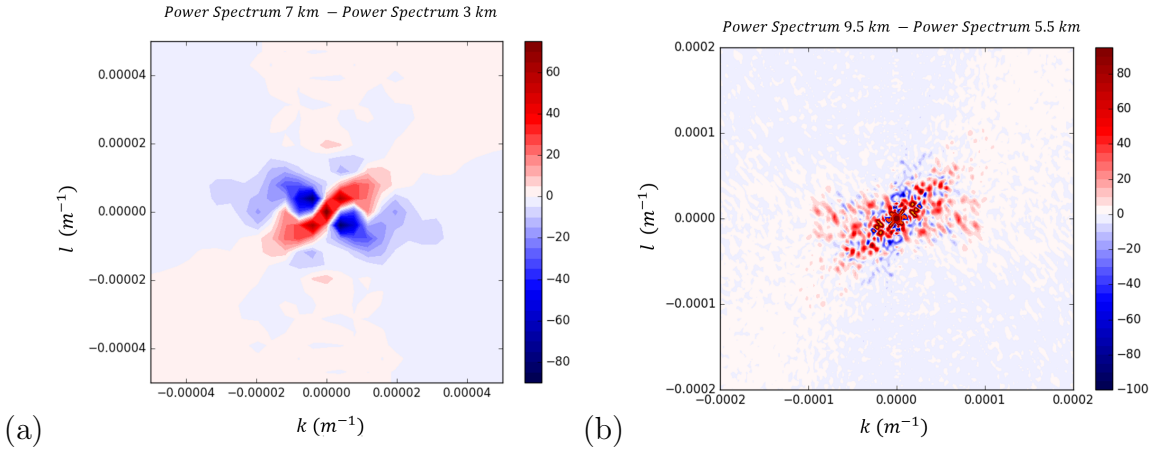

FIGURE 5.10: Differences in spectral energy calculated between: (a) the power spectra at 7 km and 3 km (in Figure 5.8) for the idealized simulation with a constant rate of wind turning with height, (b) the power spectra at 9.5 km and 5.5 km (in Figure 5.9) for the semi-idealized simulation of a turbulence encounter over the Rocky Mountains.

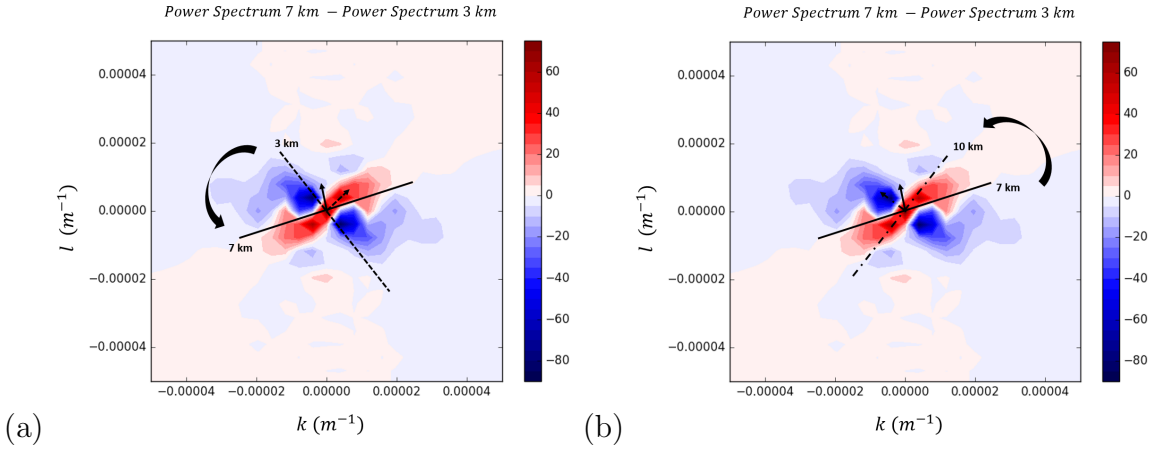

FIGURE 5.11: Differences in spectral energy as in Figure 5.10(a) but where the direction of the background wind vector is shown at: (a) 3 km (dashed arrow) and 7 km (solid arrow), (b) 7 km (solid arrow) and 10 km (dash-dot arrow). The straight-lines departing from the origin of the k, l plane are perpendicular to each of these wind vectors, and correspond to the directions of the wave-number vectors that have their critical levels at those altitudes.

In the spectrum of Figure 5.10(a) the wave energy difference is positive for the majority of the wave-numbers in the first quadrant ($k > 0$, $l > 0$), implying that the wave amplitude is larger at 7 km than 3 km. Figure 5.11(b) is similar to Figure 5.11(a) but the direction of the wind vector at 10 km (dash-dot arrow) is shown.

The wave-number vector perpendicular to the wind at 7 km (represented by the solid straight-line) is the one primarily responsible for wave breaking in the region where Ri_{out} <0 in Figure 5.7(b). However, other fairly energetic wave-numbers are also present (i.e. like the negative values, the positive values form a wide angular band). A possible interpretation for this energy distribution is that, although from linear theory waves are expected to achieve their maximum amplitude at critical levels (where they will suddenly break and dissipate), the wave amplitude actually starts to increase some distance below a critical level. Therefore, at a given height, the high energy region in the spectrum may be the result of an increased amplitude not only for the wave-number having its critical level, but also for other wave-numbers that are approaching their critical levels located at higher altitudes. Thus, the angular interval between the wave-numbers perpendicular to the wind at 7 km (solid line) and at 10 km (dash-dot line) can be thought of as the portion of the spectrum for which the wave amplitude enhancing mechanism acting in the vicinity of the critical level has already started to operate, but where the corresponding wave-numbers have not yet been absorbed.

Note that the energy contained in these wave-numbers seems also to be the reason why, in Figure 3.7 of Chapter 3, the effective angle between the (u', v') vector and the background wind vector in physical space is not exactly 90 degrees but larger (around 120 degrees). Indeed, if one uses inverse Fourier transformation to synthesize a (u', v') vector in physical space using the energy contained in the third[2] quadrant of the spectrum shown in Figure 5.10(a), this vector will point to the left of the background wind by an angle larger than 90 degrees.

Finally, energy differences in spectral space have been computed for the semi-idealized simulation of the Rocky Mountains turbulence case. In Figure 5.10(b) the energy change between the power spectra at $z = 9.5$ km (Figure 5.9(c)) and $z = 5.5$ km (Figure 5.9(a)) km is shown. The height interval between these two power spectra corresponds to the depth over which directional shear is significant and where, in physical space, most of the wave breaking occurs. A narrow region of wave energy absorption is visible in the first quadrant of the spectrum, close to the k axis. The existence of this region is consistent, by the same mechanism as explained above and graphically shown in Figure 5.11, with the wind rotation from (approximately) westerly to north-westerly, as shown in Figure 5.9(a) and (c).

[2]The third quadrant should be used because in Figure 3.7(a) the (u', v') vectors in the breaking region point towards the south-west.

Positive energy differences, and the consequent increase in wave amplitude, can again be explained by the presence of directional critical levels. However, in this case, the rotation of the wind above 9.5 km slows down significantly, so it seems unlikely that directional critical levels are the only reason for the (wide) high energy region in the first quadrant of Figure 5.10(b). This is probably a consequence of changes in the background flow parameters, such as the stability and wind speed, between the two heights where the power spectra were taken or even above. Indeed, as shown in Figure 5.2(b), the wind speed between 5.5 km and 9.5 km decreases from 20.6 m s^{-1} to 18 m s^{-1}. As mentioned previously (see section 5.4.2.3), this type of variation can cause the wave amplitude to increase. Additionally, the significant increase in N^2 starting at about 11 km can cause wave reflections (see section 5.4.2.2), which might also result in an enhancement of the wave amplitude at lower atmospheric levels by resonance. Although sensitivity tests 2 and 3 indicate that these mechanisms are not strong enough to cause wave breaking, they may still be strong enough for their contribution to the wave dynamics to be revealed in the power spectrum of Figure 5.10(b).

Chapter 6

Conclusions

6.1 Summary

Several mechanisms cooperate to make orographic gravity waves break down into turbulence. In this thesis, instability of those waves initiated by a variation of the wind direction with height (directional shear) was investigated. The aim was to achieve a better physical understanding of mountain wave breaking in directional shear flows, with potential applications to aviation Clear-Air Turbulence (CAT) forecast.

Idealized and semi-idealized numerical simulations using the WRF atmospheric model were performed. In the idealized numerical experiments, mountain shapes with a simple mathematical definition and prototypes of flows with directional wind shear were used to study the occurrence of wave breaking over a 3D orography. In the semi-idealized simulations, a real CAT encounter over the Rocky Mountains was investigated by simulating more realistic atmospheric conditions and using a real (albeit truncated) orography as lower boundary condition.

The interpretation of model outputs was developed by comparison with linear theory predictions, through spectral analysis of the wind velocity perturbation field and by carrying out various sensitivity tests.

The modelling approach employed in this thesis used a set of numerical simulations of increasing realism (although always partly idealized) that allowed us to look at the problem of breaking mountain waves in gradually more complex scenarios. An advantage of such a methodology is that, thanks to the knowledge gained in simpler case scenarios, attributions of cause and effect are possible even when the degree of

realism of the flow, and with it the number of variables and physical processes at play, has increased.

6.2 Main results and conclusions

The work presented in this thesis was motivated by research questions presented in Chapter 1. The main findings for each research question are described next:

(a) Under a controlled scenario, how does wave breaking depend on background flow parameters?

- In chapter 3, idealized simulation results for hydrostatic mountain waves were used to produce a regime diagram (Figure 3.3) diagnosing wave breaking occurrence as a function of the terrain elevation (quantified through N_0H/U) and the strength of directional shear (quantified through Ri_{in}). When directional shear is not considered, wave breaking is observed only for $N_0H/U > 1$ ($H > 1$ km), as found by previous authors. In the presence of a background directional shear, due to the non-linear response of waves to the background flow and the effect of critical levels, wave breaking can occur over lower mountains than in a constant-wind case. Wave breaking always occurs when $N_0H/U = 1$ ($H = 1$ km), no matter what intensity of the directional shear is used (note that for the weakest directional shear flow considered here $\mathrm{Ri}_{in} = 16$, which roughly corresponds to a rate of wind turning with height of $\beta \approx 14$ degrees/km). When $N_0H/U = 0.75$ ($H = 750$ m) wave breaking is detected for moderately strong and strong directional shear flows with $\mathrm{Ri}_{in} \leqslant 4$ ($\beta \approx 31$ degrees/km or faster). For $N_0H/U = 0.5$ ($H = 500$ m) wave breaking is found for flows with $\mathrm{Ri}_{in} \leqslant 2$ ($\beta \approx 40$ degrees/km or faster). It is only when assuming very small mountain heights ($N_0H/U = 0.1$ and 0.2) that wave breaking is completely absent for any directional shear intensity considered. Therefore, for gradually stronger directional shears, the critical N_0H/U for wave breaking decreases down to at least 0.5.

(b) Where is turbulence generation expected with respect to the orography that generates the mountain waves?

- Time-series of the Richardson number of the total flow (Ri_{out}) showed that Ri_{out} remains roughly between 0 and 0.25 both before and after wave-breaking periods. Thus, by considering grid-points where $\mathrm{Ri}_{out} < 0.25$, regions within the

simulation domain where wave breaking and the development of Clear-Air Turbulence are more likely were identified (Figure 3.6). The extent and location of these regions vary with the background wind shear intensity. In particular, increasing the strength of the directional shear leads to wider regions of (potential) turbulence generation and a more complex flow topology, for which Ri_{out} values lower than 0.25 occur simultaneously in many vertical levels. Additionally, for stronger shear flows, the greater density of critical levels cause the wave energy to be dissipated in the lower levels in the atmosphere (i.e. all the wave breaking occurs in the first few kilometres above the ground). The turbulent nature of the instability regions identified in the inviscid simulations from the value of the Richardson number (Ri) was confirmed by performing additional numerical simulations where turbulence was parametrized and represented through its associated TKE (Figure 3.11).

(c) Is there a way to diagnose this type of turbulence?

- Mountain wave breaking strongly depends on environmental conditions set at large-scale (such as wind speed and direction, atmospheric stability and orography profile). The aforementioned regime diagram (see answer to question (a)) provides a way of predicting wave breaking based on large-scale variables, without the need to explicitly resolve mountain waves. With such a method it is possible to identify for which combination of mountain height and background wind shear wave breaking is expected in simplified flow conditions.

  Additionally, by examining the dynamics of the horizontal velocity perturbations associated with the waves in Fourier space, it was found that the Fourier transform of the horizontal velocity perturbation vector and the wave-number vector are approximately aligned at critical levels (Figure 3.8 and Equations (3.11)-(3.12)). When transposed to physical space, this condition provides a possible diagnostic for CAT forecast in directional shear flows, based on the approximate perpendicularity between the horizontal velocity perturbation associated with the wave and the mean incoming wind.

(d) How does the stability of the flow to wave breaking change in the transition from hydrostatic non non-hydrostatic mountain waves?

- In chapter 4, mountain waves excited by narrow 3D orography were investigated. For this type of waves, the dependence of the vertical wave-number on the horizontal wave-number introduces dispersion effects in the gravity wave dynamics that are expected to influence the occurrence of wave breaking. A regime diagram for non-hydrostatic mountain waves (Figure 4.2) was produced

and compared with the analogous regime diagram for hydrostatic mountain waves. It was found that while for weaker shear flows non-hydrostatic effects increase the stability of the flow due to wave dispersion, for stronger shear flows non-hydrostatic effects decrease the stability of the flow, owing to the increased magnitude of the vertical velocity perturbation over narrow orography. The balance between these two mechanisms determines the likeliness of wave breaking. Therefore, although non-hydrostatic mountain waves are generally believed to be less likely to break because of their dispersive nature, in the presence of directional wind shear this seems to be only partially true. Ultimately this is because directional wind shear controls the distance over which dispersion effects can act before the waves break.

(e) In a real turbulence event, what is the role of directional shear in triggering wave breaking? Can we isolate its contribution?

- In chapter 5, for a selected case study over the Rocky Mountains, the connections between directional shear and an observed aviation turbulence event were studied through semi-idealized numerical simulations.

  The capability of the model to reproduce the observed turbulence encounter was assessed by comparing model outputs (i.e. generation of flow instability in fields such as potential temperature, horizontal wave velocity perturbations and Richardson number) and observations (PIREPs). An overall good agreement between the PIREPs database and model-predicted instabilities was found when the model was initialized with a real orography profile (albeit truncated). However, the agreement between observations and model worsened significantly when an idealized lower boundary condition was used (Test 1). This is because the mechanism leading to wave breaking in directional shear flows is sensitive to the bottom boundary condition. In particular, because of their different spectral energy distribution, the wave spectra excited by the idealized mountain and by the realistic orography result in a different wave-directional critical level interaction.

  The role of directional shear in causing wave breaking was isolated by performing sensitivity tests to exclude the variation of the atmospheric stability with height (Test 2), the speed shear (Test 3), and the mountain amplitude (Test 4) as dominant wave breaking mechanisms. The signature of directional shear-induced wave breaking was found in a significant downwind transport of instabilities observed in flow cross-sections (Figure 5.4(a)). In particular, mountain wave turbulence was detected at large horizontal distances from the orography that generated the waves. The existence of an asymptotic wake, as

predicted by Shutts (1998) using linear theory for waves approaching critical levels in directional shear flows, was hypothesized to be responsible for this downwind transport (Figure 5.7).

Other flow features suggesting the role of directional shear in causing wave breaking are: the filtering of wave energy by directional critical levels that vanished in Test 4 where directional wind shear was removed (Figure 5.5(c)); the spectral wave energy distribution at critical levels, in connection with the findings mentioned in the answer to question (c) above (see also below).

(f) In Fourier space (i.e., by spatial scale), how is the spectral wave energy distributed at directional critical levels?

- Critical levels induced by directional shear were studied by taking 2D power spectra of the magnitude of the horizontal velocity perturbation field. This was done for a fully idealized flow (Figure 5.8), presented in chapter 3, and for the more realistic flow (Figure 5.9) discussed in chapter 5. In the spectra of both flows (although more clearly for the idealized case) a rotation of the most energetic wave modes with the background wind, as well as an approximate perpendicularity between the background wind vector and the wave-number vector of those modes at critical levels, could be found. Such behaviour is consistent with the mechanism expected to lead to wave breaking in directional shear flows, associated with interaction between waves and their critical levels. Additionally, when energy differences in spectral space were computed for the horizontal velocity perturbation between two different heights, regions in the spectra where wave energy is absorbed (negative differences) and enhanced (positive differences) (Figure 5.11) were found. Negative and positive energy difference regions correspond to wave-numbers that were already absorbed by their critical levels or that are approaching their critical levels but have not reached them yet, respectively.

6.3 Directions for future work

The idealized nature of the flows considered in this thesis, and the simplifications adopted in the numerical simulations, limit the applicability of the results to real situations. In particular, the prototypes of directional shear flows used in the idealized simulations assume unrealistic constant rates of wind turning with height and static stability. Additionally, missing physical processes like the development of a boundary layer above the ground, the Earth's rotation, moisture and phase transitions etc.,

could modify the flow behaviour. Thus, the work presented here could be extended by adding complexity to the simplified scenarios considered so far. Some of the aspects of the physics of mountain waves that still need to be clarified have been already touched upon throughout the thesis. Other aspects, to be mentioned next, need to be considered *ab initio*.

As mentioned in chapter 3, one may wonder how the introduction of a Planetary Boundary Layer would modify the regime diagram presented in Figure 3.3. As suggested by previous studies (Ólafsson and Bougeault, 1997, Peng and Thompson, 2003), waves generated in the presence of a PBL are expected to be weaker than the ones developing in a frictionless flow, because the PBL attenuates the amplitude of the flow perturbations forced by the lower boundary condition. Thus, in directional shear flows, for a same mountain height, we may need a stronger directional shear in order to achieve wave breaking by comparison with inviscid simulations. However, the weakening of waves in the presence of a PBL is not large enough to totally counter-balance the increase of the wave amplitude in the vicinity of directional critical levels. Additionally, definitive conclusions cannot be drawn without taking into account the stratification of the boundary layer. Jiang and Doyle (2008) showed that the diurnal variation of the PBL (driven by surface heating or cooling) results in a diurnal variation of the interaction between the PBL flow and mountain waves. While a well-developed convective PBL seems to reduce the gravity waves amplitude, a nocturnal stable PBL acts to increase the wave amplitude when $N_0 H/U_0 \approx 1$. It remains to be known how these phenomena would interact with a directional wind shear.

The idealized numerical simulations of chapter 3 and 4 could also benefit from a more realistic upper boundary condition. As mentioned in chapter 5, the interaction between vertically-propagating mountain waves and the tropopause may trigger wave breaking. This is mainly a consequence of two distinct mechanisms: on the one hand, the increase in static stability at the tropopause makes the waves behave, to a certain extent, as in the presence of a critical level. The increased N results in a larger vertical wave-number m in the stratosphere that will facilitate wave breaking (VanZandt and Fritts, 1989). On the other hand, the discontinuity represented by the jump in static stability may generate wave reflections into the troposphere. As shown by Leutbecher (2001), upward and downward propagating waves can interfere, constructively or destructively, with consequences to the wave amplitude itself. These two mechanisms coexist and probably modify the wave amplitude in the lower stratosphere and upper troposphere (Smith *et al.*, 2008). One of the ways in which directional shear could interact with these mechanisms, is by selective filtering of the wave energy with

height. If waves generated at the surface are dissipated because of directional critical levels, they may never reach the tropopause, or reach it with a substantially smaller amplitude, resulting in a different wave response from the one expected if no critical levels existed.

Regarding the possible wave breaking diagnostic proposed in chapter 3, initial attempts to use the perpendicularity condition between the horizontal velocity perturbation and the background wind vectors were made in Appendix 3.B. These preliminary tests showed some difficulties in using the diagnostic, and the need to combine the perpendicularity criterion with at least another constraint. For this purpose, the magnitude of the velocity perturbation vector was used, as we can expect it to be large at critical levels and wave breaking regions. Although the validity of this diagnostic was discussed in the thesis from a theoretical prospective, its applicability needs to be tested. This type of work would probably require a considerable amount of time and a large number of test cases to guide empirical choices (such as the selection of threshold values etc.) using also knowledge of the physics of mountain waves at critical levels. Ultimately, if the diagnostic proved to be successful, it could become part of the group of diagnostics currently employed for CAT forecasting (as mentioned before, presently, none of the diagnostics in use considers the contribution of directional shear to wave breaking).

Regarding the semi-idealized simulations presented in chapter 5, results could be made more robust by repeating the study running the WRF model in its "real configuration". This would entail initializing the model with 3D weather fields of wind, pressure, temperature etc., and turning on the parameterizations of physical processes (radiation, PBL, surface heat and moisture fluxes etc.), and including the Coriolis force. In this type of simulation, uncertainties due to the simplifications adopted in the semi-idealized approach would be reduced, but a physical understanding of processes would become more difficult. For example, we could assess how the effects of a transient background flow would impact our results (in the semi-idealized simulations included in the thesis the background flow was prescribed as a fixed field that does not change in time). The effects of moisture and phase transitions on the atmospheric stability could also be taken into account. Furthermore, using an orography that is not laterally truncated might alter the wave-directional critical level interaction via modification of the surface forcing (see answer to question (e) above). It would be interesting to compute power spectra of the horizontal velocity perturbations in these more realistic conditions and check whether they can still represent a useful tool or, instead, the information would be too distorted by other physical processes now modelled. Finally, more case studies like the one investigated here could be considered to

confirm (or contradict) the conclusions and hypotheses formulated in chapter 5.

The research presented in this thesis had a clear focus on flow instability due to mountain wave breaking, with implications for aviation turbulence. However, it is worth mentioning that Clear-Air Turbulence is only one of the many manifestations of mountain waves. Recalling Figure 1.1 (b), where the diversity of topics related to mountain waves is reviewed, it must be noted that the interaction of mountain waves with directional critical levels also affects the global atmospheric circulation. An improved understanding of where wave breaking is expected, and under what flow conditions, could assist in the development of new orographic drag parameterizations, where directional shear probably needs to be taken into account. In an even more general context, the study of dynamical aspects of gravity waves such as non-hydrostatic effects, their spectral energy distribution and their interaction with critical levels contributes towards the fundamental research needed to improve our understanding of the interaction between the mean flow and 3D orographic gravity waves.

Bibliography

Ágústsson, H. and Ólafsson, H. (2014). Simulations of observed lee waves and rotor turbulence. *Mon. Wea. Rev.*, **142**, 832–849.

Alexander, S., Klekociuk, A., Pitts, M., McDonald, A., and Arevalo-Torres, A. (2011). The effect of orographic gravity waves on antarctic polar stratospheric cloud occurrence and composition. *Journal of Geophysical Research: Atmospheres*, **116**, 1–15.

Alexander, S., Klekociuk, A., McDonald, A., and Pitts, M. (2013). Quantifying the role of orographic gravity waves on polar stratospheric cloud occurrence in the antarctic and the arctic. *Journal of Geophysical Research: Atmospheres*, **118**, 493–507.

Ambaum, M. H. P. and Marshall, D. P. (2005). The effects of stratification on flow separation. *J. Atmos. Sci.*, **62**, 2618–2625.

Bacmeister, J. T. and Schoeberl, M. R. (1989). Breakdown of vertically propagating two-dimensional gravity waves forced by orography. *Journal of the Atmospheric Sciences*, **46**, 2109–2134.

Baines, P. G. (1998). *Topographic effects in stratified flows*. Cambridge University Press.

Barstad, I., Grabowski, W. W., and Smolarkiewicz, P. K. (2007). Characteristics of large-scale orographic precipitation: Evaluation of linear model in idealized problems. *Journal of Hydrology*, **340**, 78–90.

Bauer, M. H., Mayr, G. J., Vergeiner, I., and Pichler, H. (2000). Strongly nonlinear flow over and around a three-dimensional mountain as a function of the horizontal aspect ratio. *J. Atmos. Sci.*, **57**, 3971–3991.

Bender, C. M. and Orszag, S. A. (2013). *Advanced mathematical methods for scientists and engineers I: Asymptotic methods and perturbation theory*. Springer Science & Business Media.

Bertaux, J.-L., Khatuntsev, I., Hauchecorne, A., Markiewicz, W. J., Marcq, E., Lebonnois, S., Patsaeva, M., Turin, A., and Fedorova, A. (2016). Influence of venus topography on the zonal wind and uv albedo at cloud top level: The role of stationary gravity waves. *Journal of Geophysical Research: Planets*, **121**, 1087–1101.

Boer, G. and Lazare, M. (1988). Some results concerning the effect of horizontal resolution and gravity–wave drag on simulated climate. *Journal of climate*, **1**, 789–806.

Booker, J. R. and Bretherton, F. P. (1967). The critical layer for internal gravity waves in a shear flow. *J. Fluid Mech.*, **27**, 513–539.

Broad, A. S. (1995). Linear theory of momentum fluxes in 3-d flows with turning of the mean wind with height. *Q. J. R. Meteorol. Soc.*, **121**, 1891–1902.

Broutman, D., Eckermann, S. D., Knight, H., and Ma, J. (2017). A stationary phase solution for mountain waves with application to mesospheric mountain waves generated by auckland island. *J. Geophys. Res. - Atmos.*, **122**, 699–711.

Businger, J. A. (1969). Note on the critical richardson number(s). *Q. J. R. Meteorol. Soc.*, **95**, 653–654.

Carslaw, K. S., Wirth, M., Tsias, A., Luo, B., Dörnbrack, A., Leutbecher, M., Volkert, H., Renger, W., Bacmeister, J. T., Reimer, E., *et al.* (1998). Increased stratospheric ozone depletion due to mountain-induced atmospheric waves. *Nature*, **391**, 675–678.

Carslaw, K. S., Peter, T., Bacmeister, J. T., and Eckermann, S. D. (1999). Widespread solid particle formation by mountain waves in the arctic stratosphere. *Journal of Geophysical Research: Atmospheres*, **104**, 1827–1836.

Clark, T. and Peltier, W. (1977). On the evolution and stability of finite-amplitude mountain waves. *Journal of the Atmospheric Sciences*, **34**, 1715–1730.

Clark, T. L. and Peltier, W. R. (1984). Critical level reflection and the resonant growth of nonlinear mountain waves. *J. Atmos. Sci.*, **41**, 3122–3134.

DeWekker, S. and Kossmann, M. (2015). Convective boundary layer heights over mountainous terrain - a review of concepts. *Front. Earth Sci.*, **3**, 77.

Dörnbrack, A., Gerz, T., and Schumann, U. (1995). Turbulent breaking of overturning gravity waves below a critical level. *Appl. Scient. Res.*, **54**, 163–176.

Doyle, J. and Jiang, Q. (2006). Observations and numerical simulations of mountain waves in the presence of directional wind shear. *Q. J. R. Meteorol. Soc.*, **132**, 1877–1905.

Doyle, J., Durran, D., Chen, C., Colle, B., Georgelin, M., Grubisic, V., Hsu, W., Huang, C., Landau, D., Lin, Y. L., *et al.* (2000). An intercomparison of model-predicted wave breaking for the 11 january 1972 boulder windstorm. *Mon. Wea. Rev.*, **128**, 901–914.

Doyle, J. D. (2004). Evaluation of topographic flow simulations from coamps and wrf. In *20th Conference on Weather Analysis and Forecasting/16th Conference on Numerical Weather Prediction*.

Doyle, J. D. and Reynolds, C. A. (2008). Implications of regime transitions for mountain-wave-breaking predictability. *Monthly Weather Review*, **136**, 5211–5223.

Doyle, J. D., Shapiro, M. A., Jiang, Q., and Bartels, D. L. (2005). Large-amplitude mountain wave breaking over greenland. *Journal of the atmospheric sciences*, **62**, 3106–3126.

Durran, D. R. (1986). Another look at downslope windstorms. part i: The development of analogs to supercritical flow in an infinitely deep, continuously stratified fluid. *Journal of the Atmospheric Sciences*, **43**, 2527–2543.

Durran, D. R. (1990). Mountain waves and downslope winds. In *Atmospheric processes over complex terrain*, pages 59–81.

Eckermann, S. D., Dörnbrack, A., Flentje, H., Vosper, S. B., Mahoney, M., Bui, T. P., and Carslaw, K. S. (2006). Mountain wave–induced polar stratospheric cloud forecasts for aircraft science flights during solve/theseo 2000. *Wea. Forecast.*, **21**, 42–68.

Eliassen, A. and Palm, E. (1960). On the transfer of energy in stationary mountain waves. *Geofys. Publ.*, **22**, 1–23.

Ferrari, R. and Wunsch, C. (2009). Ocean circulation kinetic energy: Reservoirs, sources, and sinks. *Annual Review of Fluid Mechanics*, **41**, 253–282.

Fukuhara, T., Futaguchi, M., Hashimoto, G. L., Horinouchi, T., Imamura, T., Iwagaimi, N., Kouyama, T., Murakami, S.-y., Nakamura, M., Ogohara, K., *et al.* (2017). Large stationary gravity wave in the atmosphere of venus. *Nature Geoscience*, **10**, 85–88.

Garcia, R. R. and Solomon, S. (1985). The effect of breaking gravity waves on the dynamics and chemical composition of the mesosphere and lower thermosphere. *Journal of Geophysical Research: Atmospheres*, **90**, 3850–3868.

Gill, P. G. (2014). Objective verification of world area forecast centre clear air turbulence forecasts. *Meteorol. Applic.*, **21**, 3–11.

Gill, P. G. and Stirling, A. J. (2013). Including convection in global turbulence forecasts. *Meteorol. Applic.*, **20**, 107–114.

Goldstein, S. (1931). On the stability of superposed streams of fluids of different densities. *Proceedings of the Royal Society of London. Series A, Containing Papers of a Mathematical and Physical Character*, **132**, 524–548.

Grisogono, B. (1994). Dissipation of wave drag in the atmospheric boundary layer. *Journal of the atmospheric sciences*, **51**, 1237–1243.

Grisogono, B. and Enger, L. (2004). Boundary-layer variations due to orographic-wave breaking in the presence of rotation. *Quarterly Journal of the Royal Meteorological Society*, **130**, 2991–3014.

Grubišić, V. and Smolarkiewicz, P. K. (1997). The effect of critical levels on 3d orographic flows: Linear regime. *J. Atmos. Sci.*, **54**, 1943–1960.

Grubišić, V., Serafin, S., Strauss, L., Haimov, S. J., French, J. R., and Oolman, L. D. (2015). Wave-induced boundary layer separation in the lee of the medicine bow mountains. part ii: Numerical modeling. *J. Atmos. Sci.*, **72**, 4865–4884.

Guarino, M. V., Teixeira, M. A. C., and Ambaum, M. H. P. (2016). Turbulence generation by mountain wave breaking in flows with directional wind shear. *Q. J. R. Meteorol. Soc.*, **142**, 2715–2726.

Hahn, D. C. (2007). Evaluation of wrf performance for depicting orographically-induced gravity waves in the stratosphere. Technical report, DTIC Document.

Hanazaki, H. and Hunt, J. (2004). Structure of unsteady stably stratified turbulence with mean shear. *Journal of Fluid Mechanics*, **507**, 1–42.

Hines, C. O. (1971). Generalizations of the richardson criterion for the onset of atmospheric turbulence. *Q. J. R. Meteorol. Soc.*, **97**, 429–439.

Holton, J. R. and Hakim, G. J. (2012). *An Introduction to Dynamic Meteorology*. Academic press.

Huppert, H. E. and Miles, J. W. (1969). Lee waves in a stratified flow. part 3. semi-elliptical obstacle. *J. Fluid Mech*, **35**, 481–496.

Jiang, Q. and Doyle, J. D. (2004). Gravity wave breaking over the central alps: Role of complex terrain. *J. Atmos. Sci.*, **61**, 2249–2266.

Jiang, Q. and Doyle, J. D. (2008). On the diurnal variation of mountain waves. *J. Atmos. Sci.*, **65**, 1360–1377.

Julian, L. T. and Julian, P. R. (1969). Boulder's winds. *Weatherwise*, **22**, 108–126.

Keller, T. L., Trier, S. B., Hall, W. D., Sharman, R. D., Xu, M., and Liu, Y. (2015). Lee waves associated with a commercial jetliner accident at denver international airport. *J. Appl. Meteor. Climatol.*, **54**, 1373–1392.

Kim, J.-H. and Chun, H.-Y. (2010). A numerical study of clear-air turbulence (cat) encounters over south korea on 2 april 2007. *J. Appl. Meteor. Climatol.*, **49**, 2381–2403.

Kirshbaum, D. J., Bryan, G. H., Rotunno, R., and Durran, D. R. (2007). The triggering of orographic rainbands by small-scale topography. *Journal of the atmospheric sciences*, **64**, 1530–1549.

Klemp, J. and Lilly, D. (1978). Numerical simulation of hydrostatic mountain waves. *Journal of the Atmospheric Sciences*, **35**, 78–107.

Klemp, J. B. and Wilhelmson, R. B. (1978). The simulation of three-dimensional convective storm dynamics. *Journal of the Atmospheric Sciences*, **35**, 1070–1096.

Knight, H., Broutman, D., and Eckermann, S. D. (2015). Integral expressions for mountain wave steepness. *Wave Motion*, **56**, 1–13.

Lane, T. P., Doyle, J. D., Sharman, R. D., Shapiro, M. A., and Watson, C. D. (2009). Statistics and dynamics of aircraft encounters of turbulence over greenland. *Mon. Wea. Rev.*, **137**, 2687–2702.

Laprise, R. (1992). The euler equations of motion with hydrostatic pressure as an independent variable. *Monthly weather review*, **120**, 197–207.

Laprise, R. and Peltier, W. R. (1989). On the structural characteristics of steady finite-amplitude mountain waves over bell-shaped topography. *Journal of the atmospheric sciences*, **46**, 586–595.

Leutbecher, M. (2001). Surface pressure drag for hydrostatic two-layer flow over axisymmetric mountains. *J. Atmos. Sci.*, **58**, 797–807.

Lilly, D. K. (1978). A severe downslope windstorm and aircraft turbulence event induced by a mountain wave. *J. Atmos. Sci.*, **35**, 59–77.

Lilly, D. K. and Kennedy, P. J. (1973). Observations of a stationary mountain wave and its associated momentum flux and energy dissipation. *J. Atmos. Sci.*, **30**, 1135–1152.

Lin, Y.-L. (2007). *Mesoscale Dynamics*. Cambridge University Press.

Lindzen, R. S. (1981). Turbulence and stress owing to gravity wave and tidal breakdown. *Journal of Geophysical Research: Oceans*, **86**, 9707–9714.

Lindzen, R. S. and Tung, K. K. (1976). Banded convective activity and ducted gravity waves. *Mon. Wea. Rev.*, **104**, 1602–1617.

Long, R. R. (1953). Some aspects of the flow of stratified fluids: I. a theoretical investigation. *Tellus*, **5**, 42–58.

Lott, F. and Miller, M. J. (1997). A new subgrid-scale orographic drag parametrization: Its formulation and testing. *Q. J. R. Meteorol. Soc.*, **127**, 101–127.

Mahalov, A., Moustaoui, M., and Nicolaenko, B. (2009). Three-dimensional instabilities in non-parallel shear stratified flows. *Kinetic and Related Models*, **2**, 215–229.

Markowski, P. and Richardson, Y. (2006). On the classification of vertical wind shear as directional shear versus speed shear. *Weather and forecasting*, **21**, 242–247.

McFarlane, N. A. (1987). The effect of orographically excited gravity wave drag on the general circulation of the lower stratosphere and troposphere. *J. Atmos. Sci.*, **44**, 1775–1800.

McHugh, J. and Sharman, R. (2013). Generation of mountain wave-induced mean flows and turbulence near the tropopause. *Q. J. R. Meteorol. Soc.*, **139**, 1632–1642.

Mesinger, F., Arakawa, A., and Sundqvist, H. (1976). *Numerical methods used in atmospheric models*. World Meteorological Organization, International Council of Scientific Unions.

Miles, J. W. (1961). On the stability of heterogeneous shear flows. *J. Fluid Mech.*, **10**, 496–508.

Miles, J. W. and Huppert, H. E. (1969). Lee waves in a stratified flow. part 4. perturbation approximations. *J. Fluid Mech.*, **35**, 497–525.

Miranda, P. M. A. and James, I. N. (1992). Non-linear three-dimensional effects on gravity-wave drag: Splitting flow and breaking waves. *Q. J. R. Meteorol. Soc.*, **118**, 1057–1081.

Miyoshi, Y. and Fujiwara, H. (2008). Gravity waves in the thermosphere simulated by a general circulation model. *Journal of Geophysical Research: Atmospheres*, **113**, 1–11.

Nappo, C. J. (2012). *An Introduction to Atmospheric Gravity Waves, 2nd Ed.* Academic Press.

Ólafsson, H. and Bougeault, P. (1997). The effect of rotation and surface friction on orographic drag. *J. Atmos. Sci.*, **54**, 193–210.

Peng, M. S. and Thompson, W. T. (2003). Some aspects of the effect of surface friction on flows over mountains. *Q. J. R. Meteorol. Soc.*, **129**, 2527–2557.

Queney, P. (1947). *Theory of perturbations in stratified currents with applications to air flow over mountain barriers*. University of Chicago Press.

Sachsperger, J., Serafin, S., and Grubišić, V. (2016). Dynamics of rotor formation in uniformly stratified two-dimensional flow over a mountain. *Quarterly Journal of the Royal Meteorological Society*, **142**, 1201–1212.

Schwartz, B. (1996). The quantitative use of pireps in developing aviation weather guidance products. *Wea. Forecast.*, **11**, 372–384.

Scorer, R. (1949). Theory of waves in the lee of mountains. *Quarterly Journal of the Royal Meteorological Society*, **75**, 41–56.

Sharman, R. and Lane, T. (2016). *Aviation Turbulence: Processes, Detection, Prediction*.

Sharman, R. and Pearson, J. (2016). Prediction of energy dissipation rates for aviation turbulence: Part i. forecasting non-convective turbulence. *J. Appl. Meteor. Climatol.*, **56**, 317–337.

Sharman, R., Tebaldi, C., Wiener, G., and Wolff, J. (2006). An integrated approach to mid-and upper-level turbulence forecasting. *Wea. Forecast.*, **21**, 268–287.

Sharman, R., Trier, S., Lane, T., and Doyle, J. (2012a). Sources and dynamics of turbulence in the upper troposphere and lower stratosphere: A review. *Geophys. Res. Lett.*, **39**, L12803.

Sharman, R., Cornman, L., Meymaris, G., Pearson, J., and Farrar, T. (2014). Description and derived climatologies of automated in situ eddy-dissipation-rate reports of atmospheric turbulence. *J. Appl. Meteor. Climatol.*, **53**, 1416–1432.

Sharman, R. D., Doyle, J. D., and Shapiro, M. A. (2012b). An investigation of a commercial aircraft encounter with severe clear-air turbulence over western greenland. *J. Appl. Meteor. Climatol.*, **51**, 42–53.

Shutts, G. (1995). Gravity-wave drag parametrization over complex terrain: The effect of critical-level absorption in directional wind-shear. *Q. J. R. Meteorol. Soc.*, **121**, 1005–1021.

Shutts, G., Kitchen, M., and Hoare, P. (1988). A large amplitude gravity wave in the lower stratosphere detected by radiosonde. *Quarterly Journal of the Royal Meteorological Society*, **114**, 579–594.

Shutts, G. J. (1998). Stationary gravity-wave structure in flows with directional wind shear. *Q. J. R. Meteorol. Soc.*, **124**, 1421–1442.

Shutts, G. J. and Gadian, A. (1999). Numerical simulations of orographic gravity waves in flows which back with height. *Q. J. R. Meteorol. Soc.*, **125**, 2743–2765.

Sigmond, M., Scinocca, J. F., and Kushner, P. J. (2008). Impact of the stratosphere on tropospheric climate change. *Geophysical Research Letters*, **35**, L12706.

Skamarock, W. C. and Klemp, J. B. (2008). A time-split nonhydrostatic atmospheric model for weather research and forecasting applications. *J. Comput. Phys.*, **227**, 3465–3485.

Skamarock, W. C., Klemp, J. B., Dudhia, J., Gill, D. O., Barker, D. M., Wang, W., and Powers, J. G. (2005). A description of the advanced research wrf version 2. Technical report, DTIC Document.

Smith, R. B. (1977). The steepening of hydrostatic mountain waves. *J. Atmos. Sci.*, **34**, 1634–1654.

Smith, R. B. (1980). Linear theory of stratified hydrostatic flow past an isolated mountain. *Tellus*, **32**, 348–364.

Smith, R. B. (1989). Mountain-induced stagnation points in hydrostatic flow. *Tellus*, **41A**, 270–274.

Smith, R. B., Woods, B. K., Jensen, J., Cooper, W. A., Doyle, J. D., Jiang, Q., and Grubišić, V. (2008). Mountain waves entering the stratosphere. *Journal of the Atmospheric Sciences*, **65**, 2543–2562.

Smith, S., Baumgardner, J., and Mendillo, M. (2009). Evidence of mesospheric gravity-waves generated by orographic forcing in the troposphere. *Geophysical Research Letters*, **36**.

Smolarkiewicz, P. K. and Rotunno, R. (1989). Low froude number flow past three dimensional obstacles. part 1: Baroclinically generated lee vortices. *J. Atmos. Sci*, **46**, 1154–1164.

Staquet, C. and Sommeria, J. (2002). Internal gravity waves: from instabilities to turbulence. *Annual Review of Fluid Mechanics*, **34**, 559–593.

Stiperski, I. and Grubišić, V. (2011). Trapped lee wave interference in the presence of surface friction. *Journal of the Atmospheric Sciences*, **68**, 918–936.

Strauss, L., Serafin, S., Haimov, S., and Grubišić, V. (2015). Turbulence in breaking mountain waves and atmospheric rotors estimated from airborne in situ and doppler radar measurements. *Q. J. R. Meteorol. Soc.*, **141**, 3207–3225.

Sun, J., Nappo, C. J., Mahrt, L., Belušić, D., Grisogono, B., Stauffer, D. R., Pulido, M., Staquet, C., Jiang, Q., Pouquet, A., *et al.* (2015). Review of wave-turbulence interactions in the stable atmospheric boundary layer. *Reviews of geophysics*, **53**, 956–993.

Taylor, G. (1931). Effect of variation in density on the stability of superposed streams of fluid. *Proceedings of the Royal Society of London. Series A, Containing Papers of a Mathematical and Physical Character*, **132**, 499–523.

Teixeira, M. A. C. (2014). The physics of orographic gravity wave drag. *Front. Phys.*, **2**, 43.

Teixeira, M. A. C. and Miranda, P. M. A. (2009). On the momentum fluxes associated with mountain waves in directionally sheared flows. *J. Atmos. Sci.*, **66**, 3419–3433.

Teixeira, M. A. C. and Yu, C.-L. (2014). The gravity wave momentum flux in hydrostatic flow with directional shear over elliptical mountains. *Eur. J. Mech. B - Fluids*, **47**, 16–31.

Teixeira, M. A. C., Miranda, P. M. A., and Valente, M. A. (2004). An analytical model of mountain wave drag for wind profiles withshear and curvature. *J. Atmos. Sci.*, **61**, 1040–1054.

Teixeira, M. A. C., Miranda, P. M. A., and Argaín, J. L. (2008). Mountain waves in two-layer sheared flows: Critical-level effects, wave reflection, and drag enhancement. *J. Atmos. Sci.*, **65**, 1912–1926.

Teixeira, M. A. C., Argaín, J. L., and Miranda, P. M. A. (2013). Orographic drag associated with lee waves trapped at an inversion. *Journal of the Atmospheric Sciences*, **70**, 2930–2947.

Teixeira, M. A. C., Paci, A., and Belleudy, A. (2017). Drag produced by waves trapped at a density interface in non-hydrostatic flow over an axisymmetric hill. *J. Atmos. Sci.*, **74**, 1839–1857.

The Globe and Mail (2015). Experts weigh in on possible causes of turbulence on air canada flight. https://www.theglobeandmail.com/news/alberta/experts-weigh-in-on-possible-causes-of-turbulence-on-air-canada-flight/article27980763/.

The Weather Channel (2017). Turbulence forces american airlines emergency landing; 5 injured. https://weather.com/news/news/turbulence-american-airlines-flight-diverted.

Trier, S. B., Sharman, R. D., and Lane, T. P. (2012). Influences of moist convection on a cold-season outbreak of clear-air turbulence (cat). *Mon. Wea. Rev.*, **140**, 2477–2496.

Turner, J. (1999). Development of a mountain wave turbulence prediction scheme for civil aviation. Technical report, Met Office, Bracknell, UK.

Turner, J. S. (1973). *Buoyancy Effects in Fluids*. Cambridge University Press.

VanZandt, T. E. and Fritts, D. C. (1989). A theory of enhanced saturation of the gravity wave spectrum due to increases in atmospheric stability. *pure and applied geophysics*, **130**, 399–420.

Vosper, S. (2004). Inversion effects on mountain lee waves. *Quarterly Journal of the Royal Meteorological Society*, **130**, 1723–1748.

Whiteway, J. A., Pavelin, E. G., Busen, R., Hacker, J., and Vosper, S. (2003). Airborne measurements of gravity wave breaking at the tropopause. *Geophys. Res. Lett.*, **30**, 2070.

Wolff, J. and Sharman, R. (2008). Climatology of upper-level turbulence over the contiguous united states. *J. Appl. Meteor. Climatol.*, **47**, 2198–2214.

Worthington, R. (1998). Tropopausal turbulence caused by the breaking of mountain waves. *J. Atmos. Solar-terrest. Phys.*, **60**, 1543–1547.

Xu, X., Wang, Y., and Xue, M. (2012). Momentum flux and flux divergence of gravity waves in directional shear flows over three-dimensional mountains. *J. Atmos. Sci.*, **69**, 3733–3744.

Xu, X., Xue, M., and Wang, Y. (2013). Gravity wave momentum flux in directional shear flows over three-dimensional mountains: Linear and nonlinear numerical solutions as compared to linear analytical solutions. *J. Geophys. Res-Atmos.*, **118**, 7670–7681.

Zängl, G. (2003). Orographic gravity waves close to the nonhydrostatic limit of vertical propagation. *Journal of the atmospheric sciences*, **60**, 2045–2063.